

# Bioinspired Peano-HASEL Actuation

2nd Year Report

Harrison McAleese

Supervisor:

Dr Andrew Weightman

Co-supervisors:

Dr Alejandro Macario Rojas & Dr Vidyadhar Peesapati

# Contents

<b>1</b>	<b>Introduction</b>	<b>1</b>
<b>2</b>	<b>Literature Review</b>	<b>3</b>
2.1	Saltatorial Locomotion . . . . .	3
2.1.1	In Nature . . . . .	3
2.1.2	Saltatorial Robots . . . . .	9
2.1.3	Summary . . . . .	10
2.2	Series Elastic Actuator . . . . .	11
2.2.1	Robotic Series Elastic Acatuators . . . . .	11
2.2.2	Variable Stiffness Acatuators . . . . .	12
2.2.3	Summary . . . . .	13
2.3	Soft Robotics . . . . .	13
2.3.1	Dielectric Elastomer Actuators . . . . .	13
2.3.2	Hydraulically Amplified Self-Healing Electrostatic Actuators . . . . .	14
2.3.3	Peano-HASEL Actuators . . . . .	16
2.3.4	Summary . . . . .	21
2.4	Conclusions . . . . .	21
<b>3</b>	<b>Research Outline</b>	<b>28</b>
3.1	Aim and Objectives . . . . .	28
<b>4</b>	<b>Development and Evlauation of Peano-HASEL SEAs</b>	<b>30</b>
4.1	Design . . . . .	30
4.1.1	Outline . . . . .	32
4.2	Peano-HASEL Manufacturing . . . . .	32
4.2.1	Film and Heatsealing . . . . .	32
4.2.2	Applying Electrodes . . . . .	35
4.2.3	Oil and Filling . . . . .	37
4.3	Numerical Series Elastic Element Investigations . . . . .	38
4.3.1	Peano-HASEL Scaling and Expansions . . . . .	38
4.3.2	Hookean Spring Studies . . . . .	40
4.3.3	Discussion . . . . .	48
4.3.4	Conclusions . . . . .	49
4.4	Manufacturing, Development and Evaluation of Silicone Series Elastic Elements . . .	51
4.4.1	Silicone Molding . . . . .	51
4.5	SEE-PH Coupling . . . . .	51
4.5.1	PLA Embedded "Root" Couplings . . . . .	51

4.5.2	Methodology . . . . .	52
4.5.3	Current Results . . . . .	53
4.5.4	Discussion . . . . .	55
4.5.5	Conclusions . . . . .	58
4.6	Initial Investigations of Variable Stiffness . . . . .	58
4.6.1	Methodology . . . . .	58
4.6.2	Results and Discussion . . . . .	59
4.6.3	Conclusions . . . . .	62
<b>5</b>	<b>Series Elastic Element Optimisation with Genetic Algorithm</b>	<b>63</b>
5.1	Objective Function and Bounds . . . . .	64
5.2	Geometry Definition . . . . .	65
5.2.1	Two Dimensional Geometry . . . . .	66
5.2.2	Three Dimensional Geometry . . . . .	66
5.3	Modelling and Simulation . . . . .	66
5.4	Optimisation . . . . .	68
5.5	Results . . . . .	69
5.6	Discussion . . . . .	71
5.7	Conclusions . . . . .	72
<b>6</b>	<b>Discussions, Conclusions and Future Work</b>	<b>73</b>
6.1	Discussion . . . . .	73
6.2	Conclusions . . . . .	73
6.3	Overview of Future Work . . . . .	74
6.4	PH-VSA Work Packages . . . . .	77
6.5	Stretch: Long-Short Term Memory Control and Sensing . . . . .	79
6.5.1	Proposed Approach . . . . .	79
<b>A</b>	<b>Experimental Setup</b>	<b>81</b>
<b>B</b>	<b>Matlab code</b>	<b>88</b>

# List of Figures

2.1	Examples of Power Modulation across phylums from literature. Top Left: Galago <sup>[2]</sup> . Top Right: Bullfrog <sup>[88]</sup> . Bottom Left: Leopard Frog <sup>[6]</sup> . Bottom Right: Guinea Fowl <sup>[35]</sup> . . . . .	6
2.2	Variable stiffness of the aperneurosis and a cartoon demonstrating the loading mechanism <sup>[8;89]</sup> . . . . .	8
2.3	Examples of SEAs from literature. Notice the size and holistic complexity of these actuators. Top: MKIV Geared LSEA <sup>[51]</sup> . Middle Left: Variable Stiffness Compliant Actuator <sup>[85]</sup> . Middle Right: Hip SEA for THOR robot <sup>[53]</sup> . Bottom Left: MIT Ballscrew based SEA <sup>[91]</sup> . Bottom Right: Compact Rotary SEA for human assistance <sup>[54]</sup> . . . . .	22
2.4	Basic operation of a High-Strain Peano-HASEL actuator. The operation of electrode zipping is the same as in all PH actuators, only the placement of the electrode is changed in HS-PH. <sup>[109;95]</sup> . . . . .	23
2.5	Load-Strain characteristics of two types of Peano-HASEL actuator compared. Until 4% strain, standard PH actuators could lift higher loads than their Hig-Strain counterparts <sup>[109]</sup> . . . . .	23
2.6	Effect of increasing voltage on operational mechanisms of Peano-HASEL actuators from Kellaris et.al(2018) <sup>[50]</sup> . . . . .	24
2.7	Geometry definition for the deformation of the Peano-HASEL actuator from Kellaris et.al(2019) <sup>[49]</sup> . . . . .	24
2.8	Scaling behaviours of the Peano-HASEL actuators, taken from Kellaris et.al (2019) <sup>[49]</sup> . . . . .	25
2.9	Equivalent Circuit of a DEA. As the electric field in non-zipped regions of Peano-HASELs can be neglected, the zipped region behaves like a DEA. . . . .	25
2.10	Self-sensing of a PH-Fibre with miniturised circuitry by Ly et.al (2020) <sup>[64]</sup> . . . . .	26
2.11	Demonstration of PH signature values. . . . .	27
4.1	A complete Peano-HASEL Fibre with signature [1   7   80   20   0.6] . . . . .	33
4.3	Example Scaling behaviours of PH-Actuators . . . . .	39
4.4	Behaviour of a linear SEE with increasing stiffness. The optimal value of stored energy arises at 23.42% actuator efficiency and a stiffness of $k = 119 \times 10^3 \text{Nm}^{-1}$ . Acuated by a PH-Sarcomere (BOPP - $V = 10\text{kV}$ - [1   1   120   20   0.6]) . . . . .	41
4.5	Demonstration of a $10000\text{Nm}^{-1}$ SEE blocking a single PH-Sarcomere (BOPP - $V = 10\text{kV}$ - [1   1   120   20   0.6]). Note the considerable area below the actuator curve not enclosed by the SEE curve, demonstrating the inefficiency of the linear SEE. . . . .	42
4.6	The parametrisation of geometry for the four types of geometry in this study, defined by the four ratio parameters: Type 1 - $\lambda$ ; Type 2 - $\sigma$ ; Type 3 - $\zeta$ ; Type 4 - $\rho$ . . . . .	43

4.7	Geometric Parameter sweeps for (a) $\lambda$ , (b) $\sigma$ , (c) $\rho$ (for $n = 5$ ) and (d) $\zeta$ . Both (c) and (d) are swept in values defined by the area maintaining conversion factors in table 5.1. . . . .	46
4.8	Normalised with respect to the control geometry: variations in $k$ for respective area maintaining $\lambda$ equivalents (defined by table 5.1). . . . .	47
4.9	Sample averaged mechanical testing results for geometries. The first legend numbers display the equivalent $\lambda$ value and the later indicates geometry type ( $\equiv \lambda$ Type). Detail A shows the transition region between stress-strain regimes. Experimental noise and error is more prominent and visible in this region on this scale. . . . .	48
4.10	The interaction of Peano-HASEL Force-Stroke behaviour with the mechanical testing data suggests poor energy storage efficiency and minimal useful stiffness tuning potential. . . . .	49
4.11	BOPP SEE energy storage metrics compared to the available Peano-HASEL energy output. The $\zeta$ and $\rho$ parameters show strong grouping while $\lambda$ tapering reduces effectiveness. While gains can be made through $\zeta$ variation, the strong grouping indicates a plateau in these gains. Notably, facilitating further development of Peano-HASEL output energy before blocking did not increase the energetic effectiveness of an SEE. . . . .	50
4.12	Example root with variables:... Note the exposed sides towards the bottom of the root. . . . .	52
4.13	Demonstrations of root interactions with SEE during loading and after failure. . . . .	54
4.14	Failure testing of root based SEEs. . . . .	55
4.15	Ramping Cyclic Loading tests. The SEE is loaded between an incrementally increasing force range. 4.15a shows the evolution of the dependant displacement with time. 4.15b shows the controlled variable force with time. 4.15c shows the behaviour of the SEE during loading and unloading. As time progresses, the response is shifted to the right by the hysteresis curves. Significant hysteresis is observed in zone 1 & 2, but on subsequent loading the magnitude of the hysteresis is smaller suggesting a settling of the root into a new stable seating within the SEE. 4.15d shows detail of the last loading before failure where significant hysteresis occurs at $65N \leftrightarrow 70N$ . . . . .	56
4.16	Displacement oscillations in Peano-HASEL range. . . . .	57
4.17	Demonstrative picture of variable stiffness samples. . . . .	59
4.18	Results for the successful variable stiffness sample . . . . .	60
4.19	Comparison of successful vs failed variable stiffness tests. 4.19a: Working variable stiffness SEE with the aponeurosis displaced. Results for this test are given in Figure 4.18. 4.19b: Example Pull-off failure of silicone tabs at 12mm lateral displacement. Note that any of the tabs could fail and which failed was highly variable. 4.19c: Hole failure around the screws. Only one of these failures was observed across 4 samples. . . . .	61
5.1	Genetic Algorithm operational cartoon demonstrating standard workflow and generalised genetic operations, from Brunton et.al (2015) <sup>[18]</sup> . . . . .	64
5.2	High level workflow of Genetic Algorithm optimisation. The loop is iterated until defined exit conditions are observed. . . . .	65
5.3	2D geometry generator diagram. . . . .	67
5.4	Geometry example for 3D case. Detail A shows a top down view of the vector fan. Not drawn with realistic proportions. . . . .	67

5.5	Characteristic cartoon demonstrating genetic operations Crossover, Mutation and Scramble. . . . .	69
5.6	Comparison of experimental data, linear regression model and results of the genetic algorithms modelling and simulation. The difference between the linear fit and the genetic algorithm is imperceptable at this scale. . . . .	70
5.7	Evolution of a single SEE throughout generation . . . . .	71
6.1	Gantt chart demonstrating future project workflow. . . . .	76
A.1	Control Code on PC . . . . .	82
A.2	MyRio Labview Code . . . . .	83
A.3	Diagram of High voltage setup. . . . .	84
A.4	Experimental setup for displacement readings in high voltage cage. The brakcet can be mouted at vvarying height using the holes in cage, allowing for any PH-SEA design. . . . .	85
A.5	Experimental circuit. The circuit can be left loose as the cage is interlocked and fully grounded, making exposed components safe. Data Acquisition is carried out by a MyRio controller and the PSU converts mains to 12v. The cb-101 is a DC-DC transformer that bumps a 12v signal into a 10kv. The CB101 is controllable with a 5v signal from the myrio and provides feeback through current and voltage monitors. . . . .	86
A.6	Grpahical abstract of SHVRIMPS system that will be loaned to this project to help complete multi-channel actuation in the PH-VSA . . . . .	87

# List of Tables

4.1	PH-VSA design specification for jumping robot applications. Many of these are also general specifications. . . . .	30
4.2	Selected FR3 oil properties . . . . .	37
4.3	Matrix of geometric parameters that maintain the ratio between the area of the control geometry, $A_{Con}$ , and the tapered Type 1 area , $A_\lambda$ , in a BOPP SEE. As SEE thickness is constant, this ratio is equivalent to the ratio of material volume and, assuming a homogeneous material, this allows distinction between the mechanism of stiffness variation: whether it is related to topography or material volume. The topographic mechanism would see equal stiffness variation for all geometries which share a row. The columns for $\lambda$ and $\sigma$ are equivalent, and the two types share a stiffness variation curve (Figure.4.8). The first row defines the control geometry and the corresponding geometric parameters that create it. . . . .	44
4.4	Area preserving conversions between $\lambda$ and other ratio parameters. $n$ quantifies the number of circles evenly distributed along a Type 4 length, set $n = 5$ . . . . .	45
5.1	Parameters for initial GA test . . . . .	72

## Abstract

In order to achieve robotic autonomy, compensation for novel environments is a critical component of a robotic locomotion design. This is particularly true for environments where terrain is harsh and three dimensional. Biological systems have great success in navigating complex terrain due to their physiology and control strategies. One biologically inspired set of movements is that of saltatorial locomotion. This set includes leaping motions like jumping, hopping and running. Jumping especially allows traversal of otherwise impassable terrain with high energy efficiency<sup>[41;89;66]</sup>. To achieve this, Nature employs compliant, linear actuators that work in tandem with components like tendons under adaptive and learned control.

Soft robotic actuators are a recent area of research attempting to mimic Nature's efficacy. Through embodied intelligence inherent to their material composition they have a intrinsic adaptability to novel impedance and high energy densities. The Peano-HASEL actuator is a linearly contracting electro-hydraulic actuator bearing resemblance to natural muscle, with attractive specific energy outputs, controlability and scalability<sup>[50;95]</sup>. This writing covers current research on series elastic actuation, soft robotics, specifically the Peano-HASEL actuator, and the principles that grant biological jumpers their efficacy and apply them to the expansion of the Peano-HASEL into a Variable Stiffness Actuator (VSA) with the test case of facilitating robotic saltatorial modes. The creation of a tendon-mimetic series elastic element is undertaken using evolution inspired optimisation techniques. The introduction of pennate Peano-HASELs will look to introduce variable stiffness by lateral deformation of the elastic element, controlled via an LSTM control scheme inspired by muscle to muscle reaction arcs in the periphial nervous system. This is the first macroscale fully soft SEA and the first to introduce variable stiffness. The design of the genetic algorithm for use in series elastic element design is novel. This work also looks to see the first application of an LSTM control scheme on a soft robot and the first implementation to VSAs as a stretch goal.

Manufacturing capability has been investigated and established for Peano-HASEL actuators along with experimental capacity for testing them. Silicone series elastic elements have also been manufactured and their couplings investigated for hysteresis and failure. The preliminary coupling designs can withstand forces up to 45N and suffer no hysteresis in the displacement range of the Peano-HASEL.

The applicability of aponeurosis inspired varibale stiffness was tested and showed that for small elements with a 12mm lateral displacement ( $\epsilon_{Lat} = 120\%$ ) showed a  $25 \rightarrow 5\%$  increase in tensile force during the loading.

The genetic algorithm was developed and tested, though results show minimal improvements in power modulation performance with current parameters. Further development is needed to allow multiple materials into the optimisation.

# Chapter 1

## Introduction

Robots are generally defined by autonomy. While simpler automata-like machines can carry out well defined, easily repeatable tasks, a robot is capable of complex action under its own autonomy. Modern robots are computer programmable, in general, able to carry out complex instructions and tasks. Crucially, however, they are distinguished from simpler machines by their ability to sense what is around them, adapting to stimuli to mould to a situation and in ideal theory adapt to some relative novelty<sup>[9]</sup>. Applications of these machines are numerous and exceptionally promising.

Examples of established and recent applications are robotic arms seeing use in manufacturing industries<sup>[3;40]</sup>; medical robotics<sup>[57;105;80;103]</sup>; farming<sup>[15;4;78;75;22]</sup>; and autonomous repair, maintenance and decommissioning in extreme environments<sup>[69;13;72;74;73;32]</sup>.

While these robots have proven themselves adequate for many tasks, the efficacy of natural systems has not yet been met. This is especially true of locomotive navigation where there are requirements of untethered operation. Limited power autonomy and efficiency many times smaller than natural systems limits applications, highlighting the need for energy efficient locomotion gaits and similarly efficient actuators<sup>[47]</sup>. Recent work has demonstrated that jumping is a highly efficient locomotion mode that can facilitate navigation of complex terrains with good energy economy<sup>[?]</sup>. Many biological systems utilise jumping<sup>[10;1;2;5;6;41]</sup>. Robotics using jumping have demonstrated impressive height performance, agility, the ability to navigate complex terrain and some exhibit multi-modal locomotion capability<sup>[33;99;116;76;114]</sup>. Jumping gaits are achieved in the majority through coupling of compliant elements in series and parallel to actuators<sup>[33;36;45;16]</sup>, in order to create protective impact absorption and allow for power modulation, a technique used in high impulse movements to supersede force-velocity outputs of actuators, inspired by natural systems<sup>[84;6;10;89]</sup>.

However, many of these robots have yet to see application in outdoor complex and novel environments. A robot in these environments that is untethered must have the ability to land and orientate for repeated jumps and it must do this on uneven and atypical terrain. So far, control has proved a challenging factor to achieve this<sup>[116]</sup>. This is without the addition of payloads which can add complexity to the dynamics. Many of the robots are miniature, making obstacles harder to surmount, increasing the need for good energy economy due to small batteries and larger required jumps. The size also reduces the available computation for complex control methods. High energetic density is of crucial importance to jumping robotics and materials used as well as the actuation strategies are factors that define this density.

The series elastic actuator (SEA) is an actuator paradigm that includes compliant components in series with, traditionally, motors. SEAs have proven effective in power modulation and energy

absorption/recovery tasks as mentioned and in general allow for expanded force bandwidths and increases in force control. SEAs however can suffer from high complexity, involving many interacting parts. This can reduce robustness, contribute to weight and incur energy losses from heating. In fixed stiffness actuators, there are also trade-offs between beneficial features requiring compliant or stiff impedance.

VSA s allow a SEA to shift its stiffness dynamically. This can allow an actuator to access the benefits of stiffer actuators such as force stability and positional accuracy while being able to absorb impacts, modulate power and exhibit highly efficient cyclic movements<sup>[113]</sup>. Methodologies to achieve VSAs are often complex, involving multiple actuators and springs. In hard, motor driven systems, multiple actuators often come with the needed transmission. Natural systems utilise variable stiffness in muscle tendon complexes to dynamically alter the mechanical response of their tendons<sup>[5;62]</sup>. This allows modulation of energy storage and may potentially allow for mitigation between trade-offs observed by fixed stiffness actuators. Evidence has been presented that suggests this is in part achieved by lateral deformation of the aponeurosis by the pennate muscle alignment seen in natural systems<sup>[5]</sup>. This mechanism has yet to see proper engineering application and has only been investigated briefly with rubber bands<sup>[43]</sup>.

Soft robotics is an emerging research field using compliant materials to mimic biological systems and imbue robots with embodied intelligence. These robotics are lightweight, adaptive to perturbations, able to deform easily while being mechanically resilient and are often low cost<sup>[24;81]</sup>. The Peano-HASEL actuator is a relatively new soft robotic actuator able to contract linearly with high energetic density; high frequency responses; precision control; relatively easy manufacturing with readily available materials and the ability to self-sense through capacitance monitoring<sup>[50;48;95;64]</sup>. These actuators couple electrostatic compression with hydraulics to create a local hydraulic pressure using dielectric oil to deform a flexible, inelastic polymer film. Peano-HASELs have seen applications in grippers, robotic finger and fish, for example. The Peano-HASEL provides a promising starting point from which to build a soft actuator suited to macro-scale jumping systems. To do this, an extension of the Peano-HASEL to a SEA is a novel and potentially beneficial research direction.

This work will take the Peano-HASEL actuator and expand it to accommodate series elasticity in order to develop a fully-soft actuator. While the main application target is jumping locomotion, the actuator will likely be generally applicable in principle. A genetic algorithm approach, utilising Finite Element Analysis (FEA) is utilised to optimise series elastic elements to best compliment the complex dynamics of the Peano-HASEL in power modulation tasks. The Peano-HASEL SEA (PH-SEA) is then further evolved into a VSA by the introduction of pennate Peano-HASELs, utilising the principle of lateral deformation to alter the stiffness. This methodology may potentiate multi-modal locomotion applications and provide the favourable benefits

# Chapter 2

## Literature Review

### 2.1 Saltatorial Locomotion

#### 2.1.1 In Nature

Saltatorial locomotion modes, such as jumping and hopping allow three-dimensional movement in difficult terrains. It is observed in vertebrates and invertebrates that find themselves in environments with a variety of obstacle types and at a multitude of size scales. The term *jumping* is distinguished from hopping by implying a standing start or a single movement, whereas hopping involves multiple, successive jumping movements in series. Hopping is prevalent mainly in mammalian species and is considered highly specialised. It is not uncommon for this locomotion mode to be applied in addition to cursorial (running) and arboreal (climbing/swimming) and the actuators employed must be able to facilitate all locomotive modes employed. Developing an actuator to facilitate saltatorial locomotion, such as in this work, demonstrates an actuator specialisation that implies actuator applicability to complimentary modes. The major advantages of jumping are numerous and include:

1. Ability to achieve sudden and often unpredictable impulses.
2. Obstacle Avoidance through utilisation of 3D environments.
3. Energy efficiency gains.

Sudden and often unpredictable impulses in saltatorial movements provide animals with a key tool to escape predators, attack prey or begin flight, providing crucial early acceleration<sup>[41;65]</sup>. Quadrupedal rodents are preyed upon at higher rates than the sympatric bipedal hopping counterparts and there are metabolic efficiencies in larger hopping species<sup>[66]</sup>. This is attributed to the unpredictability of jumping impulses allowing rapid trajectory changes, as well as the speed of the movement. The environmental evolutionary pressures that facilitate the origination of jumpers and hoppers are may be structurally complex: forested or rocky, for example, alluding to the benefits of this locomotion mode as a means to navigate unpredictable and unfavourable terrain effectively. Hopping also sees high use by Macropods in desert environments where resource scarcity promotes adaption to energy efficiency. The *Jaculus jaculus*, commonly called the lesser Egyptian Jerboa, uses hopping to great effect making hopping it's "fastest mode of steady-state locomotion"<sup>[66]</sup>.

## Take-off velocity

Jumping performance is partly a function of take-off velocity. James et al.<sup>[41]</sup> use a simple ballistic equation:

$$d = \frac{\sin(2\alpha)}{g} v^2 \quad (2.1)$$

Where:  $d[\text{m}]$  is distance jumped,  $v[\text{ms}^{-1}]$  is take-off velocity,  $\alpha[\text{deg}]$  is take-off angle and  $g[\text{ms}^{-2}]$  is the gravitational acceleration ( $\approx 9.81\text{ms}^{-2}$  on Earth). This equation is cited as demonstrating the dominance of the velocity term, which we can see is highly proportional to jump distance, by virtue of being a squared term. Assumptions made are the neglection of air resistance and that forces as well as acceleration are constant throughout the jump. It should also be noted that this equation does not take into consideration the location of the applied force in relation to the centre of mass, something that will be explored with detail in a section forthcoming. The review also acknowledges this, communicating that the kinematics become insensitive to take-off angle when this is considered, causing higher sensitivity to variations in take-off velocity and height. Equation (2.1) is expanded<sup>[65;41]</sup> to consider the variations in acceleration and location of force application:

$$d = \frac{\sin(2\alpha)}{g} \left[ \frac{\bar{P}L}{M_b} \right]^{\frac{2}{3}} \quad (2.2)$$

Replacing  $v^2$  with a ratio of  $\bar{P}[\text{W}]$ , the total average power utilised in the jump;  $L[\text{m}]$ , the distance between the most distal part of the limb and the centre of mass; and  $M_b[\text{kg}]$ , the body mass. In this equation, we see the potential for adaptions that increase jump distance. Firstly, while power must be provided by skeletal muscles, the introduction of elastic potential energy storage mechanisms could allow energy to be released that is stored prior to or during the jump, enhancing jump distance by increasing  $\bar{P}$ . Secondly,  $L$  can be increased through the use of relatively long legs. The power required for a jump is directly proportional to the available acceleration distance, which manifests here in leg length<sup>[2]</sup>. Having a larger body mass is also shown to be a detrimental property regarding jump distance, demonstrating the value of a high specific energy actuation strategy. Locomotive parameters that govern jumping ability are predicted to adapt with increasing body-size to compensate for increase in weight-related muscular skeletal forces by the theory of dynamic similarity. This theory has been shown to have great predictive ability in a number of factors<sup>[14;68]</sup>. Subsequent sections will explore the factors that influence this equation, as well as other factors also impacting the quality of a jump.

Many species (for example: frogs, macropods, locust) have found such success in saltatorial movement that it has became their primary locomotive mode. These species, with a higher tendency to jump, maximise jump performance by exhibiting certain morphological and physiological traits. With the intention to achieve robotic saltatorial motion, it is important from an engineering perspective to understand what these traits are and exactly how they lead to this maximisation of performance.. James et al. (2007)<sup>[41]</sup> note that there is considerable discussion on the most important factor contributing to jumping performance, but suggests that it is unlikely one variable would be a key determinant encompassing all systemic groups and ecological settings. The mechanisms that maximise the efficacy of saltatorial locomotion will be emergent from the coupled, complex interactions of multiple components.

## Natural SEAs

It appears common among jumping animals to employ a method of energy storage, though the strategy is not unique to jumpers. Extending beyond obviously high impulse gaits, elastic elements

are common in animals across phylums. With a minimal weight addition increases in take-off velocity can be achieved through the use of elastic elements<sup>[27;10;41]</sup>. Evolution provides a filtering of ineffective strategies for survival. This cross-phylum evolution is therefore interesting as it demonstrates convergence in evolution, alluding to the efficacy of the strategy. Three major roles for elastic elements in locomotion are identified by Roberts & Azizi (2011)<sup>[89]</sup>:

1. Energy Conservation: Recycling of energy due to gravitational work into kinetic work to improve metabolic economy.
2. Power Amplification (Modulation): Power Production enhancing acceleration type movements (i.e. jumping).
3. Power Attenuation: Absorbing energy with the intention of stopping motion, such as in landing.

All three are advantageous to animals adapted to saltatorial locomotion. Considerable interest is warranted to the power amplification in this discussion as it is the most important for the application to soft-robotic actuators, however all are important considerations.

As power is the ratio of work over time, muscular power is limited by the rate limits of its processes. Elastic elements are purely passive and their function inherent to their structure. This allows the relatively slow muscle contraction to be modulated into a much faster release, thus increasing the transient power output of the system.

Observations of jumping animals show that the power output required for them to achieve their seemingly remarkable jump height far surpasses the power output of the muscle<sup>[12;2]</sup>. The jump of the *Galago senegalensis*, weighing 0.25kg, produced a peak centroid power of 200W. The highest specific power output available instantaneously in a vertebrate was identified in *Rana Pipens* by Lutz & Rome (1994) to be  $371\text{Wkg}^{-1}$ <sup>[63]</sup>. This means the aforementioned Galago's muscle mass to power such a jump would need to be 0.539kg, over double its weight. The impact of this observation is enhanced by the fact that the Galago's extensor muscles are roughly 25% of its body mass, requiring the muscle to achieve 9 times the *Rana Pipens* output<sup>[2]</sup>.

Elastic elements allow an animal to pre-load energy into elastic elements preceding a jump, quickly expending the energy along with muscle actuation to maximise transient power output beyond the capability of their actuators in isolation. This power modulation behaviour appears consistently in literature and across the study of phylums, showing minimal release of power and low jump movement in the early half of the jump before a large release in the later half as a convergent evolutionary strategy for jumping (Figure.2.1).

## Elastic Elements in Insects

Fleas<sup>[11]</sup>, click beetles<sup>[25;26]</sup> and locust<sup>[10;27;108]</sup> are all particularly studied small animals, with varying mechanisms of energy storage, but all following a fairly common theme. All of these animals use power modulation, making the transient release of stored energy possible by use of various catch mechanisms. The nature of this is rather like a catapult, releasing the energy suddenly with high impulse. Muscle output energy can be stored within the elastic elements by locking its ends via the catch and allowing the muscle to only stretch the elastic element, with minimal energy transferred into flexion of the jumping joints, and then released at take-off to enhance power outputs via the transient elastic recoil. This allows slow muscular contraction prior to a jump to contribute to the high impulse jumping motion.

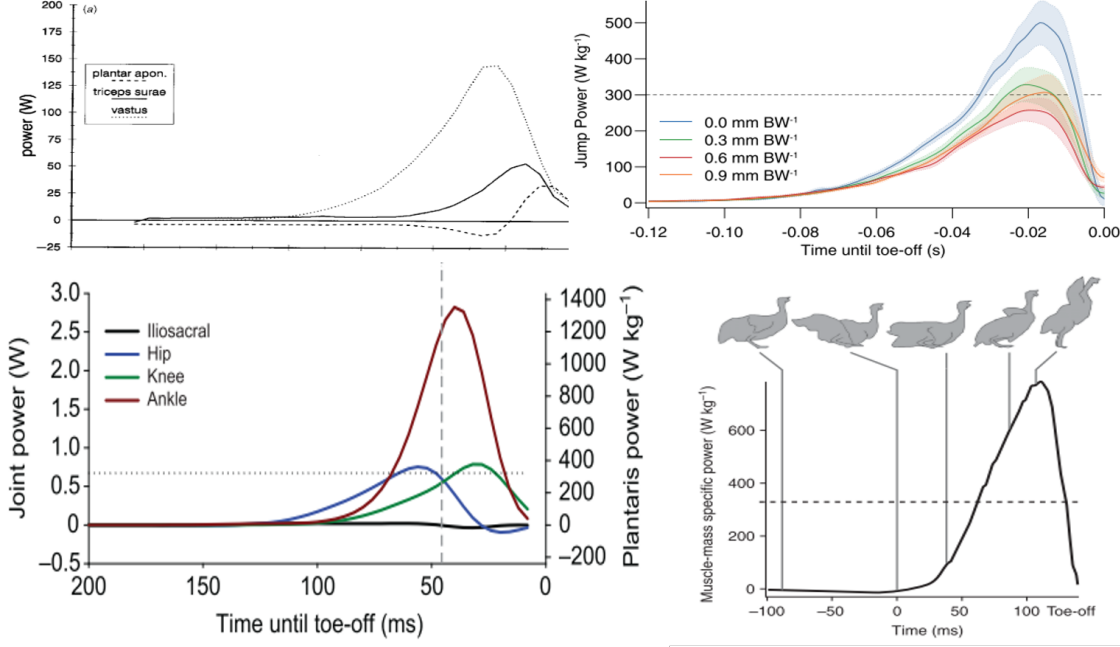


Figure 2.1: Examples of Power Modulation across phyla from literature. Top Left: Galago<sup>[2]</sup>. Top Right: Bullfrog<sup>[88]</sup>. Bottom Left: Leopard Frog<sup>[6]</sup>. Bottom Right: Guinea Fowl<sup>[35]</sup>.

Bennet-Clark (1975) identifies two functions associated with the catch mechanisms observed across insects. Firstly, the catch allows substantial storage of energy in elastic elements, as discussed. Secondly, it allows any antagonists to the jumping motion to be relaxed prior to energy release, so that they do not see damage from the high impulse. Interestingly, Bennet-Clark observes that the locusts without an operational catch were still able to jump, though the absence of the catch was deleterious to jump performance. This serves to highlight that this evolutionary adaptation was not necessary for allowing the jumping locomotion mode, but is crucial in optimisation of its performance<sup>[10]</sup>.

In fleas, energy is stored in a resilin pad, loaded by depression of the metathoracic femur. The loading scheme creates a near negligible mechanical advantage for articulation muscles in the flea, allowing the flea to load the elastic element without joint movement. The energy can be released transiently by another muscle. Species with larger resilin pads are observed to be better jumpers, providing evidence towards the advantage of increasing power modulation through energy storage as a larger pad implies higher energy storage capability<sup>[11]</sup>.

Locusts are efficacious jumpers and also employ an anatomical catch mechanism by placing extensor muscles out of mechanical advantage until the elastic element is loaded<sup>[34]</sup>. Their long legs are well adapted for the locomotion mode and achieve jumping through expeditious extension of the tibiae. Their peak power output during a jump is 75W, producing a peak acceleration of  $180\text{ms}^{-2}$  and a peak velocity of  $3.2\text{ms}^{-1}$ <sup>[10;108]</sup>. Bennet-Clark shows that the locust *Schistocerca Gregaria* stores the energy of 70mg of muscle in stores weighing 4mg per leg. The system of stored energy in the locust increases power 1.5 times of the muscles production capabilities, leading to a power modulation of 10 times. This is achieved with only a 5% weight penalty<sup>[10]</sup>. The *Semilunar Process* is a non-linear spring, named for its crescent shape. Each leg has one semilunar process located in the distal region of the femur. An adult male locust requires 9mJ to jump, while a large

female requires 11mJ. Each semilunar process stores 4mJ energy at the 15N maximal force of the extensor tibiae, in fully elastic deformation; a substantial portion of the needed jump energy<sup>[10]</sup>. The non-linear nature of the Semilunar Process alludes to the complexity of natural systems. Having evolved through random adaption processes, the natural system need not regard dynamical understanding for design and control in the same way a human may need to express dynamics in a language suitable for control development.

## Tendons

Larger animals also make use of energy storage mechanisms, primarily in the form of tendons. Tendons are series elastic. Tendons, along with the materially similar (so much so they are sometimes considered continuous<sup>[106]</sup>) aponeurosis, play a vital role in many acceleration based locomotion modes, passively storing energy from the body's motion under gravity, such as in steady state motion, and storing the work done by muscle fibre shortening or absorbing impacts<sup>[89;10;12;6;31;88]</sup>. Experiments have shown that the importance of tendon elasticity predominates in many muscle structures<sup>[2]</sup>. Tendons are readily accepted to exhibit two distinct regions of their stress strain curves. A compliant 'Toe' region and a linear region following that. The maximum output distal limb muscles, with highly pennate, short fibre construction usually exhibit high fixed-end compliance. Tendons here are long and relatively thin, storing energy well and generating large forces<sup>[88]</sup>.

Lieber et al. (1991) in studies of the frog *Rana Pipen*'s semitendinosus (ST) muscle observed that the tendon in series with this muscle was short in comparison to the Achilles tendon in line with the gastrocnemius. The ratios of muscle to tendon length respectively:  $Ratio_{ST} = 1.5$  |  $Ratio_{Gastro} = 11$ <sup>[61;106]</sup>. The difference between these complexes is their function, the ST being involved in flexion and the gastrocnemius in extension. As the frog is a jumping animal, its likely what is seen here is an indication to the function specific deployment of the tendon: the extensors being heavily involved in power generation for movements of the whole body against gravity requiring significantly more power than the flexing of a limb. This is also noted by Lieber et al. (1991). Investigations into the role of the achilles tendon in *Rana Pipens* also demonstrated that the muscle lengths between the gastrocnemius and the ST varied by only  $\sim 8$ mm, while the tendons varied by  $\sim 5$ mm and the apeoneurosis by  $\sim 15$ mm, in favour of the gastrocnemius<sup>[106]</sup>. The gastrocnemius was identified as the more compliant complex of the two by comparing tendon length/fibre length ratios, though it should be noted that tendon length includes all connective tissue in series with the muscle fibres, including tendon and aponeurosis, considered a single functional unit by Trestik et.al. (1993) due to negligible differences in strain between the two. The gastrocnemius tendon:muscle length ratio was observed as  $3.30 \pm 0.42$  against the ST's  $1.01 \pm 0.19$ , implying function dependant length ratios. with longer tendons being advantageous for distal extensors active in jumping.

Tendons are also observed to exhibit variable stiffness in passive loading and active contraction on short time scales by exploiting the geometric contribution to stiffness. The apeoneurosis portion of the tendon has been seen loaded biaxially by expansion of the muscle belly, changing it's geometry, altering the effective stiffness of the tendon in the longitudinal directions. Azizi et al. (2009) found evidence that in active loading the longitudinal stiffness of the apeoneurosis was increased curvilinearly<sup>[8;89]</sup>. This principle is demonstrated in figure 2.2. They also showed biaxial loading reached 2-3 times greater longitudinal stiffness than uniaxial loading. Arellano et.al (2019) observed a 15% decrease in aponeurosis energy storage and a 34% increase in apparent longitudinal stiffness<sup>[5]</sup>.

Larger animals also see increased jump performance relative to their insect counterparts, with higher jump frequency, speed and height observed. The comparison between the two is fair as Bennet-Clark (1976) posits that the energy - mass ratio of an animal is the deciding factor in jump

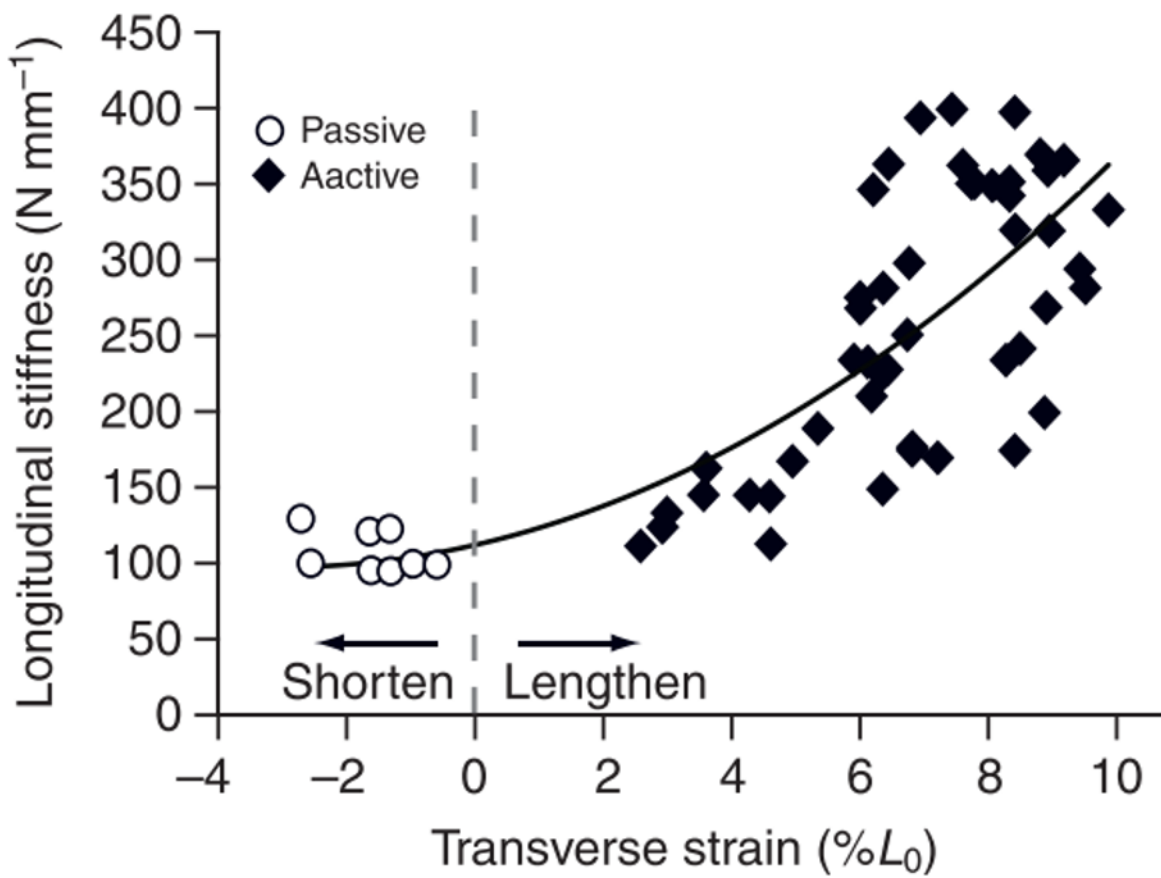
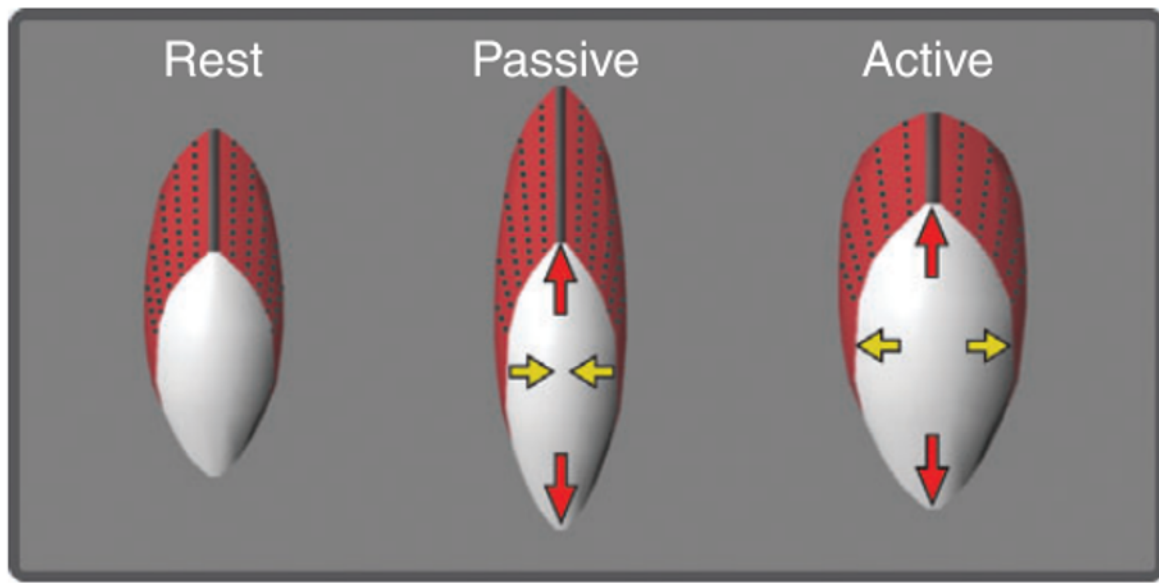


Figure 2.2: Variable stiffness of the aperneurosis and a cartoon demonstrating the loading mechanism<sup>[8;89]</sup>

height<sup>[12]</sup>. The highest reported jump of a bushbaby saw a centre of mass displacement 6 body lengths in magnitude: a 0.250kg animal leaping 2.25m, but as previously mentioned, the muscle power output is not nearly enough to meet the power demands of such a jump.

Unlike insects, no distinct clutch is observed. Instead they make use of a “dynamic clutch” [6] or “Inertial Catch” [90;35]. Effectively, exploiting moments about limbs and ground reaction forces to load series-elastic elements prior to take-off. It is necessary that the tension in the elastic element develops before the majority of joint movement, to avoid the premature release of stored energy and develop the prerequisite for the large power release seen in the last half of the jump.

### 2.1.2 Saltatorial Robots

Jumping robotics have been a goal of many researchers for some time. A number of important metrics are defined in literature that help to evaluate a robotic jumpers performance.

The first metric is “Jump height”. For this work, jump height is defined as the maximum vertical displacement of the centre of mass of a system from the initial height obtained in a neutral stance prior to the particular jump.

Naturally a second metric emerges by considering the horizontal element of a jump: “Jump distance”. This is defined as the horizontal displacement of the centre of mass of the system from the position

A metric comes from Haldane et.al (2016) allows a combination of all the above metrics. In their paper and follow up works, they define the “agility metric”, which aims to capture the jumping ability of a system, be it biological or mechanical, from purely noninvasive measures, building on previous work of standardised performance metrics for comparison<sup>[23]</sup>. “vertical jumping agility to be the height that a system can reach with a single jump in Earth gravity, multiplied by the frequency at which that jump can be made”<sup>[33]</sup>. The vertical jumping agility (VJA [ $\text{ms}^{-1}$ ]) is expressed mathematically as:

$$\frac{h}{t_{stance} + t_{apogee}} \quad (2.3)$$

where  $h[\text{m}]$  is the max height of a jump,  $t_{stance}$  and  $t_{apogee}[\text{s}]$  measure the time spent in stance from actuation onset and the time from lift-off to jump apogee. This expresses the systems agility as a dimensional quantity; an expression of the average climb rate in a gravitational field with repeated jumps. As the quantity has dimensions, Haldane et al. point out that this will be limited by the power-weight ratio of the system. The use of a dimensional quantity is warranted as the relative size of the terrain does not affect the required jump height to conquer said terrain. This is similar to the claim made by Bennet-Clark (1976) when comparing mammalian jumps to insects<sup>[12]</sup>. Jump apogee is the point of zero-velocity. With this, jumps can be seen to terminate at the apogee, and so a ballistic limit is defined as:

$$h \leq \frac{g}{2\omega^2} \quad (2.4)$$

Where  $g[\text{ms}^{-2}]$  is the gravitational constant and  $\omega[\text{Hz}]$  is the jump frequency, capturing the limit as the time in stance approaches 0.

Jumping locomotion requires directional control but also the ability to upright after landing to then jump again. Kovac et al. (2010)<sup>[55]</sup> created an 18cm robot that could jump up to 62cm. From a take-off angle of 75°, it could recover and orient itself. The robot had a mass of 14g. The robot is fairly complex, with many moving parts and connections. Actuation was achieved with a torsion spring that imparted energy into a four bar leg system. A DC motor powers a eccentric cam through a 4-stage gearbox, which charges two springs. Arguably this would reduce the robustness of the design, as each additional part is an added point of failure.

Jung et al. (2016) demonstrated a robot with a mass of 59.4g that could jump 1.62m at a size of 10cm<sup>[45]</sup>. This robot could also crawl, demonstrating multi-modal locomotion. Again; the jumping mechanism is complex and has numerous parts, requiring a gear set and pulley system. This robot also employed an energy storage and release mechanism. While multi-modal locomotion is useful, the paper makes no mention of the robots self-righting capacity. One particularly interesting robot that utilises saltatorial locomotion is the SALTO robot which, along with its successor: SALTO-1P, achieves extremely effective and impressive jumping, allowing continuous jumps to great height. As well as designing SALTO, Haldane et al. (2016)<sup>[33]</sup> also investigated the biological principles that facilitate jumping, taking inspiration from many of the concepts discussed in the previous chapter and particularly paying interest to power modulation and mechanical advantage.

Using their agility metric, the Galago achieved a vertical jumping agility of 2.2ms<sup>-1</sup> and the SALTO robot achieved 1.7ms<sup>-1</sup>. As noted in the previous chapter, Haldane et al. identify the prominence of compliant enabled power modulation utilised by animals for their jumps. They point out that this allows animal systems to achieve greater jumping ability than robots that have higher power density.

SALTO makes use of elastic elements. Identifying the importance of mechanical advantage for power modulation and energy increases utilised by animals, they produced a robot which applies these principles to great effect. SALTO is a monopodal hopper, and leg extension was fixed to be the same as the Galago, as was mass. The intention of the SALTO platform was to experimentally demonstrate the differences between rigid, parallel-elastic, series-elastic and series-elastic with mechanical-advantage actuation (SE-MA) strategies. The SE-MA strategy utilised the dynamic clutch method, starting with a low mechanical advantage to allow loading of elastic elements with minimal limb movement, moving to a high advantage later in the stance to allow release of this energy.

Optimisation was undertaken across all free parameters of vertical jumping agility for two power densities: 10Wkg<sup>-1</sup> and 100Wkg<sup>-1</sup>. The latter is close to the Galago's specific power of 93Wkg<sup>-1</sup>. Using a rigid actuator, the Galago model experienced a height reduction of 60% and a vertical agility of 1.7ms<sup>-1</sup>. Both SEAs surpassed this for a given power density. Their model also showed that increasing the ratio of mechanical advantage at the beginning and end of the stance-phase increases jump height. In the case of 10Wkg<sup>-1</sup> specific power, this increase in jump height did not lead to an increase in agility, as the frequency of the jump diminished in turn. This is due to the relationship  $Power = Force \times Velocity$  which imposes a limit of  $\frac{10W}{1kg \times 9.81ms^{-2}} \approx 1ms^{-1}$  on the jumping agility. However, the 100Wkg<sup>-1</sup> did see increases to jumping agility.

### 2.1.3 Summary

Jumping is characterised by factors relating to the whole system. Limb morphology and the weight of the components extrinsic to jumping play a role in the ability of a jumper. Beyond this, control of a robot is important. Orientation, ability to upright, knowledge of terrain and a sense of self are critical components for jumping. Actuators also need to have high power density in order to minimise weight while providing the large impulses prerequisite for an effective take-off velocity. Jumping robots thus far have seen creative and efficacious development, utilising biomimetics and generating encouraging performance. However, these robots have yet to see deployment to applications, and robotics are not there to simply locomote. In order to accommodate the weight of large sensor arrays, grippers and payloads, the power density of an actuator must be reduced as much as possible. Furthermore, the potential complexity of controlling these robots as they navigate novel terrain is non-negligible. As such, as much of this control should be passive or minimalist, in order

to allow robust and effective translation about novel terrain. Much of this starts in the actuator.

## 2.2 Series Elastic Actuator

### 2.2.1 Robotic Series Elastic Actuators

Origins of the Series Elastic Actuator Paradigm are often credited to Pratt et al.(1995). They looked to series elasticity as a method to mitigate the noise, torque ripple, backlash, friction and reflected inertia from shock loads as a result of the gear trains used in “stiff” actuator. The Series Elastic Element (SEE) gave many advantages. Firstly, acting as a low pass filter to shock loads, it facilitated impact protection for gear trains, despite the SEE filtering the output of the actuator. This was put forward as “an engineering tradeoff”: Heightening the ease of force control when interface resonances are lowered. They also importantly identify the increase in efficiency for legged locomotion through energy storage<sup>[82]</sup>. More broadly, SEAs look to increase the robustness of force control by decoupling the motor units from the environment which allow controllers to observe spring deformation rather than motor current as a more accurate proprioceptive indicator, reducing sensor cost and increasing force control fidelity<sup>[59;104]</sup>. Beyond this, SEAs also facilitate shock tolerance and energy storage/recovery through their compliance<sup>[71;104]</sup>.

An early, linear, series elastic actuator was modelled by Robinson et al.(1999) in the development of a biomimetic walking robot. Their goal was to develop a low motion, high specific force and specific power actuator that would grant impact tolerance while being controllable. They created guidelines to inform future SEA designs, recognising that the spring constant deserves particular attention. They found the choice of spring constant to be a compromise between high spring constant with large force bandwidths and the minimisation of nonlinear friction and impedance with a low stiffness constant<sup>[91]</sup>. These actuators allowed early progress in the 90s and early 2000s for the MIT walking lab such as the spring flamingo<sup>[83]</sup> and the M2 humanoid robot<sup>[79]</sup>.

Many SEAs use lead screw based systems which are bulky and incur high friction interactions<sup>[82;91;101]</sup>. Rotary torsion springs have been used in order to reduce the form factor of the actuator, potentially allowing their use in human locomotion assistance applications<sup>[54;102]</sup>. These efforts however appear to still suffer from a trade off between power density and form factor.

Sergi et al.(2012) developed a SEA with a torsional spring and impedance control. Their design weighed 1.8kg, a significant amount of weight to be worn by as a knee assisting actuator<sup>[102]</sup>. This actuator was later integrated into a treadmill mounted system. It is unlikely the actuator in it’s current configuration would see application in a fully mobile system due to it’s bulky form factor and weight. The design is also complex, involving many interacting and rigid parts which may be prone to shock damage, even with the SEE in place and potential failure points are numerous with more interacting parts. Many interactions also give rise to Joule heating which may be uncomfortable if not properly insulated.

The MIT cheetah robot utilised an SEA with proprioception<sup>[110]</sup>. This robot is multi-modal; able to walk, run and jump. The first version of this robot could trot at speeds up  $6\text{ms}^{-1}$ . Their actuator unit used two actuators with a gear train located at the hip, rather than having actuators present at the joints, as a mechanism to minimise the total moment of inertia. This highlights the need for unorthodox configurations when using traditional actuators with relatively low power/weight ratios compared to the later discussed soft robotics. In this paper, they define a metric known as the *Impact Mitigation Factor* (IMF) that quantifies the effectiveness of a mechanism’s free-dynamics at reducing impact impulses. They noted that the introduction of compliance through a series elastic element affects overall compliance, interestingly altering the value of the SEE’s stiffness

does not. This is because a compliance temporally distributes an impact, the stiffness governs the spread of the impulse and does not change the initial impulse. The advantages to IMF from SEA's were highlighted by the authors, looking at theoretical modifications of including SEAs at joints to the MIT Cheetah and another robot: HUBO KHR-4. Their results showed that averaged over all the theoretical designs presented the MIT Cheetah operated at 90% of its theoretical SEA counterpart's IMF, while the HUBO KHR-4 operated at 52% of it's own counterpart. This demonstrates the efficacy of SEA's at reflecting impact inertia, a crucial consideration in locomoting robotics.

Haldane et al's. (2016) work on series elastic power modulation identified the crucial inclusion of power modulation through series elastic elements to jumping robotics. Their actuator combined series elastic with mechanical advantage to great effect. A brushless DC motor was paired with a torsional spring<sup>[33]</sup>. This spring was made of latex and is not the only example of SEAs utilising soft materials and their higher energy storage per unit mass. Soft springs allow for non-linearity and higher torque resolutions to be introduced for a lower weight cost without the need for complex and intricate mechanisms. They do however introduce hysteresis if viscoelastic effects are present and lose the fast response of stiffer mechanisms<sup>[7]</sup>.

In summary, SEAs are a paradigm with potential to improve traditional robotics and their control methods. They also expand the feature space through the introduced compliance with shock absorption, power modulation as well as energy storage and recovery. While current designs are effective, often they have large form factors and many complex interacting components, decreasing their robustness and applicability to locomotive and human interactive applications<sup>[60]</sup>. Across the literature, no SEAs appear to be fully soft, despite the inclusion of soft spring elements. The majority also appear to be bulky and complex mechanisms. Introduction of actuators to human interaction systems or to systems with locomotive autonomy can improved by creating SEAs with higher power density, lower overall weight and form factor and using soft materials. In order for a robot to achieve effective autonomy, robustness and weight are key factors. Complex mechanisms come with more potential failure points and the hard interactions of many mechanisms induce significant friction, leading to wear with repeated actuation. In remote environments where a robot is operating in isolation, these considerations gain extra validity as repair or replacement of components is a rare privilege or simply not feasible.

### 2.2.2 Variable Stiffness Actuators

The previously mentioned trade-offs between higher compliance actuators and their stiffer counterparts have seen mitigation through the use of VSAs , a subgroup of the Variable Impedance Actuator paradigm<sup>[113;107]</sup>. These actuators allow controllable, dynamic tuning of a SEE to suit the needs of the controller at the specific moment. Methods of achieving the stiffness variation include the variation of SEE preload, the output and spring's transmission ratio or somehow influencing the physical properties of the spring<sup>[113]</sup>. Spring preload variation is cited as the simplest method in the review given by Wolf et al. (2016). This can be achieved through co-contraction of antagonistic spring systems but comes with the drawback that the spring can not be used to store VSA output energy until the preload is released. Alterations of transmission ratio affect directly the passive displacement of the spring, reducing the outputted spring rate but not reducing the potential energy storage when changing the stiffness setup. These mechanisms are usually complex (figure.2.3 and costs of antagonistic VSA's are higher , most requiring at least two motor units and their respective gear trains. As there is energy flux between kinetic and potential energies frequently in VSA articulation, it is necessary for these transformations to be efficient. Friction in actuator mechanisms incurs non-negligible losses and the drive train efficiency between the springs and links becomes relevant in oscillatory movements where motors are mostly inactive<sup>[113]</sup>. With

more interacting components the robustness of an actuator decreases.

### 2.2.3 Summary

It seems that elastic elements working in tandem with muscle is a valuable mechanism giving rise to a natural systems effective locomotion. Through modulation, the transient release of power can be achieved beyond the usual ability of natural muscle. Elastic elements also allow for the protection of natural muscle by absorbing impact energy and can then translate this back into useful work. Beyond this, natural elastic elements can also vary their stiffness, dynamically altering the trade-off between impact absorption and the effective translation of force. These features have been sought in engineered SEAs to some success. However, these systems are currently bulky and complex, requiring gear trains and often sub-assemblies for the motors to convert rotational motion to linear actuation. This creates heavy actuators that may be less robust than a relatively simple SEA using linear actuators. To compliment a jumping application, interfaces behind hard components that can transmit impacts should be reduced and the specific power outputs maximised through weight reductions. Furthermore, utilising a compliant actuator unit in tandem with the compliant series elastic element appears minimally researched. The development of a fully soft VSA is a target for research in this project and will hope to address both the complexity and robustness considerations of current VSAs while also utilising the biomimetic principles found from nature.

## 2.3 Soft Robotics

Soft robotics is so called after the desired compliance inherent to materials and engineered into the designs. They are often defined by the material properties and usually adopt moduli in the range of soft biological materials<sup>[58]</sup>. Traditional, 'harder' robotics can apply large forces and move very quickly, but this is detrimental to collaboration with people and interactions with fragile objects and can also incur significant investments in materials and control<sup>[111]</sup>. Soft robotics introduce compliance through relatively simple material substitutions that allow for an embodied intelligence. Gripping a fragile object, a soft manipulator could adapt to variations in density simply through it's material compliance and the stiffness contrast of the impedance and the actuator, removing a considerable burden from the controller<sup>[39]</sup>. The soft materials also increase the capacity for safe human robot interaction by the same means<sup>[111;81]</sup>.

Addressing locomotion in novel terrain may benefit from the compliances of materials, allowing an actuator to comply to an impedance, reducing control complexity often needed with hard actuation. However, control of soft actuators still remains an issue due to the non-linearity associated with soft materials as well as the potential for hysteretic behaviour. Sensing methodologies are also challenging as a non-compliant sensor will interfere with the soft robots desired compliance.

### 2.3.1 Dielectric Elastomer Actuators

Dielectric Elastomer Actuators (DEAs) are the precursor to HASEL actuators used in this work and use the same primary actuation mechanism. By exploiting the Coulombic attraction<sup>[38]</sup> developed by establishing a potential difference between two electrodes which pulls them together through the electrostatic forces of attraction. These electrodes are located on opposing faces of a compressible membrane so that the membrane is deformed as the electrodes experience this force and mechanically displace. DEA actuators, and their derivatives HASELs and Peano-HASELs, make use of Maxwell stresses to induce Maxwellian pressures<sup>[1;95;38;117;42]</sup>. These are stresses that

come about in matter as a result of electric fields, shown by the Maxwell Equations of electromagnetism<sup>[38;42]</sup> and can also be thermodynamically derived from the isothermal equations of state of an ideal transducer<sup>[117]</sup>. The equation for a Maxwell stress ( $\sigma$ ) perpendicular to the electrode surface resulting from its field is given by:

$$\sigma = \frac{1}{2}\epsilon_0 E^2 \quad (2.5)$$

where  $E$  is the electric field between the two electrodes,  $\epsilon_0$  is the vacuum permittivity. This mechanical force deforms the DEA and creates the actuator's force. Typical elastomers employed are “Acrylic, Silicones, Polyurethanes (PU) and Rubber.”<sup>[24]</sup> and it is critical that the material is flexible. Moreover, elasticity is preferential to avoid hysteresis effects with repeated actuation. Attributes and disadvantages vary by material and are application specific. For example, silicone and PU elastomers are mouldable to a number of shapes and degrees of softness, do not often require pre-stretching and have fast response times<sup>[24]</sup>. Though strain production is relatively low and the permittivity of silicones requires higher voltage stimuli, reducing the autonomy of a system. Research on these actuators reports high strains (> 100%), high efficiencies (> 80%), energy densities and self-sensing. Combination effects of multiple actuators and integration with frames can improve force output. Models for simulation have been demonstrated to be accurate and applications in artificial muscles. Though these attributes are promising, DEAs require large voltages in the kV range and suffer from leakage currents, which can cause electrical breakdown in the dielectric<sup>[17]</sup>. This damages the dielectric and has deleterious performance effects<sup>[24;1]</sup>. Stacked actuators require large areas of dielectric, prone to electrical failure according to Weibull distributions for dielectric breakdowns<sup>[56;115]</sup>. Silicone sponges swollen with silicone oil showed continued operation post breakdown, but strains were below 5%<sup>[37;1]</sup>. Research has been conducted in low voltage DEAs which have shown functional actuation at 450V with strain values up to 25%<sup>[44]</sup>. Application of voltage also expands the actuator and consideration of the passive state of a system is required to make this compatible with limited power supplies.

### 2.3.2 Hydraulically Amplified Self-Healing Electrostatic Actuators

HASEL actuators, akin to the DEA actuators to which they are a subset, use the same mechanism of Maxwell stress to create actuation. However a HASEL actuator consists of a shell which contains a fluid which is displaced by the contraction of the electrodes. This creates a pressure on the shell and deforms it. This mechanism is therefore referred to as Maxwell Pressure in literature. By coating an elastomer shell, filled with a fluidic substance, partly in electrodes, then establishing a potential difference which generates electric fields within the dielectric, the dielectric is forced into free volumes by this mechanism as the volume between the electrodes is reduced by motion of electrode attraction. This increase in fluidic density generates a pressure which deforms the elastomer shell. Influence is exerted by the deformation pushing or pulling on the intended actuation object, and designs are customisable for a variety of actuation modes by electrode placement and actuator geometry. In a HASEL actuator, at a particular voltage, the Maxwell stresses exceed the restoration forces imposed by the elastomer; at this point the electrodes pull together abruptly. This is voltage threshold is called the “pull in voltage”.

The Maxwell stress (and, therefore, the Maxwell Pressure) is proportional to the dielectric permittivity ( $\epsilon$ ) of the medium between the electrodes and the magnitude of the electric field ( $E$ ). The relationship is given by (2.6)<sup>[38;117]</sup>:

$$P_{Maxwell} \propto \epsilon E^2 \quad (2.6)$$

While DEAs are evidently applicable actuators, they suffer from unrecoverable senescence. High electric fields potentiate dielectric breakdown events which produce aging or sudden failure. To overcome this, Hydraulically Amplified Self-Healing ElectroStatic (HASEL) actuators have been developed, combining soft fluidic and electrostatic actuators. HASEL actuators use liquid dielectrics in polymer shells to facilitate self-healing<sup>[1]</sup>, opposed to the solid dielectric in DEAs. When a dielectric breakdown occurs between electrodes, material in the path is vaporised as the voltage exceeds the dielectric strength of the material. In solid dielectric, this creates a cavernous channel that remains in the dielectric, reducing performance or facilitating failure from short-circuiting. Liquid dielectrics will flow to fill voids left by breakdowns, thus self-healing<sup>[1;50]</sup>. Elastomer shells do not self-heal; but do self-seal<sup>[95]</sup>, this means that breakdown events still have a deleterious impact, be it substantially mitigated by liquid dielectrics. However, liquid dielectrics are not immortal. Cavities such as bubbles form after a breakdown, which have low breakdown strength. These will lead to a small but non-negligible increase in breakdown occurrence. Suggestions for improvements are made by Rothermund et al. (2020) proposing incorporation of mechanically self-healing and/or gas-permeable elastomers that would allow bubbles to escape from the actuator. Acome et al. (2018) showed breakdown events were observed at an average voltage of 23.8kV, with a minimum of  $\sim 18kV$ . Over 50 breakdown events, the first and last breakdown events occurred within 0.3kV of one another (1st : 29.0kV/50th : 29.3kV). In fig.1F<sup>[1]</sup>, it would appear that later breakdowns were more biased to be below average, with a high density of occurrence around the 20kv region. Arguably, the average in the 35  $\rightarrow$  50 event range would be significantly lower than when viewed holistically.

HASEL actuators, like DEAs, exhibit self-sensing. HASEL actuators are essentially deformable capacitors. As the separation of the electrodes is the mechanism by which the actuator produces force, a relationship between this separation and the displacement of the actuator or its force can be combined with the elementary equation for capacitance ( $C$ ) between parallel plates with a dielectric medium of relative permittivity  $\epsilon_r$ :

$$C = \epsilon_0 \epsilon_r \frac{A}{d} \quad (2.7)$$

where  $A$  is the electrode area and  $d$  is their separation. By passing a low amplitude AC voltage, superimposed on the high-amplitude actuation voltage, the impedance can be analysed to provide sensing of deformation<sup>[1;50;95]</sup>. This is possible as the capacitance of the actuator is a function of its geometric properties. The area of compression by electrodes mimics a parallel plate capacitor and can be approximated as such:  $C \propto \frac{A}{d}$  where  $C$  is capacitance,  $A$  is electrode area and  $d$  is the inter-electrode distance. As this compression is the mechanism which creates actuation, the capacitance gives an inference of the actuators geometric state, which can allow the accurate approximation of strain and force outputs.

Kellaris et al (2018) compared optical to capacitive datasets against position data for a peano-HASEL (PH) actuator under a varying voltage stimulus. By using a constant scaling factor, they observed reasonable agreement between the data sets<sup>[50]</sup>. Discrepancies were observed, implying a non-linear strain/capacitance relationship. This minimalist and non-invasive proprioceptive capability facilitates a solution to the commonly cited problem of sensing often discussed in soft robotic literature. Sensors must be soft or non-invasive themselves in order to not interfere with the actuation and the data they collect must be representative, a challenge in a functionally infinite DOF system.

HASELs, like soft-hydraulic actuators, allow design and actuation-mode freedoms. However, HASEL actuators generate their pressure locally by electrostatic forces<sup>[1;95]</sup>. This removes the need for bulky equipment like compressors, fluid reservoirs, pumps etc, seen on other fluidic actuators,

making them light weight and easily integrated (sans power supplies).

However, High voltage stimulus requirements still remain an issue with HASEL actuators. Acome et al. (2018) recognise this in their paper, citing the thick elastomer shell as a source of the required high actuation voltages. They do provide a potential solution, proposing the use of higher permittivity dielectric layers, which from equation (2.6) would increase Maxwell Pressures, and advanced fabrication techniques to produce high-resolution dielectric structural features.

Average specific power values range from  $80Wkg^{-1}$  (High Strain-PH) to  $180Wkg^{-1}$  (PH), with  $337Wkg^{-1}$  recorded at resonance for planar HASELs. For comparison, Mammalian skeletal muscle has an average specific power of  $50Wkg^{-1}$ . Linear strains up to 124% have been reported for planar HASELs at resonance and quadrant donut HASELs have shown 118% linear strains. Robustness tests from Acome et al.<sup>[1]</sup> of these actuators have shown negligible deterioration after 1 million cycles (with strains of 15%). Stacks of donut HASEL actuators have been used for robotic grippers and planar HASELs can displace 4kg objects with strain values of 69% when applied in parallel<sup>[1]</sup>.

In experiments comparing HASEL to DE actuators, Acome et al. showed that under 11kV voltage stimulus, HASEL actuators saw almost a 4 fold increase in area strain compared to DEAs ( $\frac{46\%}{12\%}$ ). The rate of area strain with voltage stimuli was much steeper for HASEL than DEA. Divergence was observed around 3kV. This demonstrates that HASEL actuators not only address the problems of DEAs but outperform them, with experimental control for dielectric thickness and elastomer material (Ecoflex 00-30). It should be noted that these strains were achieved way below the dielectric breakdown voltage average and below the minimum value (from the experiments in Acome et al.<sup>[1]</sup>).

High voltage stimulus requirements still remain an issue with HASEL actuators. Acome et al. recognise this in their paper, citing the thick elastomer shell as a source of the required high actuation voltages. They do provide a potential solution, proposing the use of higher permittivity dielectric layers, which from equation (2.6) would increase Maxwell Pressures, and advanced fabrication techniques to produce high-resolution dielectric structural features.

### 2.3.3 Peano-HASEL Actuators

HASEL actuators require stretchable materials. This contributes towards manufacturing complexity and cost as electrodes and dielectrics must be compliant to this stretch. Stretchable material variations are also limited. Peano-HASEL (PH) actuators address this, instead using inextensible but flexible shells<sup>[50]</sup>. HASEL actuators are combined with Peano fluidic actuators<sup>[76]</sup>, to create a linearly contracting actuator. To generate pressure, again the Maxwell pressure is used to create contraction between two electrodes. The electrodes start at one edge of the pouch and progress inwards towards the middle, contracting progressively with a *zipping front*. As the zipping front progresses, the liquid dielectric is forced into the unzipped, free region of the actuator. The containing film is deformable but inextensible allowing the increased fluidic density in a decreasing volume to cause a change in the pouch cross section from the resultant pressure. It is this deformation which provides the contraction. The linear contraction and electronic stimulation provide comparison to natural muscle, which also uses electric control signals via motoneurons and achieves linear contraction. A visualisation of this mechanism is given in figure.2.6. PH actuators exhibit complex deformation modes when wrinkling occurs in the film shell. This traps fluid and causes inhomogeneous out-of-plane deformations near the zipping regions of the actuator, reducing the possible strain output and affecting the roll off frequency. However, Kellaris et al. (2019) observed that under high loads, their actuators performed better than theoretical models. They attributed this to these instabilities, noting that rotation was also observed about the free end of the actuators, simultaneous with contraction<sup>[49]</sup>. Thus zipping areas are larger for the same actuation strain,

increasing force output as a result. Peano-HASELs inherit the HASEL's electrical stimulation properties being renewable and highly controllable, but restricted by the voltage and energy density of the power source. This is particularly troublesome with the high actuation voltages present, on the order of kV, though this may be mitigated with material choices for dielectric and shell.

**Materials** Due to the inextensible nature of the shell, PH actuators removed the instability observed in HASEL actuators and provide smoother, progressive zipping, avoiding the pull in voltage threshold standard HASELs exhibit. Once the activation voltage is exceeded, electrodes zip controllably and in accordance to applied voltage<sup>[95]</sup>. PH actuators suffer from observed complex motion modes when wrinkling occurs in the film shell. This traps fluid and causes inhomogeneous out-of-plane deformations near the zipping regions of the actuator, reducing the possible strain output but also affects the roll off frequency. However, Kellaris et al. (2019) observed that under high loads, their actuators performed better than theoretical models. They attributed this to these instabilities, noting that rotation was also observed about the free end of the actuators, simultaneous with contraction<sup>[49]</sup>. Thus zipping areas are larger for the same actuation strain, increasing force output as a result. Wang et al. (2020) replaced BOPP shells with thermoplastic polyurethane (TPU) for High-Strain Peano-Hasel (HS-PH) actuators, which are more compliant<sup>[109]</sup>. TPU shells had three times the relative permittivity compared to BOPP; however the shell was twice as thick, so similar load-strain characteristics were expected. TPU could achieve  $1.71 (\frac{16.03\%}{9.36\%})$  times the strain of BOPP at 10kV lifting a 0.2N load. TPU lifted lower loads in low strain regions than BOPP. Wang et al. attribute this to liquid dielectric trapped by buckling traces in regions of the shell, which prevented uniform electrode zipping. The differences in actuation performance observed by a change of film material allude to the opportunities provided by a well chosen materials with respect to actuator some performance metrics, but also highlight that this will incur deleterious effects in others. Breakdown voltage is also a material specific variable<sup>[109;70;50;49]</sup>, the probability of breakdowns is reduced with better breakdown voltage. This tackles a particular failure mode of the actuators: breakdowns across the heatsealing bonds between sheet films<sup>[96]</sup>. The change in force-strain characteristics and efficiencies when Wang et al.<sup>[109]</sup> made the switch from BOPP to TPU also demonstrate the potential in carefully selected materials for improving performance of actuators. Rothemund et al. in their review of HASEL actuators suggest that materials with higher dielectric constants and breakdown strengths would increase specific energy<sup>[95]</sup>. Suggestions for materials such as PVDF-Terpolymer, with  $\epsilon_r = 50$  and breakdown strength  $E = 600V\mu m^{-1}$ , could raise specific energies for PH actuators up to  $20000Jkg^{-1}$ , based on a model from Kellaris et al<sup>[49]</sup>. For reference, skeletal muscle achieves  $40Jkg^{-1}$ . While exciting, these models are primitive, first principles models which neglect many important effects in actuators such as dielectric viscosity which has significant effects on actuation frequency response, speed and efficiency.

Material properties are also linked to the required voltage stimulus. As the Maxwell Stress is proportional to  $\epsilon_r E^2$ , an increase in dielectric permittivity would decrease the required field strength, and thus the voltage stimuli.

The challenge is finding the balance of material properties that meets the optimal configuration. For this application, the actuator will be operating over a wide temperate range, subject to radiation and in the case of the Moon, exposed to very near vacuum. The impacts of these environmental factors are significant and diligence must be paid to them when selecting materials.

An advantage of PH actuators over traditional HASELs is the acquirement and variability potential of materials, due to flexible materials being more numerous than stretchable; and they allow for fabrication compatible with existing industrial methods such as heat sealing<sup>[70]</sup> or laser sealing<sup>[112]</sup>, reducing startup manufacturing costs and increasing attainability. Moreover, Kellaris et al.

(2018) report their actuators cost  $\sim \$0.10$  in materials, using biaxially orientated polypropylene as a film material, conductive hydrogel as electrodes and Envirotemp FR3 vegetable based transformer oil as dielectric<sup>[50]</sup>. They also note that in large scale manufacturing this cost would significantly decrease. This low economic cost in infrastructure modification and material acquisition may allow access to robotics to communities that would otherwise be excluded, such as rural farming communities and natural environmental conservation operations for example. Dispersed and accessible robotics may have wide reaching ecological benefits by facilitating new farming methodologies and consistent environmental monitoring. Another benefit of these traits is the ability to rapidly prototype novel actuators, which can lead to unexpected advances when offered to a wider creative pool.

**Geometry** The current statics models for Peano-HASEL actuators were derived by Kellaris et.al (2019) from a geometric parameterisation and a minimisation of free energy. An angle,  $\alpha$ , whose variation gives rise to the dynamics of the system.  $\alpha$  is defined from the longitudinal axis of actuator and the film moving away from the actuators tip. The geometry is given by fig.2.7. It was assumed that, with an optimal filling of dielectric oil, the cross section of the actuator when the electrodes of the actuator are fully zipped would assume a circular profile, outputting the maximum strain geometrically feasible. The optimal fill of the actuator is calculated from this circular profile. This is an insightful perspective, allowing observations of the impact of geometric design parameters on limits of actuator performance. These observations are however limited to equilibrium states, derived with respect to the tip angle  $\alpha$ , and do not address the temporal evolution of states. Moreover, they omit higher order derivatives of displacement invaluable to actuator design and implementation.

Minimisation of the free energy function derived from this model provides the relationship between the actuator's geometric deformation and it's outputted force,  $F$ :

$$F = \frac{w\epsilon_0\epsilon_r V^2}{4t} \frac{\cos(\alpha)}{1 - \cos(\alpha)} \quad (2.8)$$

where  $w$  is the actuators width,  $t$  the shell thickness,  $V$  is the stimulation voltage and  $\epsilon_0$  and  $\epsilon_r$  carry their usual physical meanings. From this equation it is clear that two geometric parameters play key roles in the actuators force output. Gains can be made through reductions in the film thickness,  $t$ , used to construct the actuators shells and by increasing the width,  $w$ , of the actuator. Notably, the actuators filled length  $L_p$  as well as it's unfilled height  $h$  are both absent from this equation. This means one may reduce this parameter to the limits of manufacture. A reduction in  $L_p$  would reduce the maximum stroke length of the actuator. This can be resolved by chaining multiple actuators in series. As the actuators are relatively light with respect to the expected loads, this incurs minimal performance penalties and allows for increases in specific energy without losses of performance; a highly favourable scaling behaviour, shown in Fig.2.8a.

From this behaviour it follows that, maintaining a certain stroke length, a single pouch of mass  $m$  and pouch length  $L_p$  may be reduced to  $n$  pouches in series, with single pouch masses scaling as  $\frac{m}{n^2}$  and pouch lengths scaling as  $\frac{L_p}{n}$ . The overall mass of the actuators is reduced by the relationship  $\frac{m}{n}$ .

There is a limit to this behaviour. As  $L_p$  becomes small, the effects of bending stiffness begin to manifest. This causes a peak in the scaling behaviour of specific energy before a rapid decline, as shown in Fig.4.3c. Force also scales as  $nF$  by adding  $n$  parallel fibres, as shown in figure.4.3a. Combined with the above scaling behaviour, the form factor of an actuator array can be maintained while still heightening force output. This relationship is demonstrated in Fig.2.8b.

To summarise the three identified geometric scaling predictions for the PH actuator:

1. The force produced by the actuator is independent of the pouch length  $L_p$ . This is seen from the absence of the term in equation 2.8. This can be reduced to minimise actuator mass and increase mass specific attributes such as energy output. and can be realised in series combinations of PH pouches.
2. Combinations of  $n$  series actuators into parallel arrays gives direct scaling of force:  $F_n$  but crucially not the blocking force  $F_b$ .
3. The two scaling properties combined allow for consistent form factors to be maintained while increasing actuator force output.

**Dynamics** Rothemund et.al(2020) studied Peano-HASELs transitioning between inertial and viscous domains of actuation response. The transition between these regimes is governed by the viscosity of the liquid dielectric. The inertial regime in the limit where the viscosity  $\rightarrow 0$  sees the actuated masses inertia dominate, giving rise to an overshoot of a set actuation strain before a slow decay of minor oscillations. In the other limit, viscosity  $\rightarrow \infty$ , the strain response sees a slow ramp up and a slow release when stimulation is applied and removed respectively. Understanding these regimes is a critical component of actuator implementation. It is mainly a material effect, however geometry is non-negligible. The equation of motion for the actuator was derived from a Lagrangian approach by Rothemund et.al(2020)<sup>[96]</sup>. Like the previous model, it is assumed that one may neglect the electrical energy stored in the electric field in the unzipped region, a valid assumption as the electric field rapidly decays in this region<sup>[87]</sup>. This model however fails to provide actual equations for  $\alpha$ 's time derivative. Knowledge of this derivative is of high interest from a design perspective of any actuator and especially a SEA.

**Applications** Stacked PH actuators have also been demonstrated by Mitchell et al. (2019) to create a modular actuator<sup>[70]</sup>. Actuators were constructed in sheets and then folded to layer the actuators one above the other. Not only was this simple to manufacture, allowing rapid prototyping and experimental variation, but also demonstrated strain values of 110% for 8 actuators and a maximum force of 33N with stimulus of 8kV constructed from BOPP and Carbon Ink electrodes. Mitchell et al. also note that the stack/folding method is not limited to the module design they used, citing the quadrant donut shape explored in the same paper as an applicable module. These donut actuators build on designs presented for HASEL actuators by Acome et al. (2018)<sup>[1]</sup>. The donut actuator was initially dimpled to instigate zipping, then made into a quadrant actuator to reduce inhomogeneous dielectric distributions during zipping, also improving initiation of zipping. While the dimpled donut had higher strain rates in the 8  $\rightarrow$  10kV range when alone, with peak strains of  $\approx 58\%$  for dimpled and  $\approx 40\%$  for quadrant (at 10kV), in a stack of 3, the quadrant donut far outperformed a similar stack of dimples by a significant margin. Quadrant stacks showed strains of  $\approx 72\%$  at 10kV, compared to  $\approx 20\%$  for dimpled designs.

Stacks of actuators in parallel have been demonstrated allowing 3D continuum control with a human operated maze game solved by actuating stacks of HASEL with varying voltage stimulus for each stack, controlled by joystick<sup>[70]</sup>. 3 stacks of 5 HASELs were used. The same stack configuration was given a robotic gripper that showed reliable soft-grip, as well as object manipulation. The gripper was adapted from a scorpion tail proof-of-concept for curling HASEL actuators and placed on top of the stack.

Geometry optimisation also has impacts on the problem of requiring large electric fields for actuation, which, though not exclusively, is a geometric problem. Alternative geometries and dielectric thickness are cited as possibilities for decreasing the needed actuation voltage<sup>[50]</sup>.

## Current Peano-HASEL Control

A disappointing reality of soft robotics is the very attributes that give rise to their favourable properties of compliance, embodied intelligence, continuous deformation also create difficult problems for control. Functionally, soft robotic actuators are stochastic in respect to a finite state representation due to being essentially infinite degree of freedom systems with highly nonlinear dynamics and hysteresis<sup>[20]</sup>. Solutions for robotic control problems are often in rigid body regimes and these breakdown without heavy modifications for soft robotics, which are more faithfully represented in a continuum mechanics framework<sup>[92]</sup>.

While control of soft systems is not impossible, high fidelity models are often needed, incurring expensive computation costs and requiring accurately identified system models, making them limited in application<sup>[20;21]</sup>. It is important if soft robotics are to depart the laboratory that they have applicable and robust control schemes.

The problem of control becomes yet more onerous with the introduction of an SEE, itself carrying a complex physical response. The operation of characterising such a system would be considerably arduous, let alone the task of controlling it. The systems primary output is a force at the end of a tendon; it's inputs the voltages used to stimulate the PH-Muscle. To move through this system requires the consideration of non-uniform electrostatic zipping; the potentially viscoelastic and thermoelastic physics of the film; hydraulic action of the dielectric oil and it's hysteresis; the material interfaces between the PH-Muscle and SEE; and the desired non-linear dynamic responses of the SEE with it's own hysteresis. Machine learning control is a potentially necessary step in controlling soft robotic systems as they lend themselves well to capturing non-linear and complex physics<sup>[52;20]</sup>. It is hypothesised that this method will be applicable to the PH-VSA. A major limitation to soft robotics also lies in their difficult interactions with sensors. The Peano-HASEL actuator shows a direct relationship between the amount of zipped electrode and it's stroke. Much like all DEA derivatives, it is possible to model the actuator as a capacitance,  $C$ , in parallel with a resistor that models the leakage current through the dielectric membrane,  $R_m$ . The parallel arrangement is then connected in series with a second resistor,  $R_e$  representing the electrode resistance (Figure.2.9)<sup>[93;29]</sup>. The values of these can be computed in real time using appropriate sensing circuitry and algorithms<sup>[28;95]</sup>. These models can even capture hysteresis in DEAs<sup>[19]</sup>. The scalability of this system to large arrays of PH-Sarcs in PH-Muscles has yet to be tested, however there has been progress in the miniaturisation of the circuitry<sup>[64]</sup>. The kinaesthesia exhibited by Peano-HASEL actuators provides compelling mechanism to provide feedback to closed-loop control algorithms and has indeed been used in literature<sup>[50;94;1;100;46]</sup>. Experiments have shown good evidence of the accuracy of this sensing method without machine learning in simple tasks, such as the positioning task in Figure.2.10<sup>[19;50;64;28]</sup>. The combination of machine learning-like control with the self-sensing proprioception has been used before on DEAs by Cao et al.(2018). Their results showed good accuracy on positional control and was achieved through experimental elucidation of dynamics.<sup>[19]</sup>. However, the technique has not yet been applied to Peano-HASELs and their extension to an SEA/VSA and while these results are promising, they are performed under idealised experimental settings. Online control will need to adaptable and operating beyond these time scales and assumptions, probably in the form of non-linear systems. This will likely require a more stochastic and statistical approach.

## Peano-HASEL Nomenclature

A brief note is made here on nomenclature for future discussion. In order to provide distinction between the types of combinations of Peano-HASEL units in this work, a nomenclature mimicking

natural muscle is adopted. The single unit, the Peano-HASEL actuator minor, is known in this work as a *PH-Sarcomere* (Sometimes PH-Sarc). The PH-Sarcomeres linear arrangement in series is referred to as a *PH-Fibre* and the 3D array of these fibres in parallel a *PH-Muscle*. In this work, Peano-HASEL Muscles are defined by a *signature* (Figure 2.11):

$$\text{PH-Signature} := [N \mid n \mid w \mid L_p \mid f] \quad (2.9)$$

where  $N$  is the number of parallel PH-fibres,  $n$  is the number of PH-sarcs per fibre,  $w[\text{mm}]$  is the actuator width,  $L_p[\text{mm}]$  the length of the actuator and  $f$  the electrode coverage ratio.

### 2.3.4 Summary

The peano-HASEL actuator presents a highly tuneable design space and potential for scalability. The actuators are however infantile in their research lifespan, and have yet to see much expansion into larger actuation systems. The dynamics of the actuator, at the intersection of electrical, polymer and fluidic domains, are complex and are still being understood. The lack of discussion around temporal dynamics, particularly the absence of  $\dot{\alpha}$  provides a line of research. Investigation into an analytical model containing similar parameters as the model presented by Kellaris et. al (2019) would greatly improve understanding of the impact of changing these parameters in design. The scalability of the peano-HASEL mimics that of natural muscle, with large arrays of actuation units generating large scale forces and strains. Natural muscle also operates within the optimum regions of its dynamics, seen in the sarcomere length tension curve. This is a lesson that may be needed in designing with Peano-HASELs due to the trade-offs between force and strain, and the inertial/viscous regime transition<sup>[97]</sup>. The effect on rise time depending on regime nature alludes to yet more design optimisation considerations. However, the Peano-HASEL possess potential for the foundation of applications and expansions, even in its infancy.

## 2.4 Conclusions

Robotic autonomy in novel environments is a challenging area of research. Among available locomotion modes, jumping presents a promising mechanism for navigation. This requires a high energetic and power density, as well as the ability to absorb shocks and adapt to landing and taking off on unfavourable, novel terrain.

SEAs allow natural systems to overcome the inherent power limits of their muscles and produce impressive jumping performance. Along with this power modulation, SEAs provide impact absorption and energetic recovery, and this has been demonstrated in numerous robotic systems. The complexity of these actuators, using hard materials and motors, reduces their adaptability and robustness which are crucial for novel terrain navigation.

The Peano-HASEL actuator provides a promising base from which to build a SEA that looks to reduce the complexity of the construction while capturing the beneficial elements of both the soft robotic and SEA paradigms. This is novel as it seems that there is no research currently in literature that applies a fully soft SEA to jumping applications and none using the peano-HASEL.

VSA are also researched in order to reduce the tradeoffs of fixed series elastic elements. These are often yet more complex than the SEAs. The linear actuation of the Peano-HASEL combined with the aponeurosis lateral deformation principle seen in nature allude to a line of research that has not been realised in an actuator to date to create a linear VSA that is fully soft.

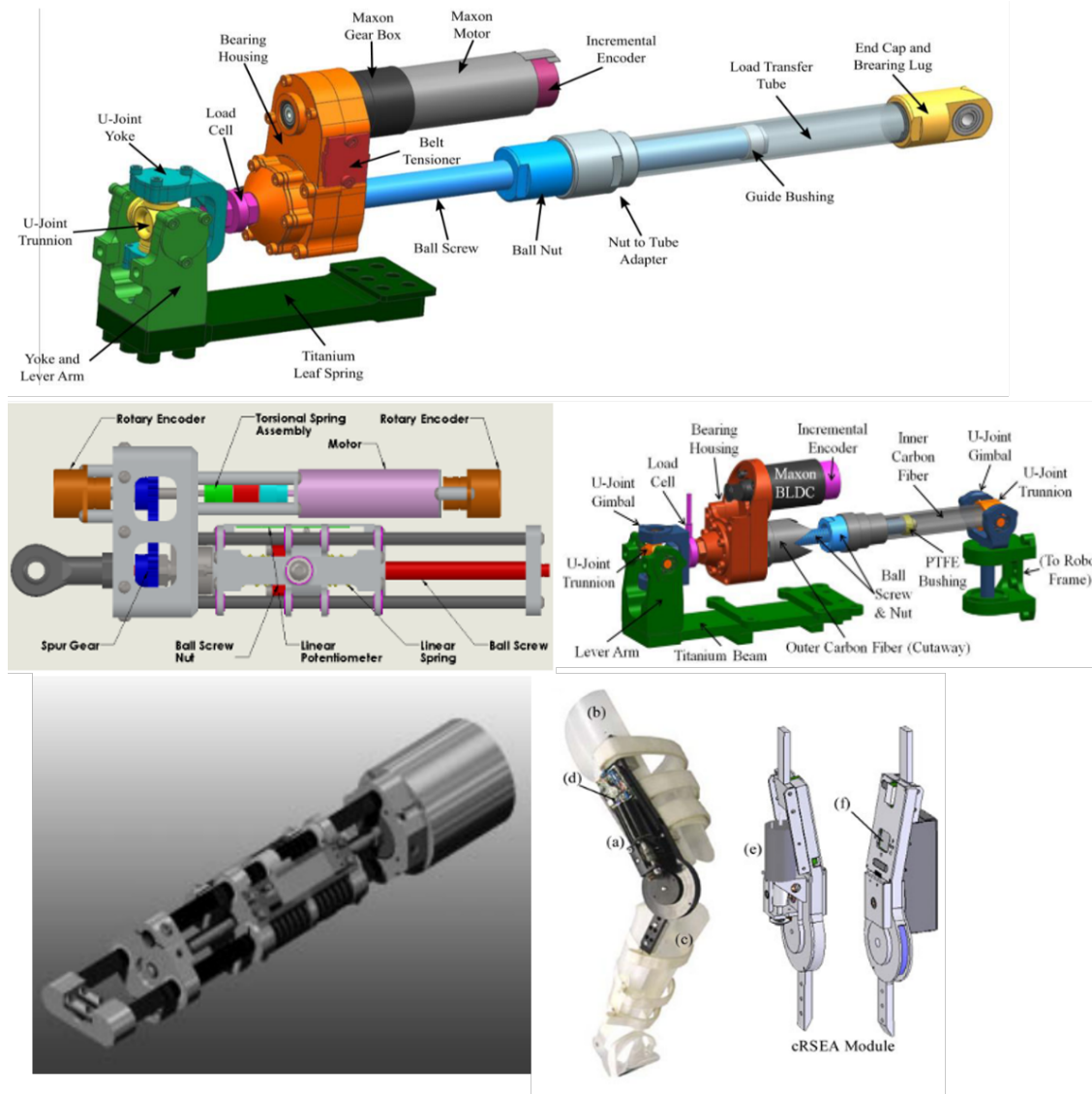


Figure 2.3: Examples of SEAs from literature. Notice the size and holistic complexity of these actuators. Top: MKIV Geared LSEA<sup>[51]</sup>. Middle Left: Variable Stiffness Compliant Actuator<sup>[85]</sup>. Middle Right: Hip SEA for THOR robot<sup>[53]</sup>. Bottom Left: MIT Ballscrew based SEA<sup>[91]</sup>. Bottom Right: Compact Rotary SEA for human assistance<sup>[54]</sup>

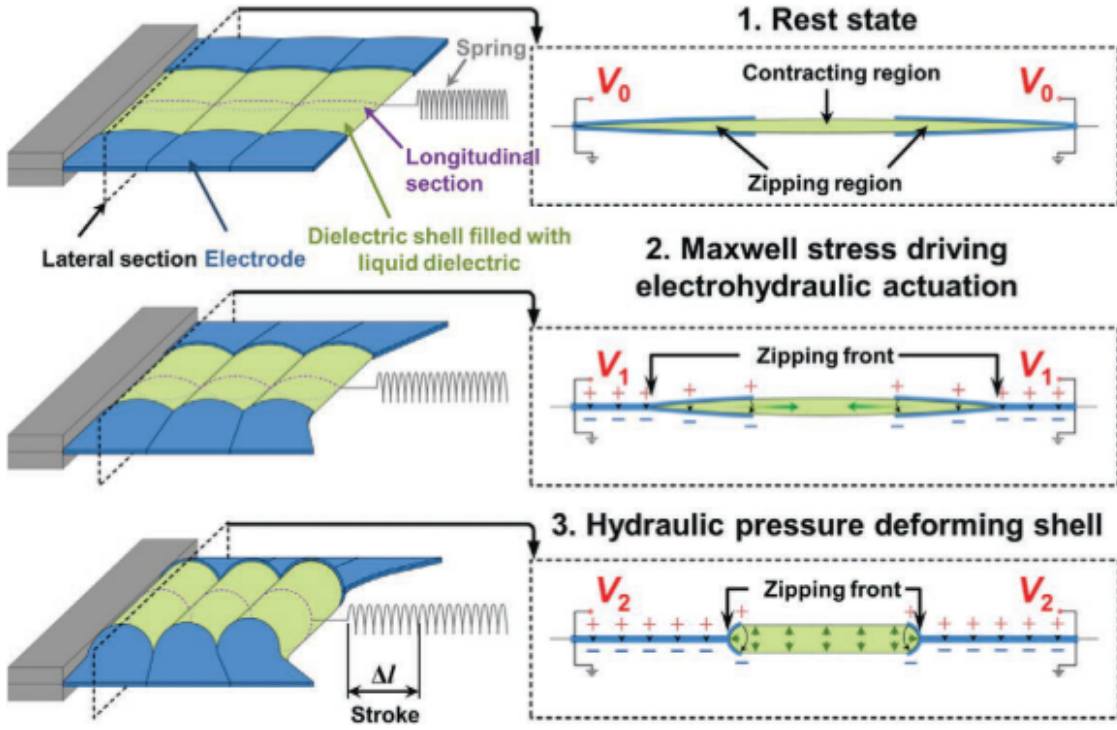


Figure 2.4: Basic operation of a High-Strain Peano-HASEL actuator. The operation of electrode zipping is the same as in all PH actuators, only the placement of the electrode is changed in HS-PH.<sup>[109;95]</sup>

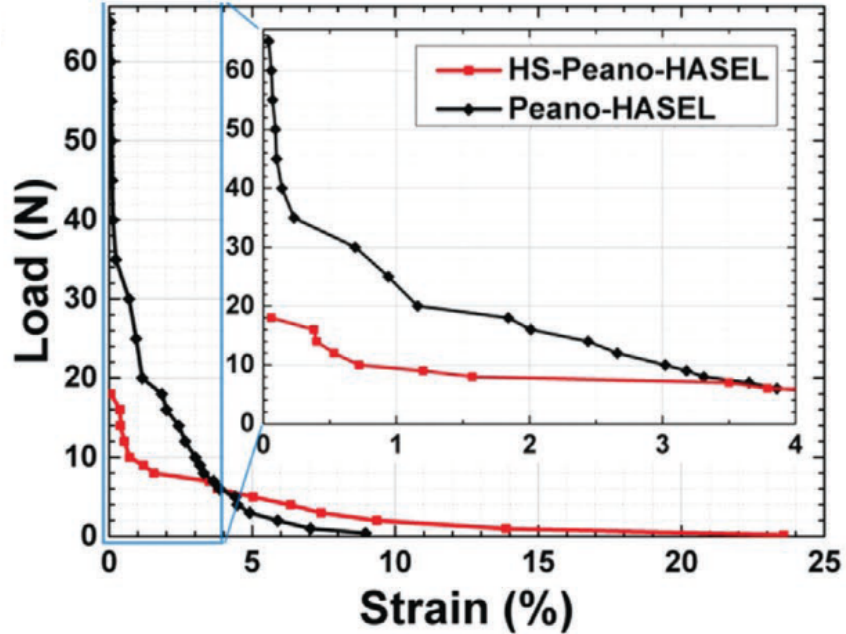


Figure 2.5: Load-Strain characteristics of two types of Peano-HASEL actuator compared. Until 4% strain, standard PH actuators could lift higher loads than their High-Strain counterparts<sup>[109]</sup>.

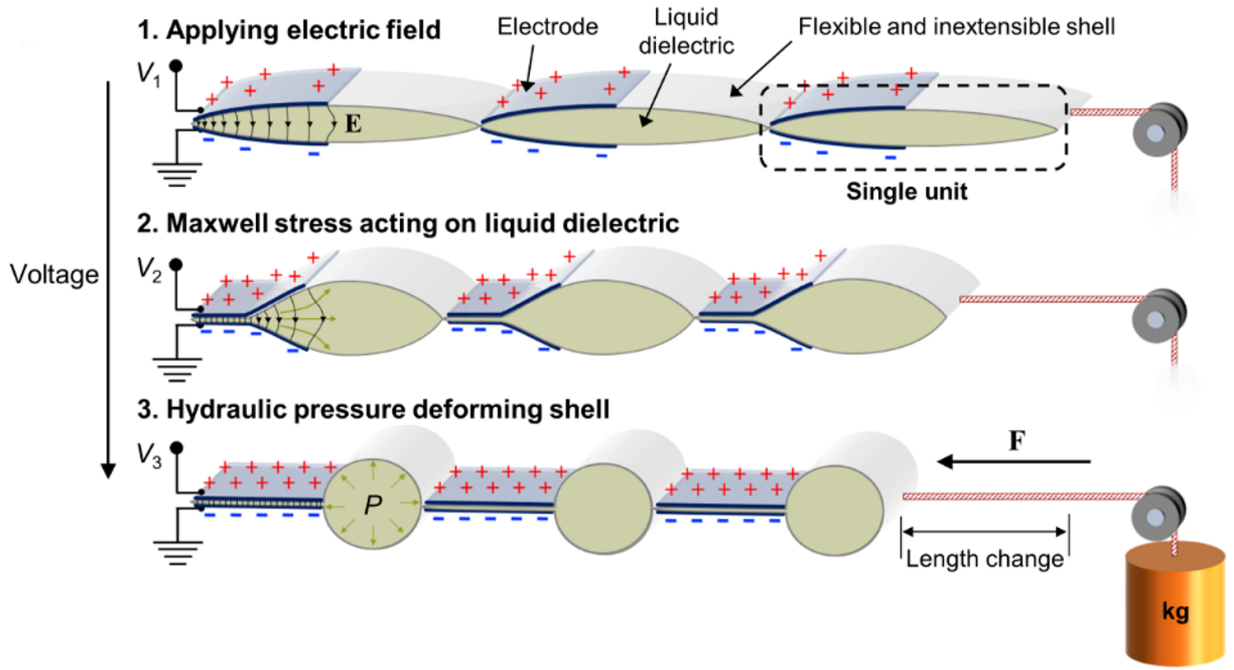


Figure 2.6: Effect of increasing voltage on operational mechanisms of Peano-HASEL actuators from Kellaris et.al(2018)<sup>[50]</sup>

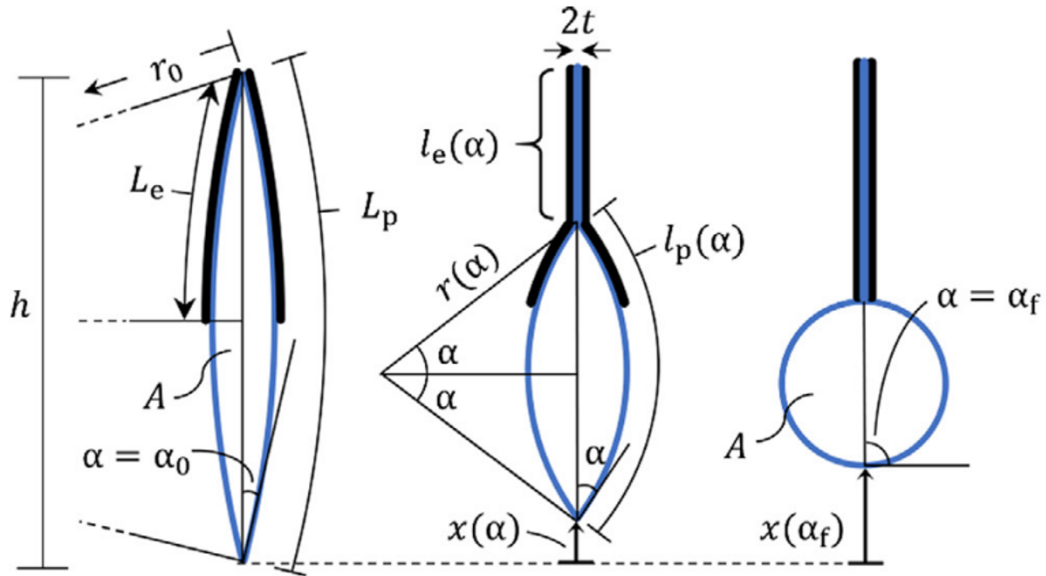
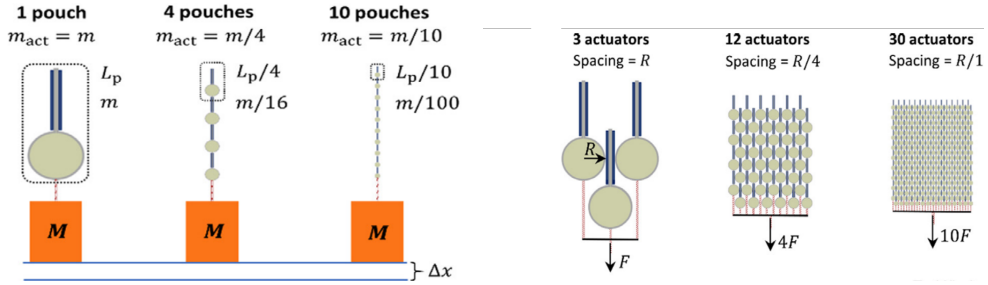


Figure 2.7: Geometry definition for the deformation of the Peano-HASEL actuator from Kellaris et.al(2019)<sup>[49]</sup>



(a) Series Scaling of Peano-HASEL actuators.  
(b) Combined scaling of Peano-HASEL actuators into arrays.

Figure 2.8: Scaling behaviours of the Peano-HASEL actuators, taken from Kellaris et.al (2019)<sup>[49]</sup>.

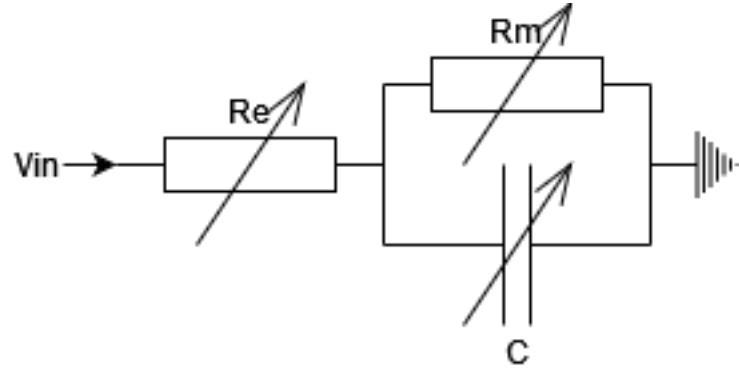


Figure 2.9: Equivalent Circuit of a DEA. As the electric field in non-zipped regions of Peano-HASELs can be neglected, the zipped region behaves like a DEA.

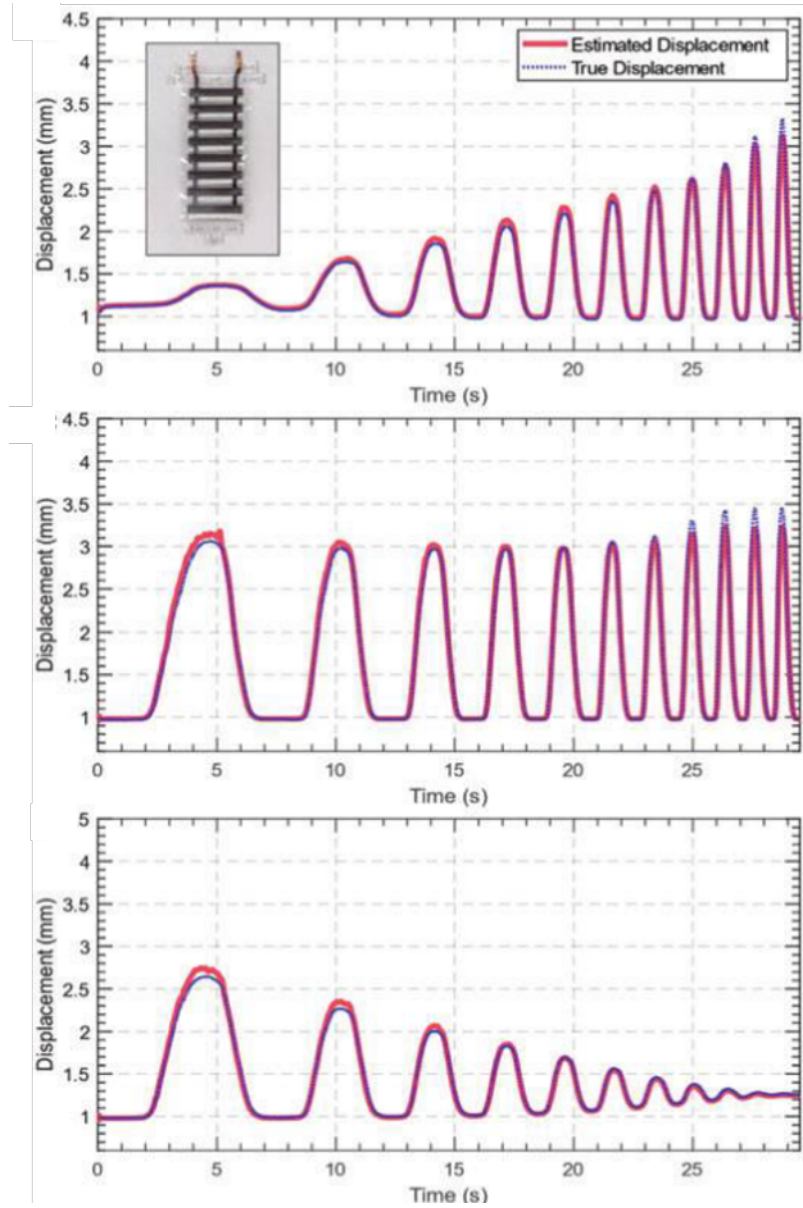


Figure 2.10: Self-sensing of a PH-Fibre with miniturised circuitry by Ly et.al (2020)<sup>[64]</sup>

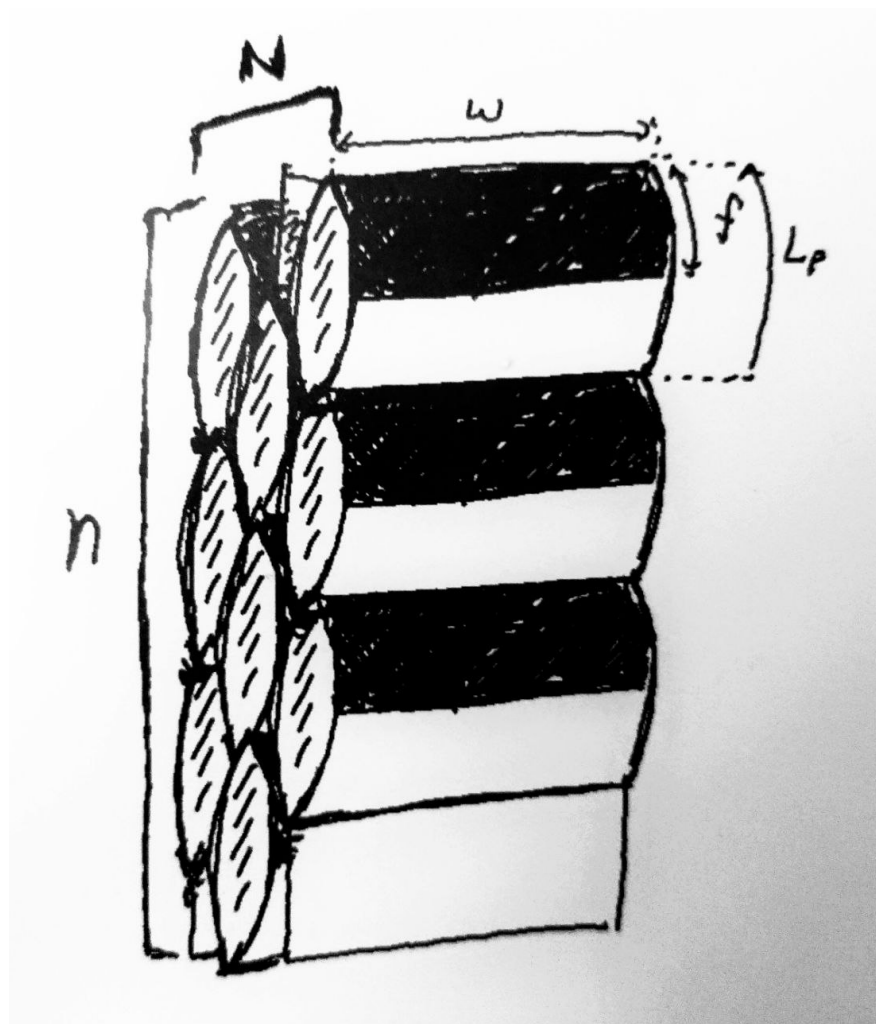


Figure 2.11: Demonstration of PH signature values.

# Chapter 3

## Research Outline

From literature, there appears to be research novelty to develop a soft SEA that can operate on a macro scale for general applications, specifically demonstrating it's applicability to saltatorial locomotion. The Peano-HASEL actuator provides a decent platform to build into this SEA due to it's highly controllable linear contraction, sensing capabilities, energetic density, reasonable force outputs and high frequency response. A PH-SEAmay capture both the beneficial characteristics of series elastic actuation and soft robotic paradigms, while avoiding the complex methods necessary to deform elastic elements using conventional actuators. Moreover, the introduction of a soft series elastic element opens opportunities for variable stiffness responses to be created using pennate Peano-HASELs to laterally deform the SEA, a simple and novel approach to variable stiffness actuation. Desirable series elastic responses may be achievable through both geometric and material variations, optimised through a genetic algorithm: a novel approach to series elastic element optimisation. Further contributions can be made by developing sensing and control methodologies for a Peano-HASEL VSA that allow proprioceptive sensing of both series elastic element and muscle to inform data-driven control.

### 3.1 Aim and Objectives

Aim: Design and characterise a Peano-HASEL VSA and evaluate it's application to jumping locomotion.

- Identify biological principles for saltatorial locomotion and understand state of the art robotics through literature review.
- Establish manufacturing capability for Peano-HASEL actuators and silicone series elastic elements.
- Manufacture a Peano-HASEL SEA and assess it's performance in position accuracy and power modulation tasks against a Peano-HASEL benchmark.
- Optimise the series elastic element using a genetic algorithm for use on the PH-SEA.
- Investigate the expansion of the Peano-HASEL SEA to a variable stiffness paradigm using pennate Peano-HASEL actuators.

- Stretch: Expand sensor coverage of Peano-HASEL VSA to include series elastic element  
Utilise a Long-short term memory (LSTM) machine learning architecture for control.

## Chapter 4

# Development and Evaluation of Peano-HASEL SEAs

### 4.1 Design

To facilitate jumping actuation, it is important that design criteria be evaluated on the PH-VSA. This being novel research on recently developed technology, it is difficult to quantify desired outputs, and this research is more of an investigation and assessment of capability than a production of a applicable prototype. Therefore the designed requirements are more a qualitative desired functionality than quantified goals with respect to particular metrics. This work looks to address jumping specifically for novel terrain and as such should have capability to not only provide the necessary functionality seen in literature for jumping but to do this in unfamiliar and unfavourable terrain. The complexity of any actuator produced should be minimised to increase the energetic density of an actuator and increase it's robustness to failure. Autonomy is crucial to a locomotive robot and as such an actuator should be untethered and controllable.

Table 4.1: PH-VSA design specification for jumping robot applications. Many of these are also general specifications.

PH-Variable Stiffness Actuator Design Specification		
Requirement	Description	Importance
Supply of Jump Impulse	The energy required for the jump must be achievable by the actuators in antagonation with gravity.	10
Actuator Force Modulation	Actuators should enact force modulation to more efficiently jump with greater efficacy.	9
Repeated Action	The actuator components must be able to perform for a number of cycles without self-inflicted deleterious effects on performance, controlability or stability.	10

Versatility	Actuators should have a wide range of states available for control to facilitate adaptive jumping in unknown terrains.	8
Actuator Control	Control of the actuators must be directly controllable by a computational controller.	10
Proprioception	The computational controller must be able to infer the state of the actuator to act accordingly.	10
Actuation Stimulus	The actuation stimulus must be controllable, efficient and renewable.	10
Actuation Stimulus	The actuation stimulus must be controllable, efficient and renewable to allow for repeatable and accurate locomotion.	10
Impact Protection	Landing impacts should have minimal deleterious effect on the actuator to reduce failure from locomotion fatigue.	10
Mass Specific Actuator Energy/Power/-Force	The specific metrics of the actuator should be maximised to contribute towards optimisation of jumping performance.	7
Actuator Strain	The strains produced by the actuators should be sufficient to deform an SEE or rotate any standard joint, desirably without additional components.	7
Component Energy Transmission Efficiency	Components and their interactions should be as efficient as possible within the actuator energy flow, to increase mission longevity before the need for recharge a power supply.	8
Control Efficiency	Control Stimulus should be minimised for a given performance, so as not to use unnecessary power.	8
Weight	Component weights should be minimal. This allows payload cost reduction, feasibility of deployment as well as improving jump performance and reducing power expenditure.	9
Force Modulation	Actuator force output can be moderated temporally by a series elastic element to allow for transient release of stored energy. This greatly enhances jumping performance in biological jumpers and the facility should be available in the PH-VSSEA.	10
Stiffness Tuning	The stiffness the elastic element should be tuned to dynamically and controllably optimise force modulation, positional control and impact absorption.	9

Actuation Predictability	The action of an PH-VSSEA as a passive and active entity should be understood, reliable, repeatable and controllable. Any deviation from this should be within tolerable limits.	10
Control Autonomy	No operator input should be involved in low/mid-level control operations as signalling times in space applications are limited by the speed of light and data bandwidth.	10

#### 4.1.1 Outline

## 4.2 Peano-HASEL Manufacturing

Peano-HASEL actuators are presented in literature as low cost and easy to manufacture<sup>[? ]</sup> Kellaris2018,Rothemund2019. Minimal starting investment in bespoke equipment is needed and materials used are readily available commercially. This is an enticing set of claims, potentially allowing rapid design iteration, mass production and accessibility to competent robotics platforms for poorer communities and institutions were they could find use in medicine, prostheses, agriculture and search rescue. While these claims are true, there is an amount of experience, gained through iterative practice, required in order to consistently create actuators. This chapter will detail the current manufacturing process in this project as well as the tried, ineffective methods and materials on the path to create this methodology. 3 main components are required for a Peano-HASEL:

- A heatsealable, inextensible and flexible polymer film to create the shell
- Flexible and conductive electrodes applicable to polymer films that can handle high voltages
- A dielectric oil

In this work, the Peano-HASEL actuator is a muscle (in the nomenclature of this work) with signature [5 | 7 | 80 | 20 | 0.6. According to the analytical model, this allows for a maximum displacement of

### 4.2.1 Film and Heatsealing

Biaxially Orientated Polypropylene with a heat seal treatment was provided by Innova Films (Propafilm FFX30) for this project with  $30\mu m$  thickness. The heat sealing side is essential for creating a bind between the two sheets. Several different versions of BOPP and Mylar sheeting were tried but the seals were not efficient to hold under stressing by hand, and would predictably fail under actuation pressures. According to the static force equation a thinner film will increase actuator force output and  $20\mu m$  sheets are being sourced. Unfortunately the Propafilm line is no longer manufactured, so a suitable alternative must be specified. It has recently been shown that BOPP Peano-HASELs exhibit interesting dielectric properties in minute actuation time scales<sup>[98]</sup>. The BOPP actuators will see displacement decay over time and with the removal of actuation voltage initially relax before re-actuating. Clearly this is an undesirable property in application



Figure 4.1: A complete Peano-HASEL Fibre with signature [1 | 7 | 80 | 20 | 0.6]

and one that is mitigated or even rendered negligible with a change in film material. Mylar film was sourced as an alternative film material, however there were difficulties in producing effective seals and electrodes. The actuation time scales currently involved in this research are on the order of seconds but will see rapid voltage fluctuations, so it remains unknown whether this phenomena will factor into experimental considerations. Further replacement films made of Mylar or Polyester materials are currently being identified regardless. The charge can also be extracted by applying a inverted voltage to the actuator which could potentially alleviate this effect if prominent.

Initially, while awaiting completion of alternative and more consistent methods of sealing, a soldering iron was used to create actuator shells by hand. Using a ruler as a guide, this primitive method while effective was limited in the available geometries. It was challenging to create curves and small features that reduce the impact of edge effects during actuation<sup>[48;97]</sup>. Moreover, the heat of the soldering iron along with inconsistent application times meant many actuators would occasionally have small holes melted into them, not discovered until filled with oil and pressure applied. Seal integrity was also variable being directly related to heat application time over each area.

Heatseals are also cited in literature as a main contributor to actuator failure: failing under actuation pressure or decreasing the resistance to dielectric breakdown of the polymer. It is therefore an important factor in actuator efficacy and requires due attention.

A method used in literature is sealing via heatpress<sup>[50]</sup>. This is effective in consistently applying accurate geometry seals. However, it becomes challenging to iterate geometries. Heatpress methodologies require a die from which the geometry is imposed onto the film. These are constructed often of brass and in literature are welded using epoxy to the heatpress. This makes them static and removes the favourable attribute of rapid prototyping granted by the actuation's geometric coupling, constraining possible actuator configurations and respective performance metrics considerably. A modular die was designed and constructed to attempt to alleviate this by allowing divisions using components that could be added to a die screwed to the plate. This was micromachined from brass and as a result tolerances were not tight enough to allow application. Moreover, the issue of geometric constraint was not removed and merely mitigated. This methodology was eventually abandoned in favour of the current methodology using a 3 axis CNC.

More recent literature favours seal creation using cnc machines<sup>[70;48;95;96]</sup>. These often manifest as modified 3D printers, with a simple modification swapping the hollow extruder head for a solid counterpart. Recent work has also shown that seals can be created by extruding 1 layer of filament onto the film<sup>[30]</sup>. While creating effective seals, reducing the risk of scratching and requiring no modification to a 3D printer or additional components, this is somewhat wasteful as the filament is then discarded. The advantage of all of these techniques is that any conceivable geometry can be written into a GCODE file and manufactured quickly with CAD software. This realises the rapid prototyping and mass manufacture potential of the Peano-HASEL. In addition, with adequately secured film, seals are accurate and consistent, even with small features. For this research, a large 3 axis was modified to include a heating element and a modified 3d printer extruder. A custom labview program converts gcode into labview commands that interface with an FPGA on a MyRIO platform. Initially, DXF files of seal paths were converted to GCODE using specialist software. However, needing an opening for oil filling meant tool paths were not closed and this often confused these softwares, creating tool paths that were inefficient or simply erroneous. To solve this, a custom matlab script was written to generate GCODE files.

To create a seal, the sealing tip is heated to 200°C. While above the temperature suggested by the film manufacturer, experiments with seal quality showed superior results with BOPP covered by Kapton sheets at a higher temperature than lower temperatures applied directly to the BOPP surface. This is because the kapton sheets distribute the heat over a larger area, generating a

secure seal while also deforming the BOPP in the sealed regions less, which becomes important for consistent electrode application.

Two BOPP sheets are rubbed together to induce static, which aids the seals consistency, and then placed below a Kapton sheet. The stack is then placed onto a rubber heat resistant mat which allows consistent force application due to its compliance. Seals are created quickly and highly repeatable.

The seal geometry is an important factor in performance. Increasing the weight of the sealed line increases the creating a more effective the binding of film sheets and a stronger seal. This can be achieved by using a large diameter heating element and by exerting more force onto the film. However, a thicker seal reduces the effective geometry of the actuator by moving the boundary into the actuators geometry. The size of the seal is also inconsistent and can be affected by minor material creasing induced by the force exerted by the heating element. Securing the film without interfering with the path of the heating element greatly mitigates this. Force applied must be balanced when creating an effective seal. Too much force can drag the heating element through the BOPP, creating large defects. Excessive force also contributes to the out of plane shape of the seal, a factor which can drastically affect electrode application.

The introduction of small indentations to the edges of the uncovered areas of the actuator reduce edge effects and facilitate higher consistency in strain across the actuators width. This is a simple addition with CNC. It is important to factor in the size of this feature relative to the width of the seal to alleviate overlapping of seals which reduce the effectiveness of this modification.

#### 4.2.2 Applying Electrodes

With respect to electrodes, this research uses Graphink CMC 2: a flexible electrode ink made of graphene embedded in a water-based medium. The geometry used for electrodes is shown in figure. Literature for Peano-HASELs mainly uses carbon inks and paints, with the original Peano-HASEL paper using hydrogels. Carbon inks/paints provide a solution that is relatively cheap and available commercially, applicable via screen printing or hand brushing. However, problems arise that see cracking in addition due to inconsistency in electrode thickness and shape that can lead to performance deficits or outright actuator failure and destruction. It is suspected that with large scale screen printing equipment these problems may be reduced but it is not practical to produce these in the quantity needed with the amount of design variation that arises from prototyping and iterative methodology construction. Hydrogels are a valid solution but with the complexity of manufacture and equipment needs, similar issues with manufacturing and prototyping arise in line with the carbon inks. The Graphink is the most expensive component of this actuator, costing However, this cost comes with a degree of reliability in manufacture and application of an actuator that is necessary for the constrained time of the project and the aims of the research.

Electrode creation proved to be a challenging component of the manufacturing process. In initial prototype actuators, carbon ink was hand applied by brush, using masking tape to constrain the applied area. Again, this manual method of application removed the ability to create fine or more complex geometric features, such as slight curves, than simple rectangles with any consistency. This is particularly detrimental with sharp points on the electrodes. The high voltages involved in actuation create large electric fields. Sharp points in the electrode greatly increase the electric field density as field lines must be perpendicular to the surface, and thus diverge at large angles around sharp points. This increases the probability of breakdown events in the high density region. Moreover, the hand painted electrodes were highly inconsistent in paint density. Actuator deformation could be impaired if the electrodes are too thick and many failures in manufacturing came of electrode cracking where they were excessively thick (Figure. 4.2c. These primitive electrodes

did however facilitate initial energising experiments.

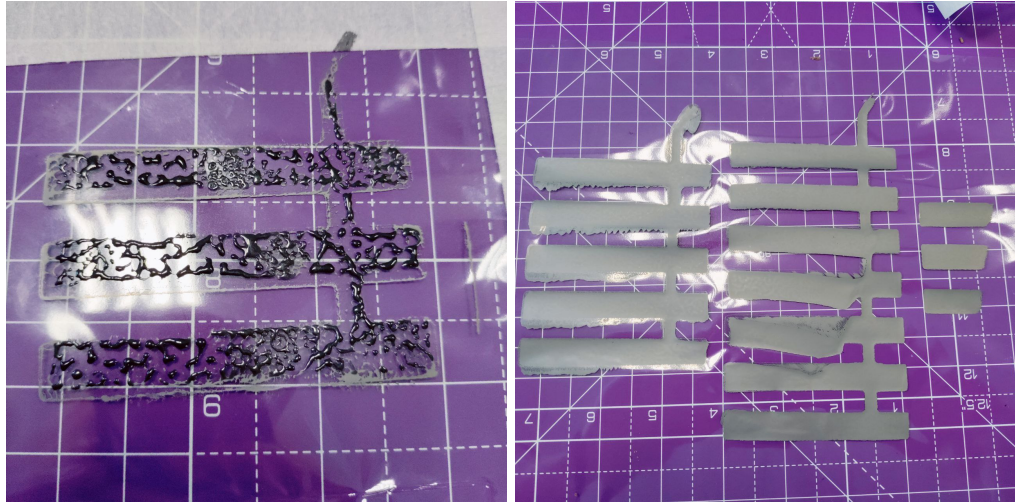
To allow more consistent application with finer geometric features, screen printing was attempted using the same carbon paint. This method has been used in literature to apparent effect, but little success was observed in this work<sup>[97;48;70?]</sup>. Problems first arose with the paint thickness, making it difficult to force through the mesh of the screen. Moreover, it was difficult to secure the sealed actuator against the screen so that the electrode could be applied accurately. This resulted in off centre electrodes and even total failures. Once an electrode is applied erroneously the actuator cannot be salvaged. Removal of the screen also caused issues with paint being pulled up from the sheets plane, either roughing the surface or removing it entirely, which results from the rapid increase in viscosity induced by the paint drying. Also, removal of the screen could cause in plane motion that smears the paint, causing sharp and holed points in the actuator or completely . Smears also cover parts of the actuators surface that are undesirable. If the paint is left to dry with the screen on, the screen sticks to the electrode and roughing and paint removal are again observed.

In an attempt to alleviate this, the paint was thinned using water. This introduces an additional consideration inherent to the BOPP film used. As the film is used in food packaging, it is possibly coated on the side without heat seal treatment in a hydrophobic layer, or carries this property inherently. This means that water introduced to the paint will bead on the actuator surface and not dry in a consistent layer (Figure.4.2a. This problem was also present with the Graphene ink and was subsequently solved by using white spirit to degrade the BOPPs outer layers and then inducing static on the surface via friction to increase binding. Thinker ink can also be airbrushed by running white spirit through the airbrush before using undiluted ink, increasing adhesion and coverage consistency.

The current methodology used with the Graphink is airbrushing. This was inspired by a recent publication<sup>[30]</sup> The problem of beading initially persisted, but the discovery of the effective pre-treatment allowed the ink to adhere well. Airbrushing in addition produces a thin electrode which is flexible and rarely cracks. Using a mask laser cut from plywood or 3D printed, clamped with the actuator film sandwiched between it and a back plate, geometry with fine features can be accurately applied. In addition, paint smearing failure occurrences are low as the ink dries quickly and there is no compression of the ink between film and applicator. Occasionally, errors in aligning the mask can skew the position and orientation of an electrode, and the opaque mask can make it difficult to mitigate this. A acrylic, clear mask and backing plate was cut to solve this. Aligning the electrodes on opposite sides of the film is challenging for similar reasons.

As mentioned in the sealing section above, it was realised that the out of plane height of the seal affected ink adhesion when crossing the seals. This created difficult to identify gaps in the electrodes where they cross onto another actuator or creating the steams for high voltage supply connection. These were identified by holding the actuator up to a light source and assessing gaps in coverage. The ink falls down this slight incline of the seal if it was too prominent. This was solved using the Kapton sheet methodology described and tuning the z-offset to apply optimal pressure to the film during sealing. Sparsely painted regions could also be identified by a similar method and usually occurred around edges. These could create edge effects in the electric fields, increasing the current density at these sites and increasing the probability of breakdown. Application of multiple coats can solve this, but it becomes difficult to maintain consistent electrode thickness. Application of multiple coats of ink mitigates this problem. However, defects become difficult to identify when applying the second electrode as the first blocks the light.

In summary, manual application of electrodes is currently challenging and riddled with caveats, but achievable. As these actuators are in their infancy, this is understood to be a teething process, and if production is scaled these issues can likely be mitigated. Moreover the issues of beading are



(a) Beading of electrode ink when applied to the film without pre treatment (b) Paint Smearing due to removal of screenprinting screen.



(c) Cracking of hand painted carbon paint electrodes.

mainly a product of the intended application of sourceable material in this work, and do not reflect the plethora of potential materials available. Careful selection of film material or even bespoke production would be a welcome.

#### 4.2.3 Oil and Filling

The dielectric oil used in this research is FR3 Cargill Transformer oil. This oil is environmentally safe and benign while exhibiting desired properties (Table 4.2).

Parameter	Value
Dielectric Breakdown Strength	$\geq 30\text{kV}$
Viscosity	$111.5\text{mm}^2\text{s}^{-1}$ at $20^\circ\text{C}$
Density	$0.92\text{gcm}^{-3}$ at $20^\circ\text{C}$

Table 4.2: Selected FR3 oil properties

To fill the pouches with oil. A filling port is left open during heatsealing. This facilitates filling via a syringe. The shape of this port appears important to ease of manufacturing. Too wide a port will make it difficult to consistently seal, which can induce ripples in the film that may affect actuation efficacy. Using a wider port also produced significant losses of oil as the oil would creep up the needle as it was removed. This is particularly troublesome when electrodes are already applied as the oil can rapidly deprecate the quality of the electrode, even causing cracking and flaking. Attempts were made to apply electrodes after the filling process but these were often of poor quality as it became difficult to reliably airbrush through the mask due to the pressure build up caused by clamping the mask to the actuator. As a result final electrode quality and alignment was poor.

The oil when compressed by the electrodes culminates in a static pressure state which exhibits a load on the film. This load is also experienced by the heat seals used to bind the film sheets together. This tearing force moves to push the sheets apart. Therefore any seals must be able to withstand the hydraulic pressure. Testing of prototypes indicates the minor probability of this failure mode in machined seals, often down to an ineffective seal being established in manufacturing, inferred by manipulating remaining seals by hand. However, seals made by hand using a soldering iron, to close the filling port, are less consistent and structural weaknesses can be created by ineffective sealing or burning through of the film due to under and over exposure to the heating element.

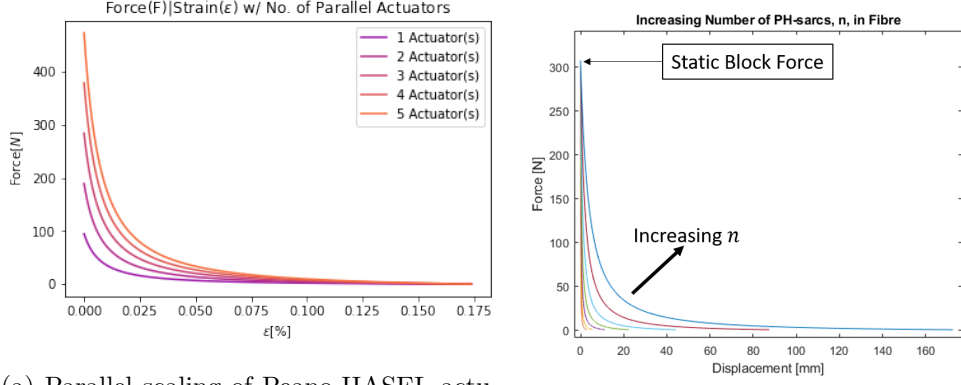
In order to mitigate the potential failure risk in these seals, the location of the port is positioned towards the top corner of the actuators side. This placement puts the potentially ineffective seal outside of the film regions that experience significant pressure, mitigating the load experienced by the soldered seal. This also allows for more effective removal of bubbles as each sarcomere in an actuator is filled independently, reducing the amount of air potentially trapped by the oil when compared to methods which fill from the top of the entire fibre. Initially the PH-Fibre was filled from the top, the oil passing through each Sarcomere but this proved time consuming for the removal of air bubbles. The placement also ensures that the fill port does not interfere with the small defects introduced in the seal which reduce edge effects. The port is made relatively long and thin to reduce oil loss during filling and is wide enough to allow a needle to pass through.

## 4.3 Numerical Series Elastic Element Investigations

A number of simple investigations were carried out on the Peano-HASEL model in Kellaris et.al (2019) and simple Hookean spring elements. These initial results were used mainly for gaining understanding of actuators. A python model was constructed to allow initial probing of the SEA mechanics. This model is exceptionally limited in only providing dynamics in the deformation domain (as discussed). Therefore, investigations of the SEA were limited as such.

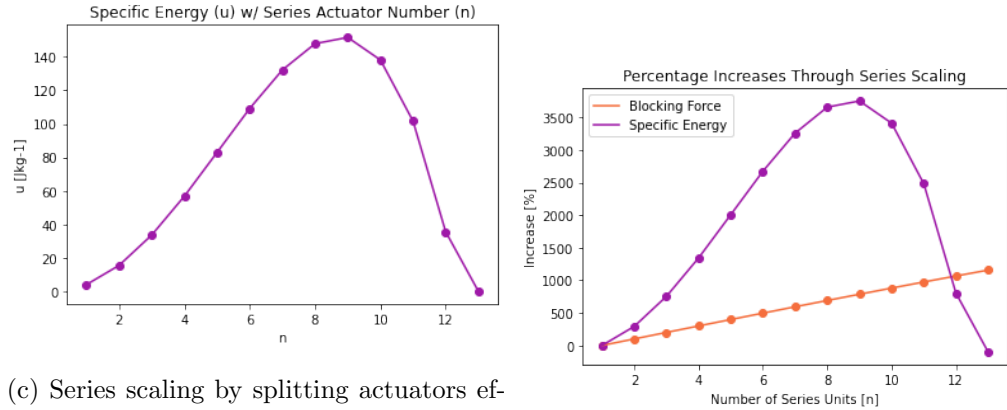
### 4.3.1 Peano-HASEL Scaling and Expansions

As mentioned in section 2.3.3, scaling of PH actuators can be achieved through a number of methods. Figure 4.3 demonstrates the effects of the parallel and series scaling behaviours on affected PH outputs. If one was to take multiple instances of an actuator in series, without inciting the splitting scaling methodology, overall actuator strain would increase due to the linear superposition of the individual strains. However the effect on force output here is non-trivial. As the actuators are coupled in a free hanging system, an actuator above another must also displace the additional mass of the actuator below it. Furthermore, there is no gain to maximum blocking force. The



(a) Parallel scaling of Peano-HASEL actuator fibres. The tail end of the curve is minimally impacted by the scaling while the blocking force increases and the bulge moves outwards. (BOPP -  $V = 10\text{kV}$  -  $[1 \rightarrow 5 | 1 | 120 | 20 | 0.6]$ )

(b) Non-Splitting series scaling. The blocking force is unaffected while the tail increases in length and the bulge moves outwards. (BOPP -  $V = 10\text{kV}$  -  $[1 | 1 \rightarrow 7 | 120 | 20 | 0.6]$ )



(c) Series scaling by splitting actuators effects specific energy. Gains are seen until bending stiffness begins to dominate the force behaviour. (BOPP -  $V = 10\text{kV}$  -  $[1 | 1 | 120 | 20 | 0.6]$ )

(d) Percentage gains in series split scaling (BOPP -  $V = 10\text{kV}$  -  $[1 | 1 | 120 | 20 | 0.6]$ )

Figure 4.3: Example Scaling behaviours of PH-Actuators

additional mass is dominated by the fluid and can be approximated by:

$$m_{add} = \frac{\rho_f gw}{2} L_p^2 \left( \frac{\alpha_0 - \sin(\alpha_0)\cos(\alpha_0)}{\alpha_0^2} \right)$$

which is an extension of Kellaris et al. (Equation 1)<sup>[49]</sup> with  $\rho_{hof}$  as the density of the liquid dielectric.

While the effect of splitting a single actuator into multiple series actuators is presented in Kellaris et.al's (2019) work, there is no discussion of the combination in series of multiple actuators. For  $n$

actuators in series, the maximum actuator displacement for a given load  $P$  is estimated by:

$$x(P) = \sum_{i=1}^n x_i(P + m_{add}) \quad (4.1)$$

Where  $x_i$  is a function of load  $P$  and the additional mass the mass contribution of the liquid dielectric of the  $i - 1$  actuators below the  $i$ th actuator, the major mass contributor. An example of this behaviour is given in figure.4.3b.

### 4.3.2 Hookean Spring Studies

Investigations including Hookean springs showed that a linear spring suffers inherent limitations when in combination with a Peano-HASEL actuator. The nature of the Force/Strain relationship is shaped by the  $\frac{\cos(\alpha)}{1-\cos(\alpha)}$  term. When the actuator deforms, its force output monotonically decreases relative to this characterising curve. As a springs force output increases as a function of strain, it is natural for the two to be plotted together. As the force of the spring's tension is acting as the load on the Peano-HASEL, there is a point in which the spring's tensile forces overcome the actuators force output. This sees the actuator blocked as a result: i.e. there exists a maximum extension for a given spring (Fig. 4.5). This maximum extension is capped by the actuator's geometry, but deviates below this with spring stiffness variation. From discussions of the biomimetic SEAs, a key metric in transient force generation is the amount of the actuator's energy that is stored inside the series elastic element. When the actuator is blocked, this also coincides to the maximum stored energy. Taking the integral under the two stress/strain curves gives the energy stored in the spring (assuming full elastic recoil) and 100% energy transfer efficiency). Using a linear, Hookean spring, the maximum possible energy efficiency of the SEE is 40% of the actuators energy, but because the SEE is overtly stiff, this blocks the actuator earlier and produces less energy. This behaviour is shown in figure.4.4, with the optimal point marked. given from sweep of stiffness. If the transient force modulation mechanism is to be effective in facilitating jumping locomotion, this value should be increased if possible.

## Evaluation of BOPP-based Series Elastic Elements

When making use of a specific, linear actuator, if the intention is to expand this into an SEA, it would be desirable to have a methodology to define a SEE best suited to an actuator's application. An SEA without variable impedance capability requires this functionality be carefully considered before implementation into a design. There is a trade-off of function with the impedance of an SEE. Favourable attributes of both compliant and stiff elements exist and the reciprocal relationship between them mandates compromise. A more compliant SEE may be beneficial for tasks such as impact absorption; allowing passive energy recovery; as well as providing protection to the actuator. However, a stiffer SEE allows for more accurate and efficacious force transmission between actuator and environmental impedance, as well as reliable, predictable control. With what may be called a *fixed impedance* SEA (in contrast to *variable impedance*), these trade-offs must be considered as persistent and as such, care must be taken in the choosing of an appropriate impedance. As discussed in section Power modulation is a large factor of consideration for many locomotive systems, as it promotes high impulse movements and a greater takeoff velocity in systems both artificial and natural. This implies the need for high energy storage and therefore a more compliant SEE. However, when developing an SEE for power modulation, considerations of the holistic system

### Stiffness Influence on Efficiency and SEE Energy

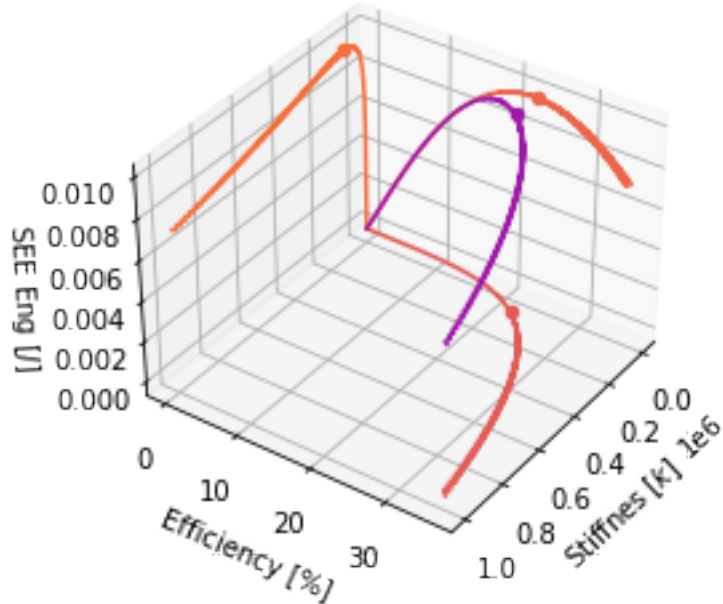


Figure 4.4: Behaviour of a linear SEE with increasing stiffness. The optimal value of stored energy arises at 23.42% actuator efficiency and a stiffness of  $k = 119 \times 10^3 \text{Nm}^{-1}$ . Actuated by a PH-Sarcomere (BOPP -  $V = 10\text{kV}$  - [1 | 1 | 120 | 20 | 0.6])

within which the SEE is embedded are needed. Olberding et. al developed a model for SEAs which showed that although a  $5000\text{Nm}^{-1}$  system stored the most energy in a mechanical advantage latch system, a stiffer  $8000\text{Nm}^{-1}$  maximised the energy of motion<sup>[?]</sup>. This is contrary to intuition that a more compliant SEE stores (And therefore releases) more energy when only the SEE is considered and manifests as a result of the wider system's strain and force limits. In this work, attempts are made to determine a general methodology to tune PH-SEA stiffness and evaluations are made on a 1-dof system. As such, the optimal stiffness demonstrated in this work is not generally applicable, but a proof of the geometric variation methodology to achieve a general desired stiffness. The optimal stiffness is problem specific. The tendon of natural systems is highly complex, with functionality and complementary properties beyond simply power-modulation. Natural tendons are multi-scale hierarchical systems involving nuanced interactions between many biological components. Macroscopically, tendons throughout their length vary material properties, geometrically twist and vary cross-section. The biomimetic principle used in this work is that the tendon's geometry is a contributor to function, specifically it's stress/strain response. Twists, convergent divergent forms and tapering all occur in the natural tendon. It is important to note however that studies have found suggestions that material gradients and differences are more prominent in the tendon dynamics than geometric variation. Nonetheless, the principle of geometric variation remains useful in a fixed material situation. Equation (4.2) gives the relationship between Stiffness (A component of impedance)  $k$  [ $\text{Nm}^{-1}$ ] and geometry for Hookean elastic elements:

$$k = \frac{EA}{L} \quad (4.2)$$

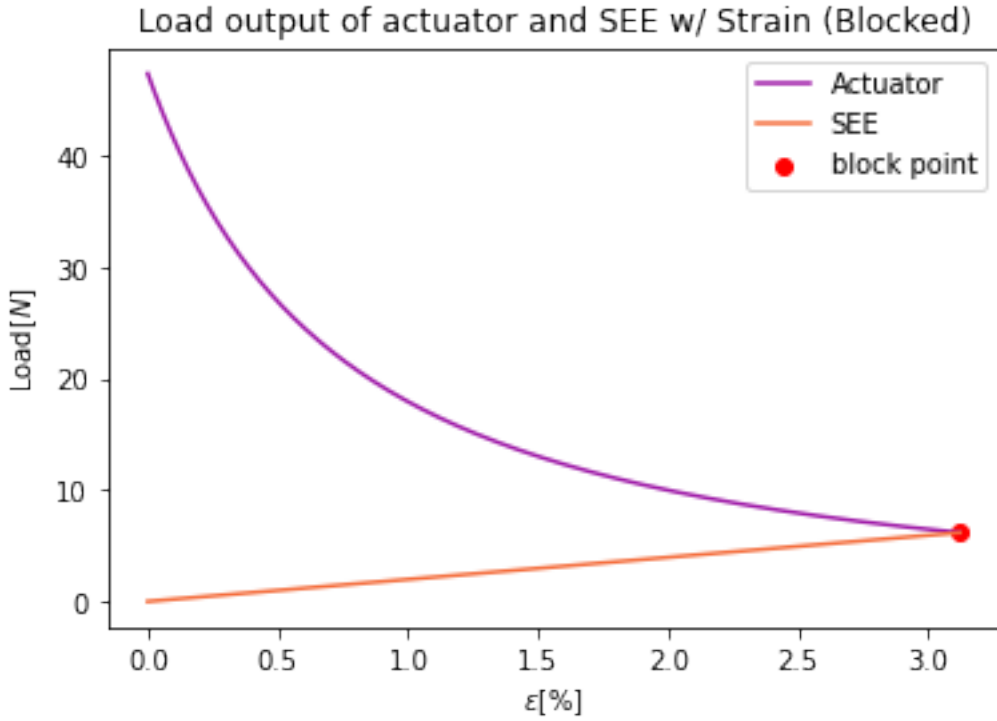


Figure 4.5: Demonstration of a  $10000\text{Nm}^{-1}$  SEE blocking a single PH-Sarcomere (BOPP -  $V = 10\text{kV} - [1 | 1 | 120 | 20 | 0.6]$ ). Note the considerable area below the actuator curve not enclosed by the SEE curve, demonstrating the inefficiency of the linear SEE.

Variation in cross sectional area  $A$  [ $\text{m}^2$ ] and Length  $L$  [m] affect the stiffness (and therefore impedance) of an elastic element. Imagining a series of small elements of non-negligible length  $dx$  and mass in series along a length  $x$ :

$$k(x) = \frac{EA(x)}{dx} \quad (4.3)$$

Implying that if  $A(x)$  is not a constant function, the stiffness response of the element would vary throughout the length and generate unique stiffness behaviour. The size of the area term when compared to  $E$  is small, on the order of  $10^{-6}$ . It is likely therefore a more achievable material variation throughout the tendon would affect stiffness far more than area variation. However, a halving of area would half the stiffness in such a region, all other terms held constant. To create a Soft-SEA, the Peano-HASEL shell material could be extended and cut into an SEE. Given the above equation, through geometric alterations (Figure 4.6), the stiffness is hypothesised to be tuneable. What remains unknown is the magnitude of this effect. It will also be important to maintain elastic deformation in the SEE. Any hysteresis from plastic deformation is undesirable from both control and lifetime perspectives.

## Modelling and Simulation

To provide an initial insight, modelling of BOPP tendons was undertaken and simulation studies were carried out in order to rapidly vary the geometry and assess the validity of geometry as a

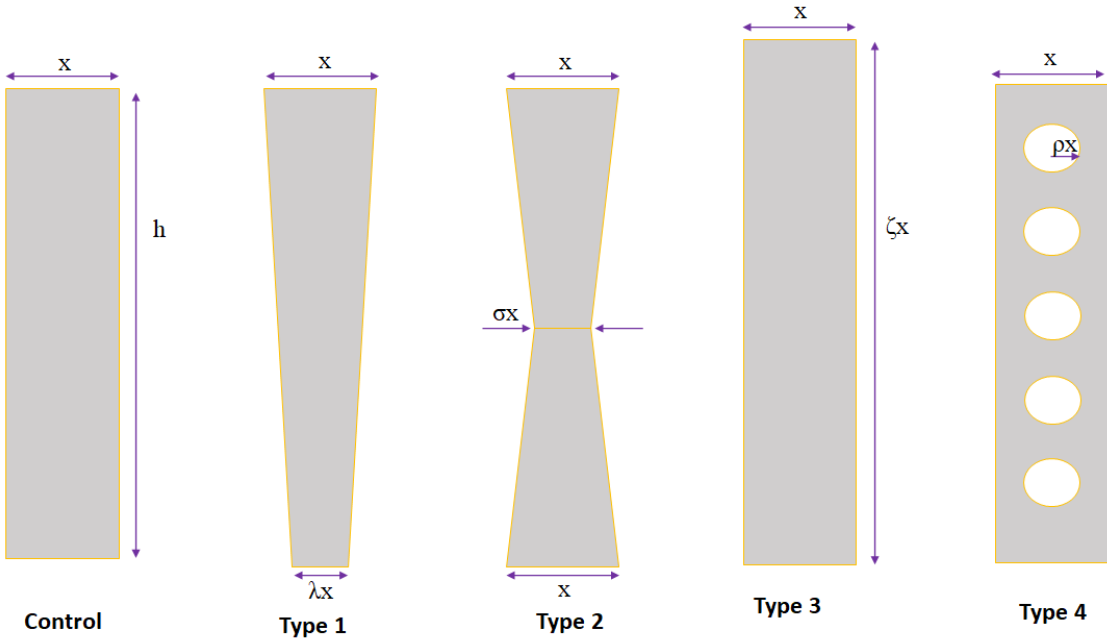


Figure 4.6: The parametrisation of geometry for the four types of geometry in this study, defined by the four ratio parameters: Type 1 -  $\lambda$ ; Type 2 -  $\sigma$ ; Type 3 -  $\zeta$ ; Type 4 -  $\rho$

stiffness tuning mechanism. Four geometric variation types are studied to give an insight into the relationship between different SEE geometries and stiffness:

- TYPE 1 - Tapers
- TYPE 2 - Convergent/Divergent
- TYPE 3 - Varying Length
- TYPE 4 - Holed Elements

These four types were chosen to provide similar but unique topographic changes to geometry, as with type 1 and 2 having convergent and divergent sides, as well as different topographies with type 3 and 4. All these geometries are easily controlled by a single parameter and the geometry of each element was parameterised as in figure 4.6. Parameters are defined by their ratios to the loaded edge,  $x$ , which has a constant size in these investigations. A parameter is dimensionless, promoting generality in the stiffness-parameter relationships obtained. Control geometry was set as a 20mm x 100mm x 0.042mm strip in proportion to predicted PH-SEA test system size. All geometries are simple modifications to BOPP SEEs that can be made consistently with a laser cutter.

Simulated geometries were modeled as 2D Isotropic Elastic, static investigations using Ansys Mechanical. 2D is a valid assumption as the thickness of the film ( $42\mu\text{m}$ ) is negligible relative to other dimensions. All geometries were loaded with a linearly ramped  $0 \rightarrow 100\text{N}$  tensile load, with a step size of 2N, from their loaded edge ( $x$ ) and fixed at the other end of their length. Total displacement was recorded at each step. This load mimics the approximate blocking force of a single Peano-HASEL and corresponds to a 10kg mass load. In practice, the displacements reached by the SEE in simulation would not occur: the Peano-HASEL is limited in strain output by its

$A_{Con}/A_\lambda$	$\lambda$	$\sigma$	$\rho$	$\zeta$
<b>1.000</b>	1.000	1.000	0.000	5.000
<b>0.950</b>	0.900	0.900	0.126	4.750
<b>0.900</b>	0.800	0.800	0.178	4.500
<b>0.850</b>	0.700	0.700	0.219	4.250
<b>0.800</b>	0.600	0.600	0.252	4.000
<b>0.750</b>	0.500	0.500	0.282	3.750
<b>0.700</b>	0.400	0.400	0.309	3.500
<b>0.650</b>	0.300	0.300	0.334	3.250
<b>0.600</b>	0.200	0.200	0.357	3.000
<b>0.550</b>	0.100	0.100	0.378	2.750
<b>0.500</b>	0.000	0.000	0.399	2.500

Table 4.3: Matrix of geometric parameters that maintain the ratio between the area of the control geometry,  $A_{Con}$ , and the tapered Type 1 area , $A_\lambda$ , in a BOPP SEE. As SEE thickness is constant, this ratio is equivalent to the ratio of material volume and, assuming a homogeneous material, this allows distinction between the mechanism of stiffness variation: whether it is related to topography or material volume. The topographic mechanism would see equal stiffness variation for all geometries which share a row. The columns for  $\lambda$  and  $\sigma$  are equivalent, and the two types share a stiffness variation curve (Figure.4.8). The first row defines the control geometry and the corresponding geometric parameters that create it.

geometry<sup>[49]</sup>. However, the simulation's scope does not contain the interaction of actuator and SEE, instead focusing on how stiffness changes with geometry. Also omitted is the coupling between the actuator's maximum achievable deflection and the stiffness response of an SEE, therefore it is highly unlikely that the maximum deflection observed in simulations will be met in application.

All simulations were subjected to mesh convergence using Ansys automesh refinement. BOPP was modelled to be loaded in the non-machined direction, corresponding to a 2.5GPa Youngs modulus with an assumed Poisson's ratio of 0.33.

## Experiments

Experimental loading for a selection of geometries was undertaken using an Instron Z010 mechanical testing apparatus. Pneumatic clamps held BOPP samples in place and each was loaded until failure. Each geometry in the selection was tested with 6 samples. These tests were used assess the validity of the geometric stiffness variation hypothesis and the simulation accuracy. BOPP is anisotropic and a polymer, so the linear isotropic elastic model naturally invokes inaccuracies. Geometries were laser cut from two sheets of  $21\mu m$  Innova Films Propafilm FFX21using a Trotec Speedy 300 with 50% power and 10% speed.These tests generated force/displacement curves for each SEE that could be compared to an analytical model of a Peano-HASEL to assess it's efficiency in storing

the actuators energy, as well as the magnitude of this energy. This was achieved by comparing the areas under both force/displacement curves of the SEE and Peano-HASEL prior to the SEE blocking the Peano-HASEL. Areas were computed using numerical integration. To understand the applicability of the BOPP-SEEs to it's operational paradigm, cyclic loading tests were undertaken to identify the magnitude of the hysteresis involved in loading and unloading the SEE. These tests were performed on geometries again manufactured with laser cutting from the same material. Failure or senescence of a BOPP-SEE in application would cascade into actuator failure, as the pouch of the Peano-HASEL is being extended into the SEE. Therefore, should the SEE become unpredictable or unusable due to irreversible deformation, it cannot be replaced, and the entire actuator becomes useless. Furthermore, changing the physics of actuation through the progression of material properties with cyclic loading would have a significant detriment to the accuracy of any robotic controller, eminently undesirable for uncoupled and autonomous navigation.

## BOPP Tendons: Results

### Modelling and Simulation

For Type 1 - Tapered geometry, the simulations suggest that there is a relationship between the geometry of the BOPP SEE and it's stiffness. Figure 4.7a shows that as  $\lambda$  decreases (creating a larger taper), the displacement experienced by the SEE increases, demonstrating a variation in stiffness. Figure 4.8 reports a weak non-linear relationship between the taper ratio and the stiffness. Type 2 geometries also show the same parameter-stiffness relationship as Type 1. Normalisation of stiffness relationships about the control geometry provided insights into the potentially scale-invariant relative stiffness changes topography alterations can facilitate. Here,  $\sigma > 1$  Type 2 SEEs produce higher stiffness than the control. Figure 4.8 shows that the two are approximately equivalent. Where  $\lambda = \sigma$ , the stiffness is functionally identical with only slight deviation, likely caused by simulation induced numerical errors. This result suggested that the topography of an element may be irrelevant in stiffness variation and it is possible that what is being observed is a relationship more directly attributable to the amount of material present in a SEE.

In order to investigate this further, conversion functions from  $\lambda$  to the other ratio parameters were defined such that the area  $A$  is conserved:  $A_\lambda = A_\zeta = A_\sigma = A_\rho$ .

Parameter	Conversion Equation
$\sigma$	1:1
$\rho$	$\sqrt{\frac{k}{2n\pi x}}(1 - \lambda)$
$\zeta$	$\frac{h}{x}(1 - \frac{\lambda}{2})$

Table 4.4: Area preserving conversions between  $\lambda$  and other ratio parameters.  $n$  quantifies the number of circles evenly distributed along a Type 4 length, set  $n = 5$ .

This conversion maintains  $A$  and the material volume (given constant thickness), while changing the element topography. If the stiffness is topography independent within the simulation assumptions, the stiffness variation with  $\rho$  and  $\zeta$  should be equivalent to any other parameter. The simulation results did not support the material volume hypothesis. Variations in  $\rho$  exhibited a looser displacement distribution, while  $\zeta$  dependant variations were much tighter (Figures.4.8). This corresponded to differences in the stiffness relationships for these parameters despite the maintained

material volume, demonstrated in figure 3. For  $\rho \rightarrow 0$ , a monotonically decreasing relationship was observed and comparable, with an offset to variations in  $\lambda$  and  $\sigma$ . Variation in  $\zeta$  diverged greatly from the behaviour of other parameters, showing large increases in stiffness as  $\zeta \rightarrow 0$ .

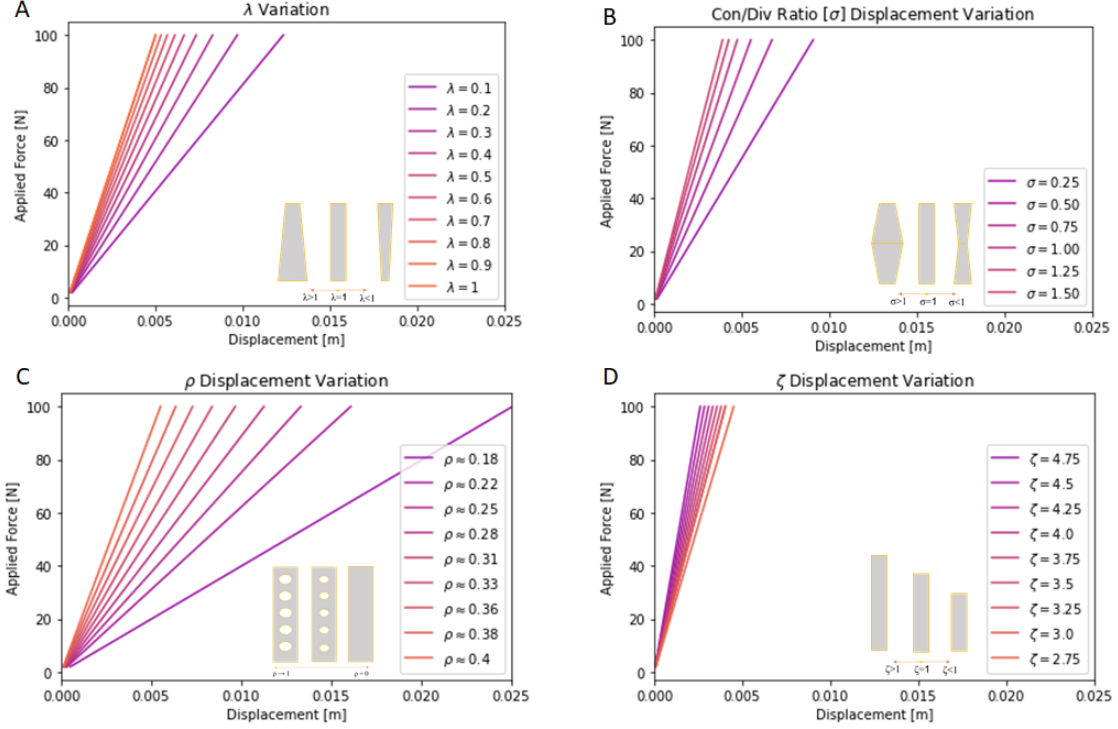


Figure 4.7: Geometric Parameter sweeps for (a)  $\lambda$ , (b)  $\sigma$ , (c)  $\rho$  (for  $n = 5$ ) and (d)  $\zeta$ . Both (c) and (d) are swept in values defined by the area maintaining conversion factors in table 5.1.

## Experimental

All geometries tested demonstrated two distinct, nonlinear deformation regimes (Figure ??). The first was a low displacement region characterised by steep gradients, which transitioned into a shallower high displacement region before failure. Often, one of the BOPP layers would fail before the other. This behaviour was likely caused by manufacturing defects. When heated under laser cutting, BOPP films experience out of plane distortions due to wrinkling. As the sheets are separate during manufacture and as such free to move out of plane, this behaviour may have created small defects in the edges of the SEE where the laser cut the deformed film. These defects could generate stress concentrations which may have lead to premature failure. Mechanical testing results demonstrated that control of both the geometry and topography of an SEE creates consistent and respectively different changes in stress-strain responses. This is in agreement with hypothesis. However, the stress-strain behaviour of the elements was considerably different from that shown in simulation. The changes in geometry did demonstrate variation in the stiffness in the near-linear region of the stress-strain response, but the major alteration was when the material would transition into a regime of reduced toughness and it's behaviour in this regime. Furthermore, mechanical testing data suggests that the behaviour of varying a geometric parameter has different effects on the stress-strain behaviour, dependant on the parameter. Variations in  $\zeta$  (affecting length) appear

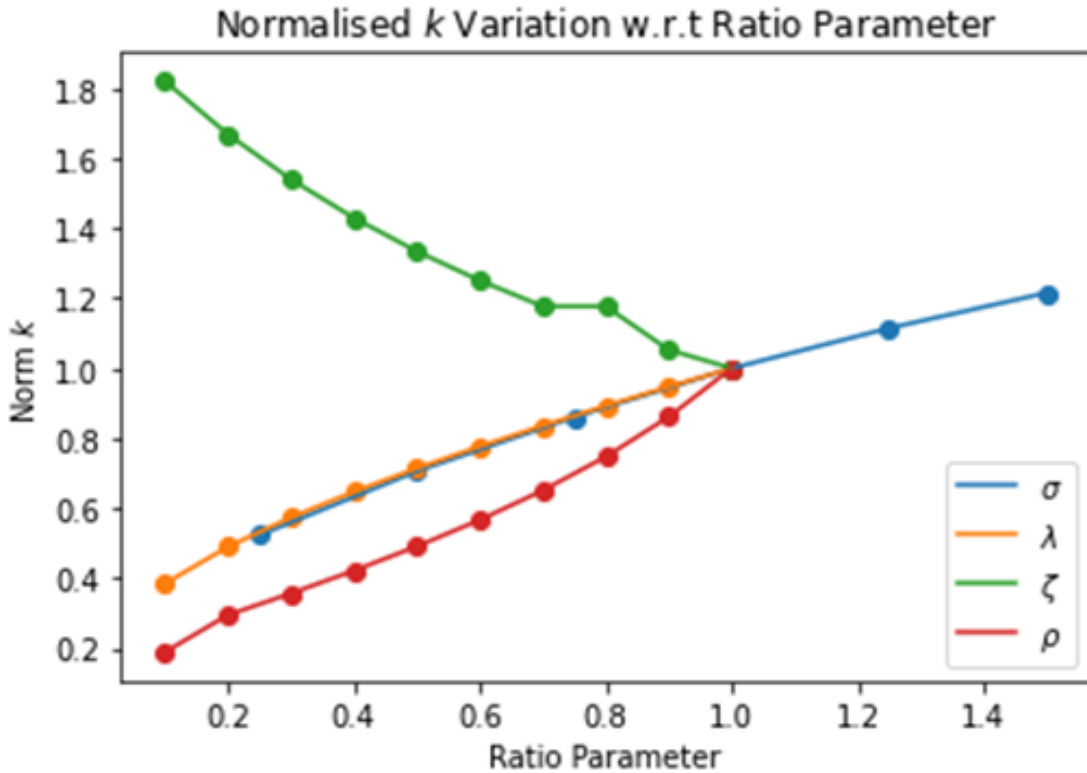


Figure 4.8: Normalised with respect to the control geometry: variations in  $k$  for respective area maintaining  $\lambda$  equivalents (defined by table 5.1).

to create minimal deviation in the first deformation regime. Larger values of  $\zeta$  transition quicker into the secondary regime, however the data suggests that this relationship is non-linear as  $\zeta = 3.5$  and  $\zeta = 4$  show very close agreement on when they exit the first deformation regime and their behaviour prior. Variations in  $\lambda$  (affecting taper) showed different behaviour to  $\zeta$ . The first regime was significantly altered with  $\lambda$  variation and the distinction between the two deformation regimes is less pronounced with decreasing  $\lambda$  values. The two samples of  $\rho$  (affecting punched hole radii), while showing behaviour deviating from their equivalent  $\lambda$  and  $\zeta$  counterparts, showed minimal variation between  $\rho$  values other than in the transition region between regimes. An indication of the efficacy of the BOPP-SEEs can be obtained by finding the stress-strain curve's intercept point with an analytical Peano-HASEL model's force-displacement behaviour. Peano-HASELs are subject to a blocking force which sees the actuator's deformation stunted as the electro-hydraulic forces are equaled by the load, which in the case of an SEE occurs when the stress-strain curve intersects the Peano-HASELs and produces an analytical estimation of the SEEs energy storage efficiency relative to the energy produced by the Peano-HASEL. From Fig.4.10, a large amount of potential Peano-HASEL energy is not captured by the SEE population's curves. An effective SEE when viewed from a purely power modulation standpoint should look to maximise elastically stored energy across it's effective stroke and this is quantified in figure 4.11 along with the magnitude of energy stored. Plotting a Peano-HASEL force-tip displacement curve (Single Pouch, 120mm/20mm [width/pouch length] with 60% electrode coverage actuated at 10KV) together with the BOPP-SEE's mechanical test results indicate geometric perturbations make a low impact to

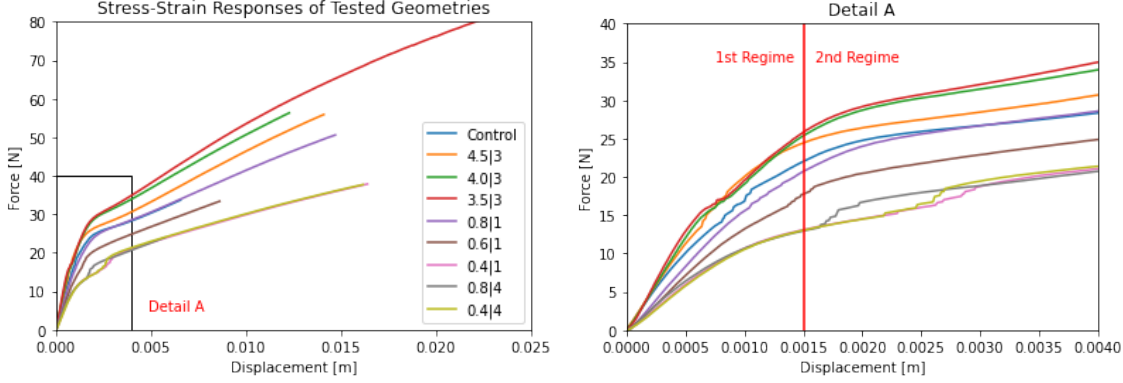


Figure 4.9: Sample averaged mechanical testing results for geometries. The first legend numbers display the equivalent  $\lambda$  value and the later indicates geometry type ( $\equiv \lambda |$  Type). Detail A shows the transition region between stress-strain regimes. Experimental noise and error is more prominent and visible in this region on this scale.

the stress-strain response on the Peano-HASEL's scale. This is possibly due to the inextensibility of the BOPP, which is supported by the tight grouping in the first deformation regime when compared to the second, where the effects of geometric modification have greater impact. The first regime demonstrates higher stiffness and the rapid decline of force output in the Peano-HASEL with stroke causes the majority of SEEs to block the actuators before the emergence of the second deformation regime. This may however be beneficial, as it is suspected the transition region alludes to the introduction of significant hysteresis.

Comparing the BOPP SEEs to a Peano-HASEL numerical model found that there was a  $\approx 3.5J$  change in stored energy between the minimum ( $\approx 24J$ ) and maximum ( $\approx 27.5J$ ) of the tested geometries, corresponding to a  $\approx 2.5\%$  change in energy storage efficiency ( $10.5 \rightarrow 12.5\%$ ). It is unclear if this energy would be elastically recovered. The BOPP's inextensible nature suggests not.

### 4.3.3 Discussion

Investigating geometric variation as a mechanism for tuneable stiffness alongside a validation of an SEE formed from a simple extension of the BOPP Peano-HASEL elucidates the need for elastic materials that deform in predictable ways. The modelling and simulation results suggested stiffness was geometrically tuneable. Ratio parameters were defined which altered the topography of a series elastic element and were referenced to the loaded edge of the BOPP SEE, providing generality to the results obtained. However, only one control geometry was investigated, so this generality remains to be verified. Ratio parameters were swept and the geometries loaded in simulation to reveal the effect on stiffness. Simulated SEEs with tapering and convergent/divergent topographies showed comparable stiffness variation during their parameter sweeps while exhibiting differing topography. This suggested that it was material volume, not the topography, giving rise to stiffness variation. In order to test this, area maintaining conversion equations were derived. The maintenance of area (with constant thickness) maintains material volume, but the change in ratio parameter alters the topographical regime. Results from these investigations demonstrated it was indeed topography generating the stiffness variation and different ratio parameters demonstrated

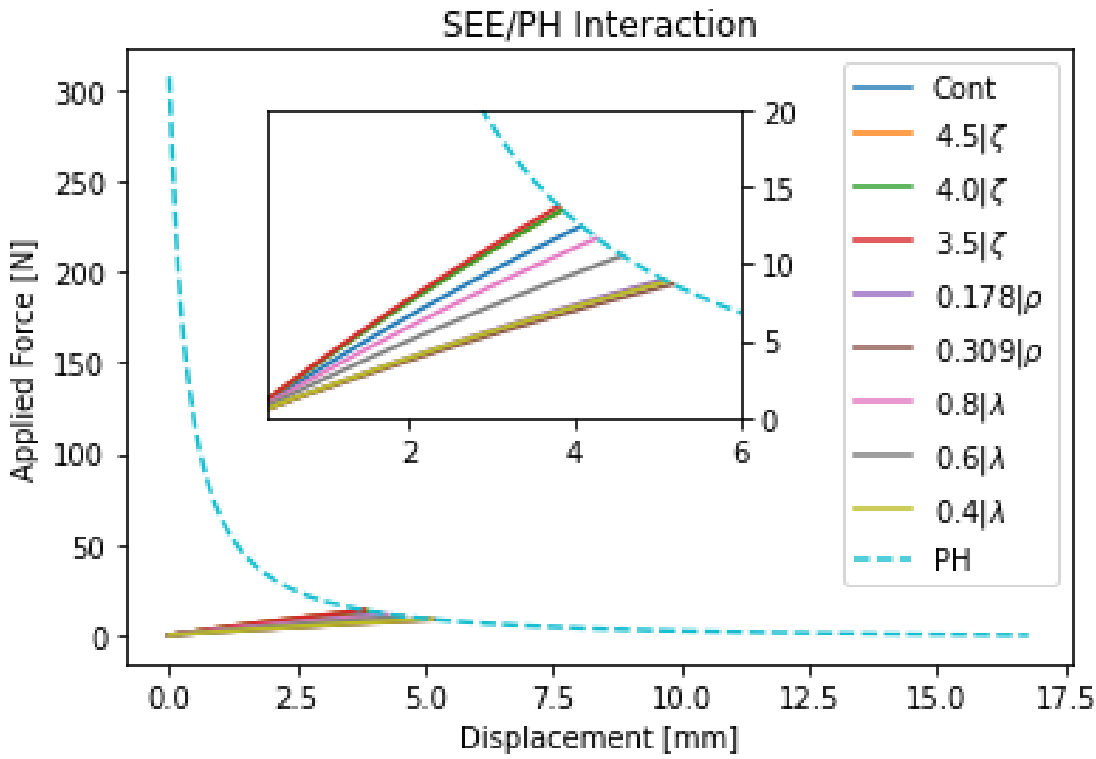


Figure 4.10: The interaction of Peano-HASEL Force-Stroke behaviour with the mechanical testing data suggests poor energy storage efficiency and minimal useful stiffness tuning potential.

considerably different stiffness variability. Experimental mechanical testing was used to validate a selection of geometries. These tests were conducted until failure and the results compared to an analytical Peano-HASEL model. This allowed indications of energy storage magnitude and efficiency when SEEs operate coupled to the Peano-HASEL. Results showed that at maximum \_\_\_\_\_. As the BOPP is inextensible, the ability to recover this work is reduced by the inelasticity. Mechanical testing results demonstrated two distinct regions. It is important to determine the magnitude of hysteresis in the deformation of an SEE from a standpoint of energy recovery efficiency as well as a control standpoint. In effectively 2D deformation regimes, geometric variation appears to affect the response of an SEE, however the effect is small. The effect in 3D regimes however remains unknown.

#### 4.3.4 Conclusions

The BOPP's inextensibility, critical to the actuation mechanism of the Pean-HASEL, makes it inadequate as a mechanical energy storage. While geometric changes did affect the stiffness and therefore the energy storage capability of an SEE, experimental results suggest the impact is small. However this may be due to the inextensibility of BOPP and the effectively 2D geometry.

Silicone SEEs are indeed possible with appropriate couplings and the ability to mold silicone into different shapes allows the propagation of the geometric variation principle to three dimensions. Silicone's highly elastic nature presents the possibility of hysteresis immunity, imperative for effective control and locomotion. Moreover, silicone allows for an effective continua of possible

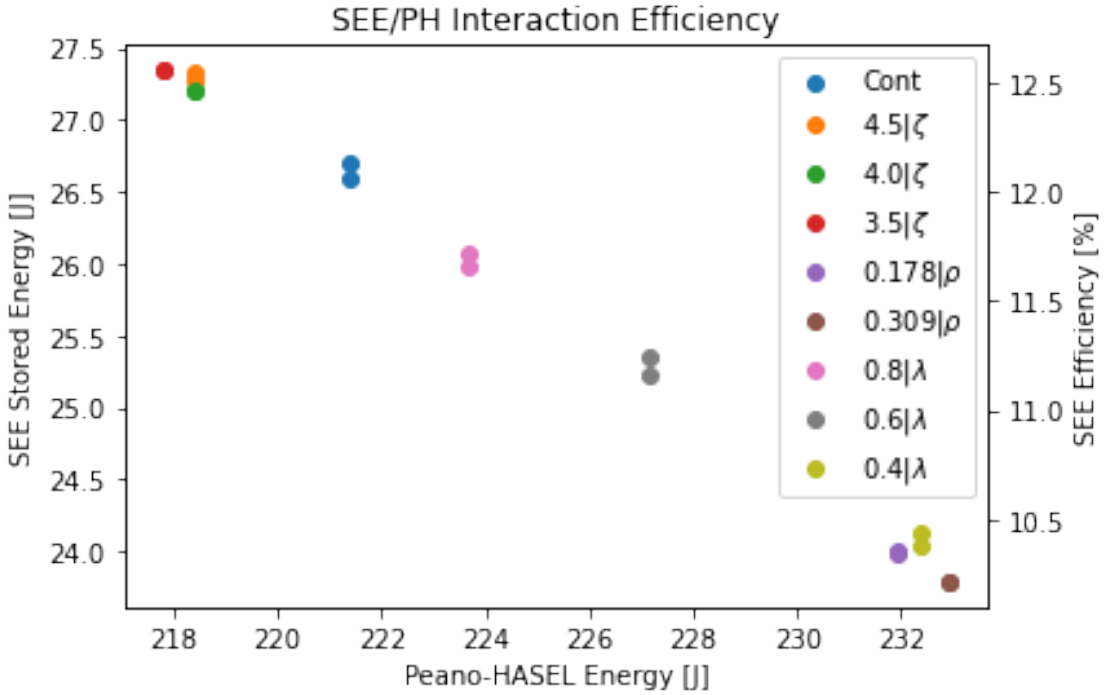


Figure 4.11: BOPP SEE energy storage metrics compared to the available Peano-HASEL energy output. The  $\zeta$  and  $\rho$  parameters show strong grouping while  $\lambda$  tapering reduces effectiveness. While gains can be made through  $\zeta$  variation, the strong grouping indicates a plateau in these gains. Notably, facilitating further development of Peano-HASEL output energy before blocking did not increase the energetic effectiveness of an SEE.

elastic responses by mixing ratios of shore hardness, opening up the possible SEE design space. Multi-material SEEs are also possible as experiments have shown that two silicones can easily be molded together. The ability to couple soft materials with varying characteristics currently appears, in the HASEL actuator case, to be a necessity. This is not unlike nature, where tendon makeup is different to the muscle and facilitates different functionality<sup>[86]</sup>. These characteristics promote silicones validity as an SEE material over BOPP.

Future work will investigate the static and transient response of a silicone SEE when coupled to a Peano-HASEL, specifically looking at: Displacement and force limits; positional accuracy and its variation with load; settle times and velocity response; as well as the possibility of variable stiffness through pennate actuation. Bar the variable stiffness, these investigations can be carried out within the next months. Variable stiffness will require thought to the alignment of multiple actuator fibres as well as modified coupling. It is possible this coupling can again be 3D printed or molded from a high stiffness (50/60 shore) silicone.

## 4.4 Manufacturing, Development and Evaluation of Silicone Series Elastic Elements

Silicone is a highly elastic material which can be molded to a desired geometry easily and with good accuracy. For these reasons, it is an attractive material to use as a SEE. However many issues arise including the manufacturing methodology, coupling to Peano-HASELs, design methodology and response to force stimuli statically and transiently. Progress towards addressing these considerations will be discussed in this section and the following chapter.

### 4.4.1 Silicone Molding

In this work, silicone is molded in 3D printed molds. These are made by subtraction of a desired geometry from a mold block in CAD software and splitting the mold to allow release of the cured SEE. The molds are printed in two parts and joined together by screws before pouring the silicone.

However, a different approach is required to accurately produce the cases discussed in future sections where it is desired to create silicone SEEs with multiple shore hardness silicones. This requires multiple curing stages and access to multiple sections of an SEEs geometry. To achieve this, modular molds were designed. Originally, these were made to lay flat, leaving the top surface of the silicone exposed. However, from prototyping tests, it seems that the different silicones would not create effective bonds in this scheme. Alternative testing revealed that under the presence of gravity, the silicones do indeed form effective bonds, so it is hypothesised that the hydrostatic pressure of the uncured silicone produced by gravity produces this effective interface. To transfer this idea to the modular molds, tower molds were designed that stack modules on top of one another.

However, tests with tower molding also demonstrated silicone tear off along the interface, suggesting the binding is attributed to another factor in the manufacturing. Future work will investigate the impact of curing times between the pouring of different silicones on the interface. Currently the silicone has been left to fully cure. A low curing time is thought to provide a stronger interface but may lead to mixing of the different silicones, while a longer cure time may reduce mixing but create a weaker interface.

## 4.5 SEE-PH Coupling

To reliably transmit force into the SEE, it is necessary to have a consistent and reliable interface between the actuator and the SEE. This connection must be able to interface with both silicone and BOPP and remain attached with minimal hysteresis throughout multiple actuation cycles and to the extremes of displacement and force outputs. Fully cured silicone cannot be glued to the BOPP directly as the low energy compensating adhesives used on the BOPP cannot bind to silicone. Allowing the BOPP to sit within the silicone during the curing process does not bind the two either, even with the addition of small cavities in the BOPP to allow silicone to cure within them. This fails rapidly with tears in the BOPP.

### 4.5.1 PLA Embedded "Root" Couplings

A solution involves a bioinspired "root", a 3D printed coupling which extends into the silicone. This root follows the principles of tree roots, which are fractal to maximise surface area to create grip

in soil. This allows the tree to exploit the friction forces between the ground and it's roots, which is proportional to the amount of surface area exposed to the dirt. This principle was practiced with silicone by producing 3D printed lattices with cavities. The cavities allow the silicone to cure around the lattice while exploiting the relatively high strength of PLA. This principle was prototyped and seen to be effective.

To assess the applicability of the principle to application it is important to understand the coupling's hysteresis and failure modes. A reliable coupling would not exhibit excessive hysteresis in actuator force-displacement ranges. Any hysteresis on a locomotive platform would incur significant control challenges. It is also useful to understand how the presence of the root embedded within the SEE changes the deformation response of the SEE from a standard free test.

#### 4.5.2 Methodology

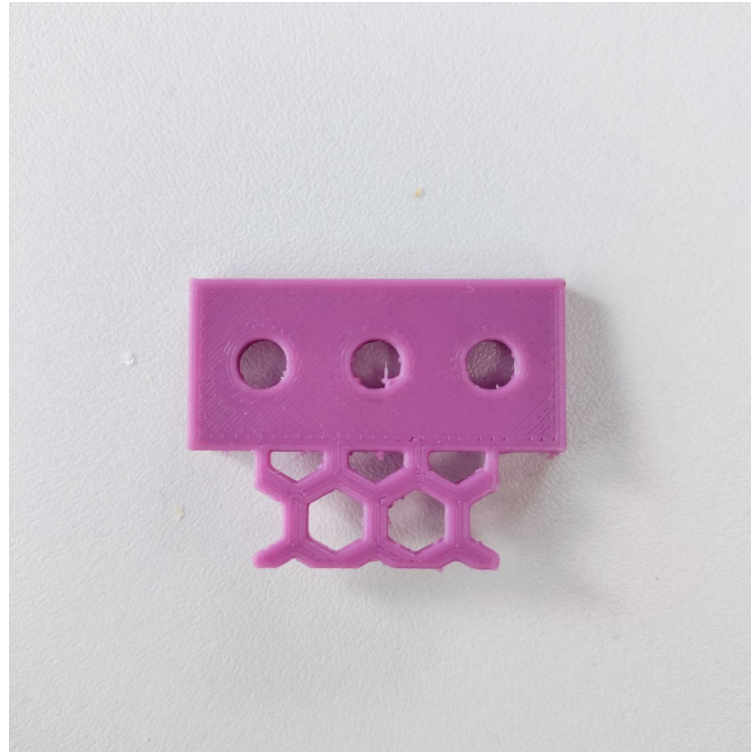


Figure 4.12: Example root with variables:.... Note the exposed sides towards the bottom of the root.

A coupling must be able to withstand the forces and displacements experienced during an actuation without significant hysteresis. Hysteresis in locomotive robotics would have a significant impact on the efficacy of a controller.

The width and thickness of the root protrusion were selected based on the test SEE geometry, itself chosen to be a compromise between matching the actuator's geometric magnitude and reducing silicone consumption. The root allowed for clearances in all directions so that the root embedding could be total and avoid sharp edges in the silicone. Molds were designed to allow the roots to be embedded. Each SEE was created with shore hardness 20A silicone

For an initial feasibility study, a number of roots were constructed. For all experiments, the

effective length of the SEE, defined from the tip of each root, remains constant at 80mm, along with thickness [6mm] and width [30mm]. These values were chosen to reflect the approximate size of an SEE of a PH-SEA, providing room for root variations and consuming a moderate amount of material per test. The shore hardness of the silicone was also maintained at 20A (Smooth-On MoldMax 20. ) as it was theorised issues of root pullout or silicone destruction would arise more frequently in more compliant silicone. Initial investigations looked at a single shape: a lattice of hexagons. The hexagon lattice structure was chosen to produce low weight roots with high stiffness and strength<sup>[67]</sup>. Each was manufactured using a 3D printer (Ender 3 v2 - PLA) using a 0.4mm nozzle and a layer height of 0.16mm and printed so that layering plane is normal to loading to reduce the probability of layer pulloff. The shape and size of the cavities was maintained while variables:

- Width of the root  $[W_r]$  := Largest lateral length of the root embedded into the silicone.
- Penetration depth  $[D_r]$  := Largest longitudinal length of the root.
- Thickness  $[t_r]$

Were changed, in a such a way that the hexagons were cut in discrete. Each of these parameters will have also vary metrics:

- Enclosed Volume  $[v_e]$  := Silicone volume captured in root.
- Effective Surface Area  $[A_{eff}]$  := Root surface area in line with tensile forces (Angled faces contribute via their vertical components).
- Total Surface Area  $[A_T]$  := Total submerged surface area, regardless of orientation.

All SEEs were molded using 20A silicone in 3D printed molds. Silicone was degassed using a vacuum chamber before curing to mitigate the formation of bubbles within the SEE. Roots are placed into the mold before pouring and held in position by screws. Excess silicone was removed with a scalpel after curing.

The question of failure mode was investigated using tensile mechanical testing on 3 initial samples of same root geometry. This test helped benchmark absolute failure and provide understanding of the failure modes. Moreover, this test provided clues to the onset of hysteresis. Each root was clamped to the testing machine and loaded until failure.

These tests indicated the potential failure mode and force regions where potential hysteresis could occur.

New samples were then loaded in 5N increments cyclically between a 5N range, starting before the indicator of hysteresis at 40N . This test is designed to narrow the hysteresis onset region.

To understand if there is significant hysteresis within the samples were oscillated between displacement set points for 200 cycles at  $750\text{mmmin}^{-1}$  in a displacement range more applicable to the Peano-HASEL.

#### 4.5.3 Current Results

Unfortunately, results for this study are limited due to a lack of available silicone to make samples. More is on order to complete these studies. However preliminary results have been obtained. During failure testing, the roots failed inconsistently in the force range  $64.8 \rightarrow 84.6$ , corresponding to a displacement range  $123 \rightarrow 150$ . This particular root geometry features small hook-like extrusions (Figure.4.12). These are a product of the method used to draw the root in CAD and were initially

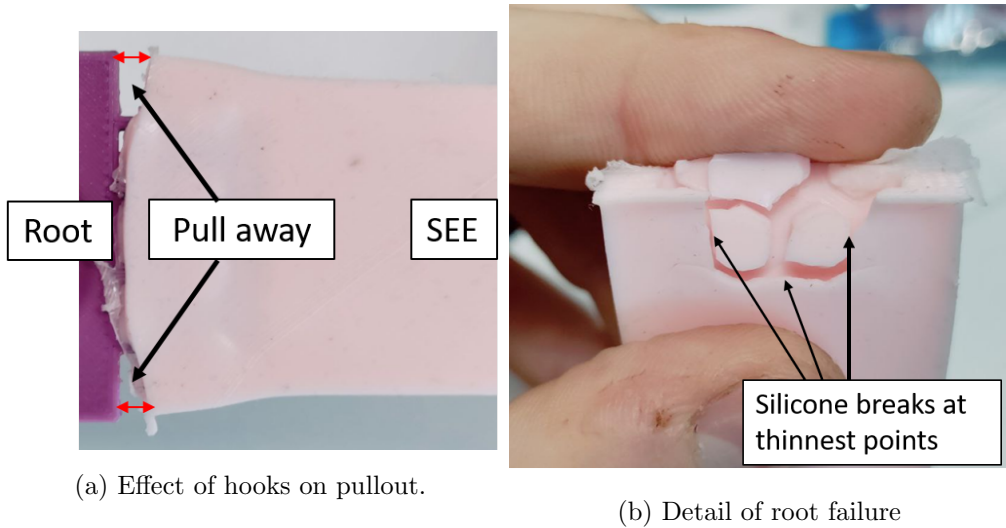


Figure 4.13: Demonstrations of root interactions with SEE during loading and after failure.

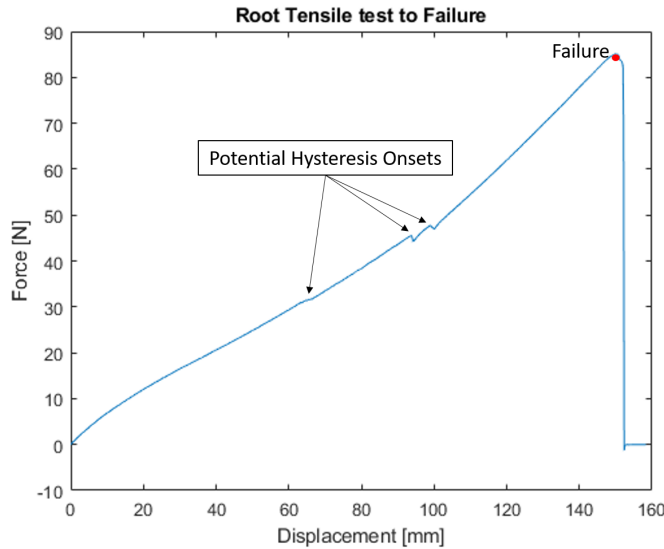
thought to be inconsequential to the SEEs response. However, as shown in figure.4.13a, the lack of closed volume these hooks created allowed the SEE to pull away from the root at the sides. A bench-marking study, without roots present, is needed to assess the impact of this on the force-displacement response. With respect to failure, these hooks would detach during loading before total failure, potentially altering the SEE's response and contributing to hysteresis. The hooks could be replaced easily into the silicone, suggesting this is purely a consequence of the lack of enclosed volume. This will need to be corrected with future tests.

The SEEs all fail due to silicone splitting in the thinnest parts that sit on top of the PLA, shown in figure.4.13b.

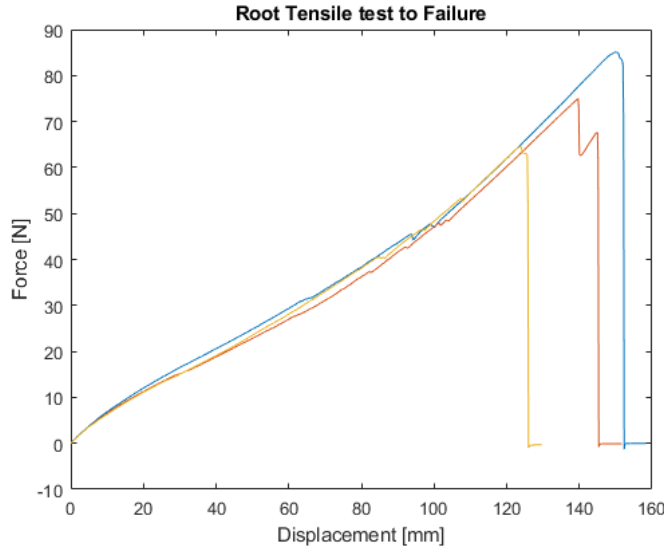
The region labelled in figure.4.14a was suspected to be the onset of hysteresis due to the discontinuities observed in the force and a period of negative force gradient.

The hysteresis onset was tested using a ramping cyclic test that brought the SEE directly to a force set point  $F_{set}$ , before oscillating in a range:  $F_{setN} \leftrightarrow F_{set} + 5N$ . This was done for 20 cycles before incriminating to the next set point. Figure. 4.15d demonstrates that as the force range increases, the effect of hysteresis increases. This can be seen by the sliding of the force-displacement loops during the cycles. The magnitude of the sliding increases with the force range and is especially prominent at  $65N \leftrightarrow 70N$  before ultimately the root fails. The unloading and reloading of an SEE produces a response which returns to the the last point of hysteresis, suggesting that the root pullout is not affecting the elasticity of the SEE and instead is settling into a new equilibrium during hysteresis.

The onset of this behaviour is far beyond the displacement range of the Peano-HASEL actuators used in this work, so the root was cyclically tested in a displacement range more applicable to actuation. No hysteresis was observed in the sample in this displacement range and the cycles appear consistent. Some minor variation in force was observed, but an Fast Fourier Transform of the force cycles reveals 3 distinct peaks which correspond to the 3 cycles.



(a) Characteristic failure test of initial Root Test to demonstrate hysteresis onsets are potentially located at plateau regions or large negative force gradients.



(b) Force-Displacement curves for all samples tested to failure.

Figure 4.14: Failure testing of root based SEEs.

#### 4.5.4 Discussion

These results should be considered preliminary. Due to the lack of material, samples were limited and tests were undertaken with this in mind to gather as much information as possible. The tests would change and could not be restarted again due to the lack of samples. This study is considered inadequate and sporadic for one to draw any significant conclusions. More tests to confirm repeatability as well as expand the results to other root geometries are still required in order to assess the validity of the results and no conclusions can be drawn from the results about

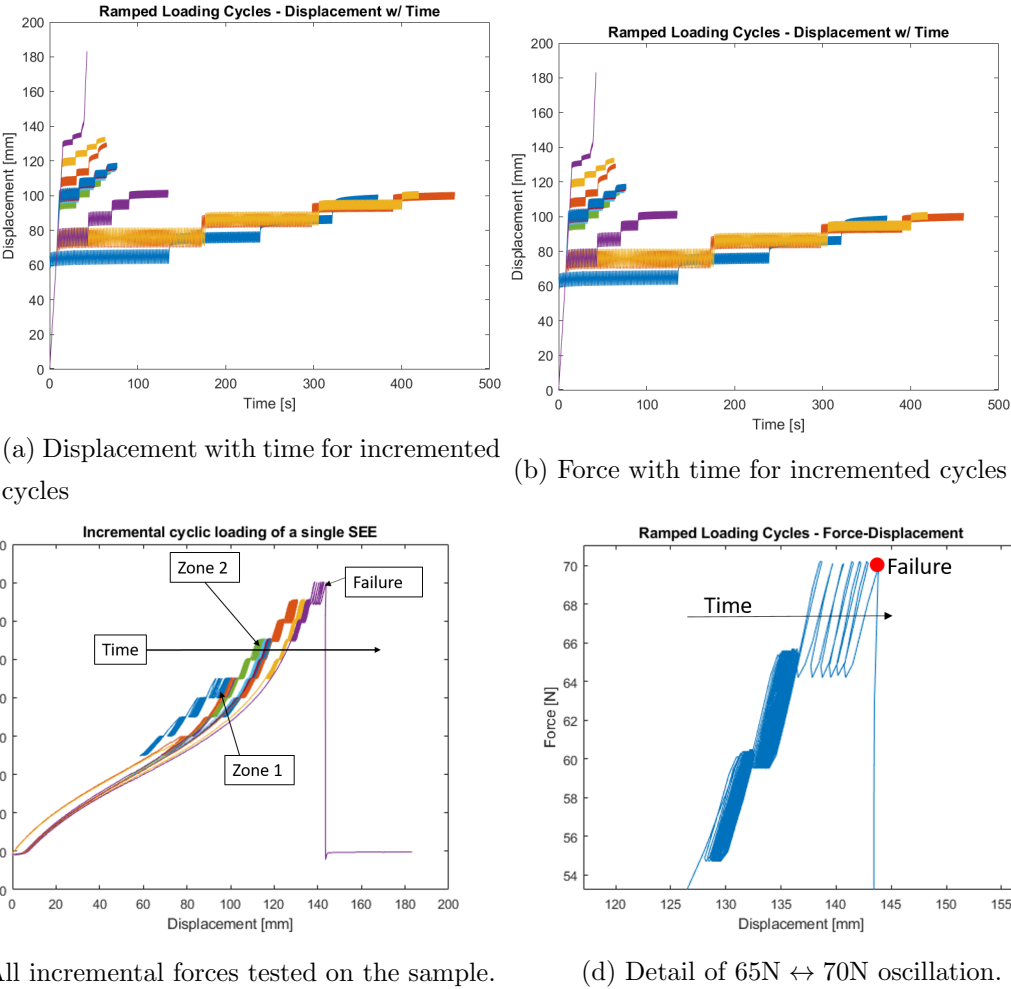


Figure 4.15: Ramping Cyclic Loading tests. The SEE is loaded between an incrementally increasing force range. 4.15a shows the evolution of the dependant displacement with time. 4.15b shows the controlled variable force with time. 4.15c shows the behaviour of the SEE during loading and unloading. As time progresses, the response is shifted to the right by the hysteresis curves. Significant hysteresis is observed in zone 1 & 2, but on subsequent loading the magnitude of the hysteresis is smaller suggesting a settling of the root into a new stable seating within the SEE. 4.15d shows detail of the last loading before failure where significant hysteresis occurs at  $65\text{N} \leftrightarrow 70\text{N}$ .

the impact of the defined variables. These tests if anything provide lessons learned to carry out a more rigorous and scientific study.

Nevertheless, these results indicate that, within the Peano-HASEL's actuation range, the effect of hysteresis is not present and the response of the SEE with the root is fully elastic. This can be seen by the 3 distinct peaks in the FFT (Figure.??), which shows that the three tests dominate the power density spectrum, indicating minimal change in the SEE's response. This suggests the coupling solution is applicable to the Peano-HASEL SEA. What the results do not indicate is the number of cycles taken to induce failure. Peano-HASELs have been demonstrated to fail at  $\approx 20,000$  cycles<sup>[50]</sup>, so any coupling must at least match this standard. Further testing should look

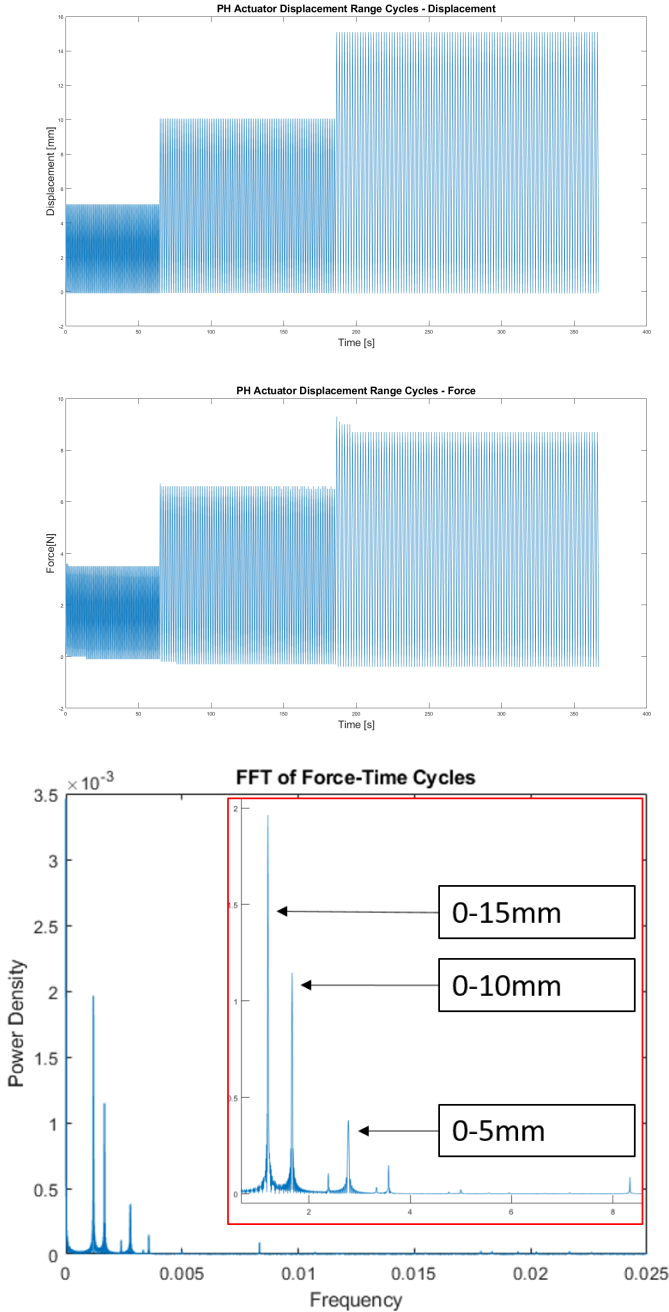


Figure 4.16: Displacement oscillations in Peano-HASEL range.

to explore this.

However, in more complex applications, it is possible that a SEE could experience pre-loading due to the motion of joints, for example, in crouching motions, exerting a pre-stretch onto an SEE. In this scenario, the displacement range could far exceed the Peano-HASEL's displacement range. Further tests are needed which probe the cyclic response of a root by incriminating the maximum displacement further towards the failure region observed in figure.4.15d.

The failure mode was in every case the silicone tearing in the thinnest points. Future designs will need to address this. This thickness of the root is likely excessive as no noticeable deformation was observed and no SEE failed due to the root fracturing. A reduction in root thickness would likely only increase the ultimate failure point.

#### 4.5.5 Conclusions

The introduction of PLA roots appears a promising method to achieve coupling between silicone elements and Peano-HASELs from these results. The limited data suggest actuation is repeatable in the required actuation ranges and the failure points are far from the outputs of the Peano-HASEL. Moreover, these conclusions are drawn on roots with the hooks, which have been observed as a key contributor to failure. Lessons have been learned with respect to the root design and future iterations will look to avoid the hooks seen in these preliminary investigations.

No conclusions can be drawn for roots with different parameters to the ones tested here. Future work will look at more roots which explore the variable space to conduct a sensitivity analysis of how these variables affect the onset of hysteresis, total failure and longevity.

### 4.6 Initial Investigations of Variable Stiffness

The variable stiffness component of the PH-VSA is inspired by the observations that the pennate muscle structure interacting with the aponeurosis causes lateral deformation and thus changes in stiffness in the tendon in natural systems<sup>[8;62;5]</sup>. To investigate the applicability of this idea to silicone SEEs, initial experiments were designed to create lateral deformation at one end of an SEE and investigate the impact of this deformation on the stiffness response of the SEE.

#### 4.6.1 Methodology

Examples of testing samples are shown in figure 4.17. Each sample is the same geometry, measuring 10x60x3mm, made of shore 20 silicone. The samples are designed with attachment tabs to allow interaction with a mechanical testing machine, measuring 10x10x3mm. Each is deformed linearly in tension up to 50mm of stretch and force-displacement data collected to allow calculations of stiffness behaviour. The tabs are made from a high stiffness silicone (Shore Hardness 50) to provide compliant but well adhered couplings between the SEE and the testing machine. The same silicone is used to manufacture lateral displacement tabs measuring  $5 \times l \times 3$ mm, where  $l$  is the length of the tab in the tensile direction. This defines two distinct regions of the SEE: the deformed region, enclosed by the lateral tabs, and the free region. The length of the free region can then be written as  $L = 60 - l$ . These are holed with M2 clearance to allow pinning to a backing board that is 3D printed. The holes are vertically spaced in 5mm increments to provide adequate spacing but leave enough material to maintain strength. Naturally there is some deformation of these tabs, but this is also true of the aponeurosis, and this investigation is to determine *if* the principle applies and the impact of relative variables, rather than to investigate its effect on a specific and applicable SEE. M2 clearance holes are left in the backing plate at regular 4mm intervals to provide displacement iteration, with the first set fixing the lateral tabs in their resting configuration. The experiment therefore provides insight into a relationship between a potential change in stiffness and a lateral deformation.

To provide a reference for stiffness changes, the SEE is tested in tension without any lateral displacement. This benchmark is tested with the high stiffness lateral deformation couplings included

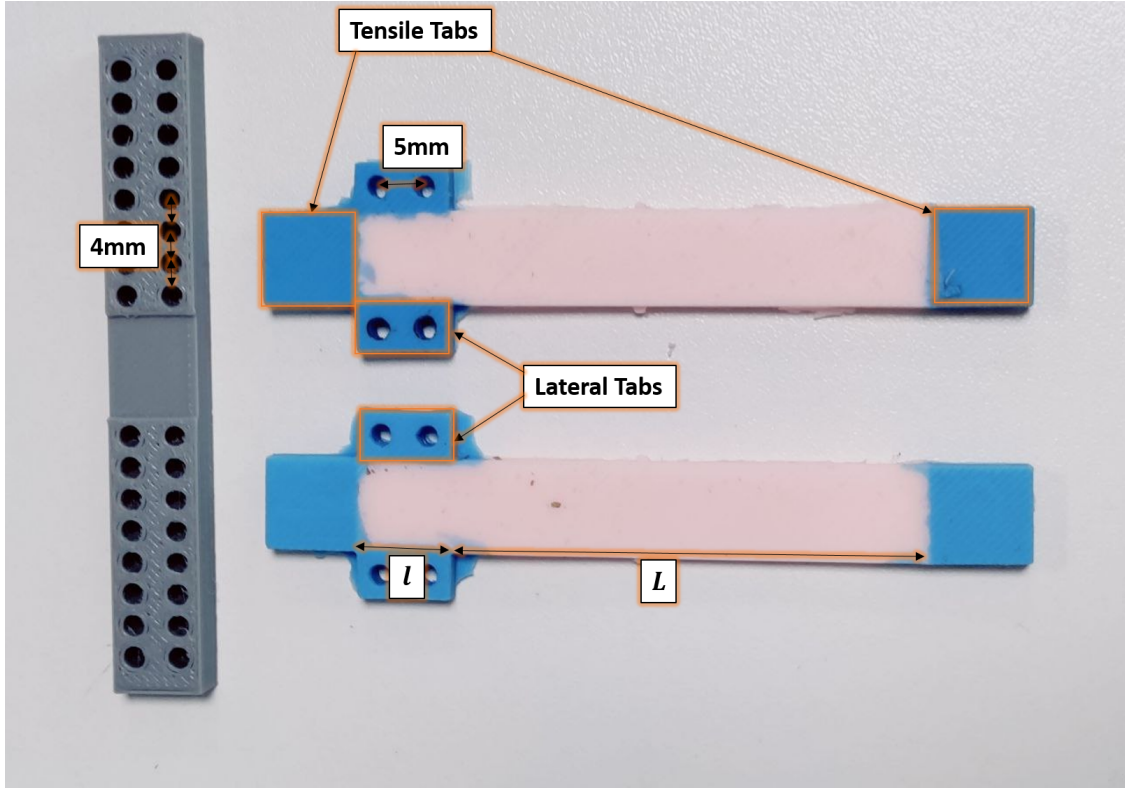


Figure 4.17: Demonstrative picture of variable stiffness samples.

in the SEE as their inclusion on the sides of the SEE may have a minor impact on the overall deformation.

The tabs are then displaced along the backing plate incrementally and each iteration is tested. This methodology gives rise to two key variables for this study:

- The length ratio  $\frac{l}{L}$ , describing the ratio between the free length  $L$  of the SEE and the length influenced by the lateral tabs  $l$ .
- The displacement of the lateral tabs  $d$ .

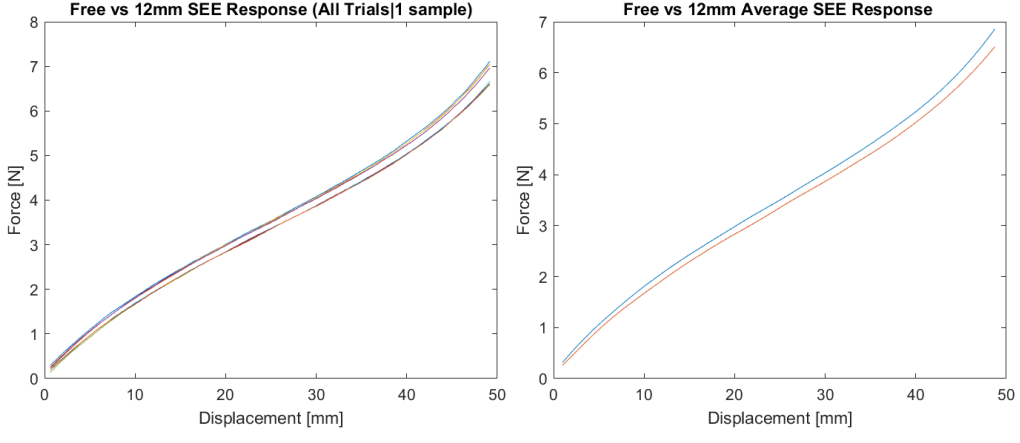
#### 4.6.2 Results and Discussion

Similar to the PLA roots investigations, these tests are hampered by lack of material. However some preliminary investigations were carried out. However, a number of failures of experimental samples prevented conclusive results. Figure.?? highlights some of these.

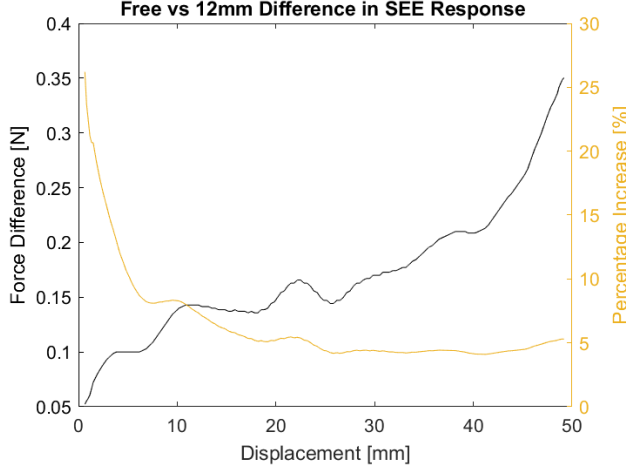
4 samples were tested and 2 failure modes were observed:

- Interface pull off.
- Silicone tearing around holes.

Initial tests were plagued with failures of the interfaces that connect the 50 shore silicone to the 20 shore (Figure.4.19b. It appears inconsistent as to when these will fail and some of the interfaces are in fact quite resilient to pull off. While it would appear to be a product of the manufacture, tabs on



(a) All trials with both free and 12mm lateral displacement. (b) Avg of the trials of free and 12mm lateral displacement.

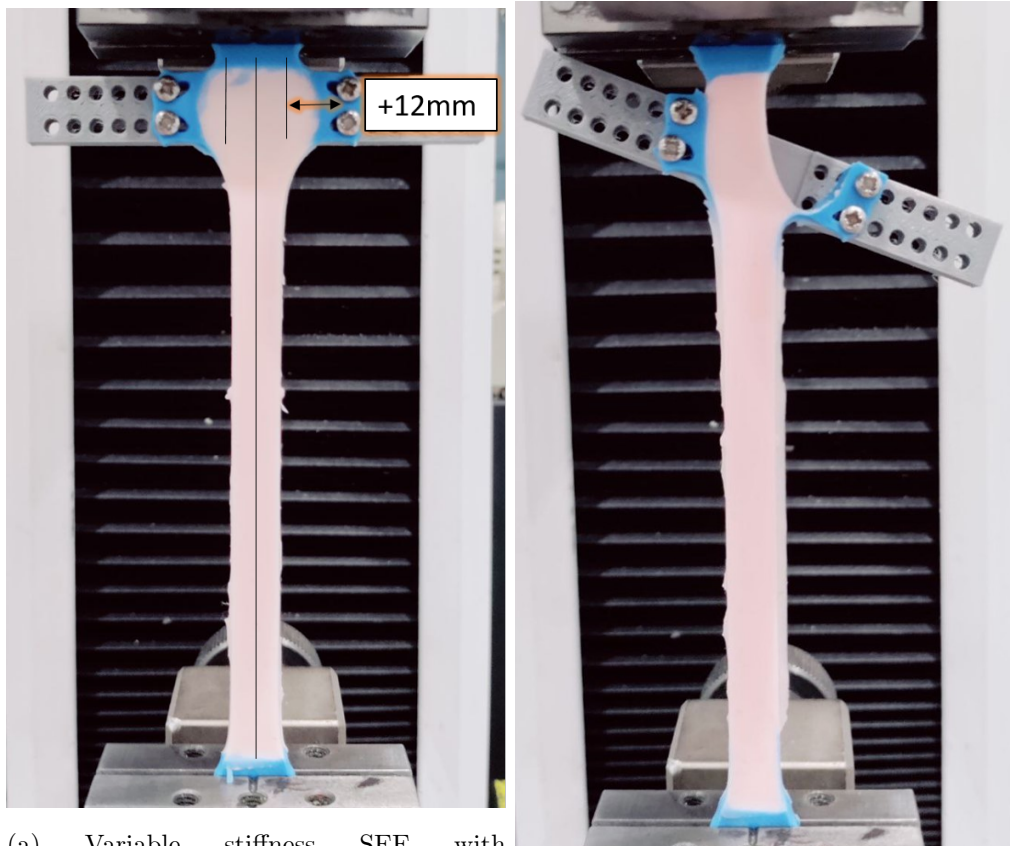


(c) Differences in force between the free and 12mm lateral displacement.

Figure 4.18: Results for the successful variable stiffness sample

the same sample experienced radically different failure loading. In order to provide results, future samples will need a stronger coupling that can withstand the lateral and tensile forces exerted to create variable stiffness and to produce loading. This may require better knowledge of the effect of curing time between silicone pours or a different coupling such as a PLA Root methodology as discussed previously. If silicone tabs can indeed be used with an adjustment to manufacturing, the tabs require more auxiliary material around the holes to prevent tearing, especially on the side of the hole which interacts heavily with the screw under tension.

The results of a successful test (Figure 4.19a) do show a small change in the stiffness response of the SEE between a free SEE and the same sample with 12mm lateral displacement (Figure 4.18). This is promising for the aponeurosis mimetic approach, although the magnitude of this difference is small. It is possible that this may be a product of the small geometry selected for these investigations. The percentage change indicates that the variation in force is non-negligible, but rapidly decays as the forces in the SEE increase. More stable tests are needed to understand the effect of further displacing the SEE laterally and confirm this result.



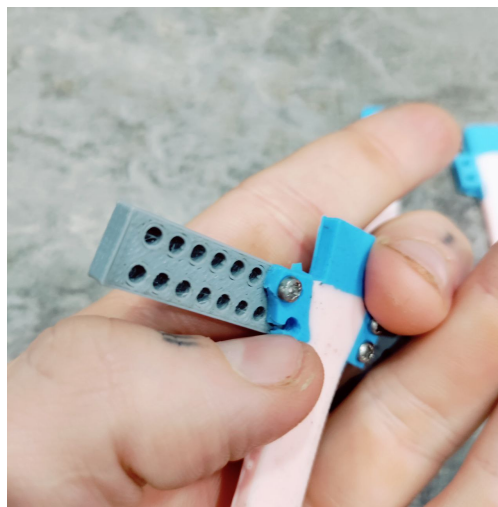
(a) Variable stiffness SEE with

12mm lateral displacement each side.

VideO:<https://tinyurl.com/3jzmuf5a>

(b) Example pull-off failure. Videos:

<https://tinyurl.com/2p8r26t5> - <https://tinyurl.com/5cezydbz>



(c) Example hole failure.

Figure 4.19: Comparison of successful vs failed variable stiffness tests. 4.19a: Working variable stiffness SEE with the aponeurosis displaced. Results for this test are given in Figure 4.18. 4.19b: Example Pull-off failure of silicone tabs at 12mm lateral displacement. Note that any of the tabs could fail and which failed was highly variable. 4.19c: Hole failure around the screws. Only one of these failures was observed across 4 samples.

### 4.6.3 Conclusions

These results point to the principle of lateral displacement as a mechanism to produce controllable variable stiffness responses in silicone SEEs. Further tests will look to replicate and validate this initial result while investigating the impact of the defined variables. Attention to the design of the SEE is needed and the modification to PLA roots will be implemented until the investigations of silicone interfaces are completed. As the stiffness change is relative in this work, the impact of the PLA Root on the stiffness response is not relevant to this investigation. This result is promising to the realisation of the PH-VSA, indicating that variable stiffness can be achieved with the introduction of pennate actuators, utilising the linear actuation mechanisms of the Peano-HASEL.

## Chapter 5

# Series Elastic Element Optimisation with Genetic Algorithm

In nature, systems are refined via selective pressures. This results in highly efficacious evolved components that compliment one another. Engineering often employs similar evolution inspired optimisation techniques in the hope of mimicking these principles.

With respect to the Peano-HASEL SEA, the non-linearity of the Peano-HASEL's actuation response alludes to the benefits and possible necessity of non-linear series elastic elements and indeed numerical investigations of existing analytical models support this hypothesis.

The nature of the Force/Strain relationship is shaped by the  $\frac{\cos(\alpha)}{1-\cos(\alpha)}$  term. When the actuator deforms, its force output monotonically decreases relative to this characterising curve. As a spring's force output increases as a function of strain, it is natural for the two to be plotted together. As the force of the spring's tension is acting as the load on the Peano-HASEL, there is a point in which the spring's tensile forces overcome the actuators force output. This sees the actuator blocked as a result: i.e. there exists a maximum extension for a given spring (Fig. 4.5). This maximum extension is capped by the actuator's geometry, but deviates below this with spring stiffness variation. From discussions of the biomimetic SEAs, a key metric in transient force generation is the amount of the actuator's energy that is stored inside the series elastic element. When the actuator is blocked, this also coincides to the maximum stored energy. Taking the integral under the two stress/strain curves gives the energy stored in the spring (assuming full elastic recoil) and 100% energy transfer efficiency). Using a linear, Hookean spring response of the form:

$$P(x) = kx$$

the maximum possible energy efficiency of the SEE is 40% of the actuators energy, but because the SEE is overtly stiff, this blocks the actuator earlier and the actuator produces less energy. An example behaviour is shown in figure.4.4, with the optimal point marked.

As previously investigated, geometric modifications and material variation may facilitate non-linear SEE responses. A genetic algorithm (GA) is proposed as a methodology for achieving this. These algorithms are biomimetic, based on natural evolution, and work by creating a population of candidate solutions (individuals) and evaluating their fitness via a fitness function. The fitness is used to weight probabilities of genetic evolution operations such as mutation, reproduction and elitism (Figure.5.1). Genetic algorithms can allow complex geometries to be defined and explored that optimise to the problem at hand, beyond the scope of conceivable geometry modifications and material combinations. Exploring this space manually would take considerable time and iterations.

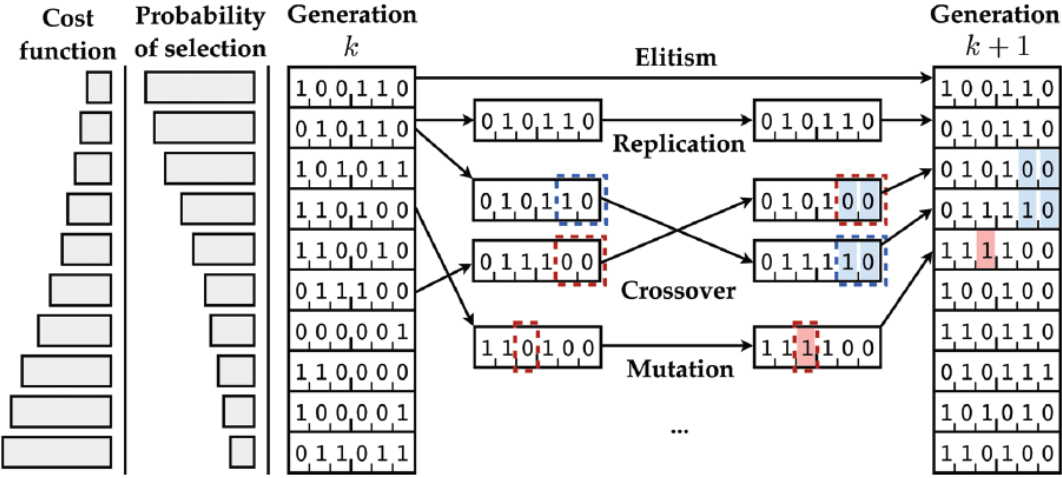


Figure 5.1: Genetic Algorithm operational cartoon demonstrating standard workflow and generalised genetic operations, from Brunton et.al (2015)<sup>[18]</sup>

The choice of genetic algorithms over other optimisation schemes is made due to their efficacy in tackling non linear problems and ability to escape local minima in highly complex feature spaces. Optimisation schemes such as this can also produce unexpected and desirable results with a well defined cost function and optimisation operations. The genetic algorithm architecture also lends itself well to the complex modelling and simulation used here to increase optimisation accuracy. Genetic Algorithms also allow for optimisation without analytical equations which would be time consuming to derive and onerous to manipulate. While this may require a more unorthodox optimisation procedure, it does facilitate optimisation beyond usually accessible problems.

After initialisation, there are 4 major steps in this optimisation, demonstrated in figure 5.2:

1. Generate geometries from numeric, optimisable representations
2. Simulate loading geometries with a Peano-HASEL muscle using finite element analysis (FEA)
3. Evaluate objective function to obtain fitness of individual.
4. Perform genetic operations for optimisation

This loop is repeated until a convergence is observed in fitness of individuals or a generation cap is reached.

Matlab 2022 was chosen for writing the GA as it provides accessible parallel computing capability as well as partial differential equation support via the PDE toolbox. Parallel computing may be necessary due to the large populations sizes requiring modelling and simulation each generation. Depending on the resolutions used for simulations, this could impose large time constraints on computations. Parallel computing allows the use of many CPU computing clusters to reduce solution times. The PDE solver allows for FEA solutions within Matlab.

## 5.1 Objective Function and Bounds

An optimisation scheme requires sensible and thought out bounds so as to constrain the optimisation to realistic solutions. Moreover, a well thought out cost function is necessary in order to

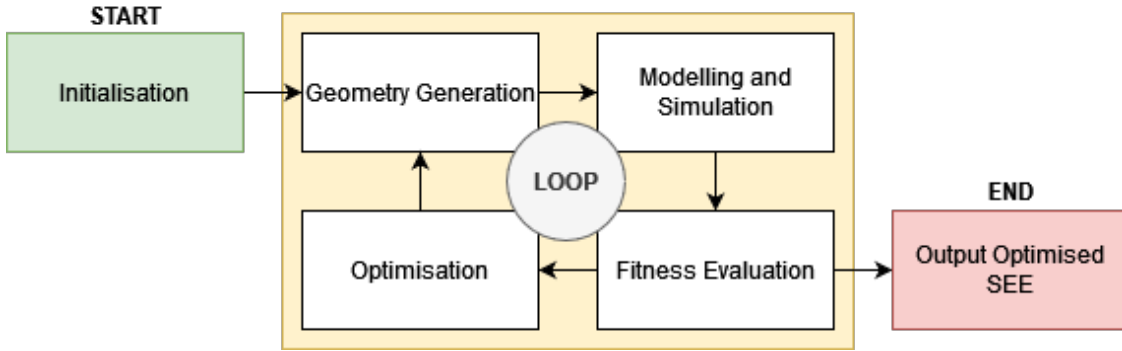


Figure 5.2: High level workflow of Genetic Algorithm optimisation. The loop is iterated until defined exit conditions are observed.

facilitate solutions that meet design requirements. This optimisation requires both geometric and material property bounds. SEEs are restricted geometrically by the peano-HASEL actuator size and manufacture limitations as upper and lower bounds respectively. Material limits are imposed by the available silicones. A theoretical continuum of shore hardness can be achieved by mixing different ratios of the available shore hardness up to the smallest and largest of these values.

The objective function is developed around the jumping use case, with attention paid to the energy storage capability of an SEE as well as it's mass. Energy storage is a large component of the power modulation attribute desired of the SEE. Mass is also a factor of consideration for jumping as a heavier SEE would require more energy to accelerate. The optimisation scheme currently omits transient responses of the SEE. This then omits vibration and damping analysis which will also play a role in selecting an optimal SEE. Again this will be part of future work and the cost function will require modification in this regime.

The current objective function takes the form:

$$\text{Max} \left[ k_1 \int_0^{x_{max}} F_{see} \frac{F_{see}}{F_{act}} dx + k_2 \frac{1}{m} \right] \quad (5.1)$$

$F_{see}$  is the tensile force generated under loading by a simulated Peano-HASEL actuator.  $x_{max}$  is the maximum deflection achieved until  $F_{see}$  exceeds the actuator force  $F_{act}$ . The ratio  $\frac{F_{see}}{F_{act}}$  represents the efficiency of the energy transmission between actuator and SEE. This is designed to not only promote high energetic magnitude solutions but also those which capture the largest energy possible in the actuation.  $m$  is the SEE mass, which is calculated using the silicone density and volume. Lighter SEEs produce higher mass specific energies, a desireable trait for locomotive robotics.  $k_{1,2}$  are controllable scaling factors to promote or suppress aspects of the objective function.

## 5.2 Geometry Definition

The optimisation scheme requires an encoding of geometry and materials that can be interacted with by the genetic operations. Geometry parameters are encoded in a *seed* (traditionally a “chromosome”), which is simply an array of values that can be interfaced with by the optimisation. For this scheme, geometry can be varied in both 2 and 3 dimensions using different geometry generation algorithms with seeds of similar structure. The choice of algorithm can be controlled before optimisation begins in the initialisation. The resolution of the generator, governed by the parameters

$m$  and  $n$  is also controlled in initialisation. The length of each section of the SEE in both cases is defined by  $\frac{L}{m}$ .

### 5.2.1 Two Dimensional Geometry

The seed used for two dimensional geometries starts with two values representing the length  $L$  and thickness  $t$  of the SEE (For a diagram see figure 5.3). The material properties of each of the  $m - 1$  sections of the SEE are given by the elements  $S_{1 \dots m-1}$ . The next values define the width vectors,  $w_{1 \dots m}$  of the SEE. Each is half the total width at this point and each vector is mirrored about the central axis. The next value is the width of the bottom of this section and the top of the next. Sections are compiled together until the length has been fully defined. The geometry is extruded to thickness. There are  $m$  sections of equal length along the SEE. The seed is thus  $1 \times 2m + 1$  elements ( $m - 1$  material values and 2 length/thickness values):

$$\text{Seed}_{2D} = [L, t, S_1 \dots S_{m-1}, w_1, \dots w_m] \quad (5.2)$$

Moving average smoothing is then carried out to avoid excessive variation in the SEE that could produce observed meshing errors in modelling and simulation stages.

The two dimensional case is geometrically bounded by constraints defined in the initialisation:

- Thickness:  $t_{min} \leq t \leq t_{max}$
- Width:  $w_{min} \leq w_m \leq w_{max}$

allowing the algorithm to explore realistic geometries.

### 5.2.2 Three Dimensional Geometry

Seed structure for the three dimensional case is fairly similar to the two dimensional case, but omitting the thickness term in favour of  $n$  extra elements perpendicular to the tensile direction. The geometry in this case is generated by building  $m$  equally spaced fans of  $n$  unit vectors, distributed equally about a circle centred on the main axis of the SEE by an angle  $\theta = \frac{2\pi}{n}$ . Each geometry value  $v_{m,n}$  of the seed defines the length of each vector. Again, the material properties of each section are given by  $S_{1 \dots m-1}$  elements of the seed. For the 3D case the seed is  $1 \times m(2 + n)$ :

$$\text{Seed}_{3D} = [L, S_1 \dots S_{m-1}, v_{1,1} \dots v_{m,n}] \quad (5.3)$$

Moving average smoothing is again carried out on each fan and then down each length of the SEE to mitigate meshing issues in modelling and simulation.

Geometric constraints are imposed by limiting the length of the vectors to the region between two co-centric cylinders coaxial to the SEE length:  $r_{min} \leq v_{m,n} \leq r_{max}$ .

## 5.3 Modelling and Simulation

Each SEE is converted to an STL. The top and bottom faces of each SEE are consistently labeled in all cases, allowing accurate assignment of boundary conditions in MATLAB automatically. Currently, the material properties of the Seed are unused as a method to accurately assign materials to different geometric regions is currently under development. The STL is imported and automatically meshed in polynomial elements.

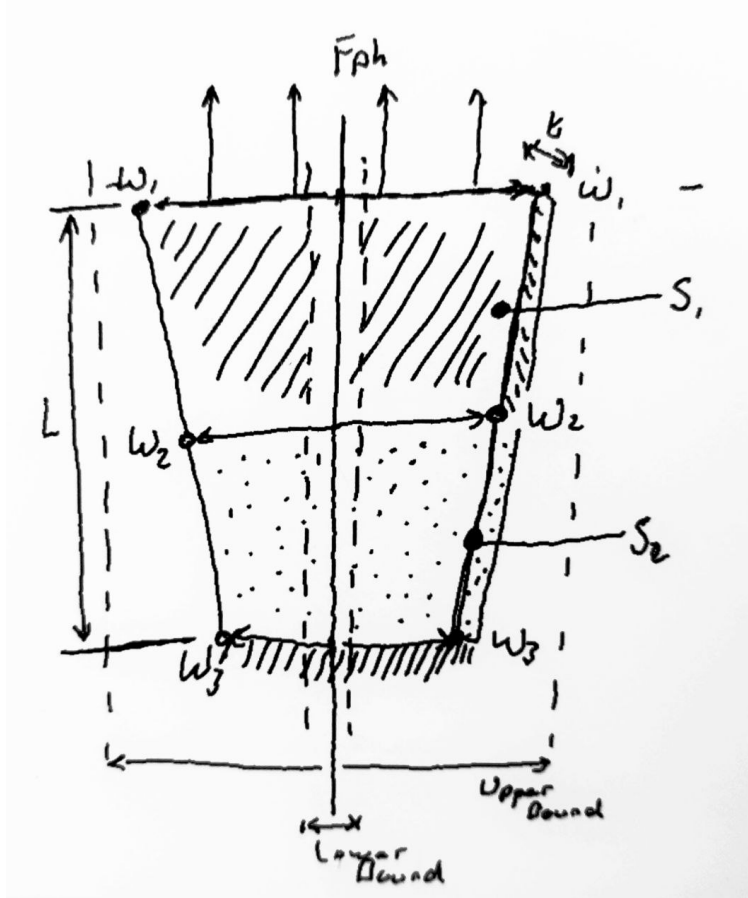


Figure 5.3: 2D geometry generator diagram.

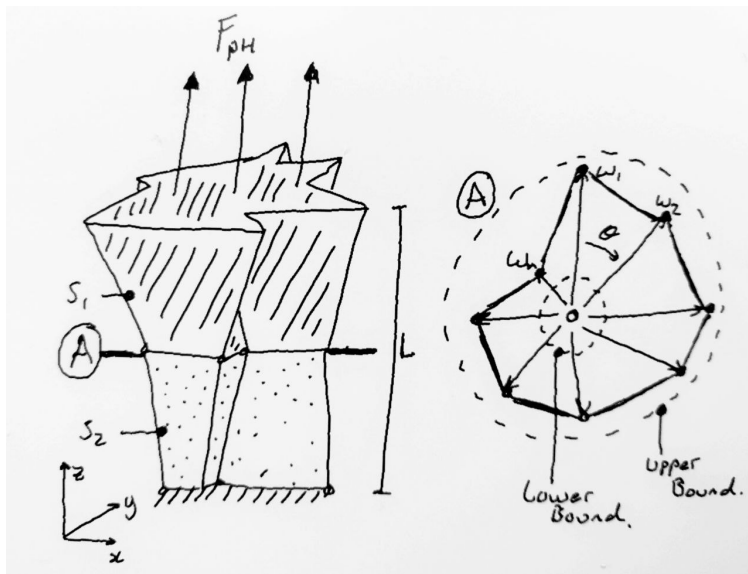


Figure 5.4: Geometry example for 3D case. Detail A shows a top down view of the vector fan. Not drawn with realistic proportions.

The SEE is fixed at one end in all DOFs by restricting all displacement of nodes on a plane, simulating the clutch used in a power modulating actuation mode, restricting SEE movement to build potential energy. The simulation runs in steps. For each step, the SEE is displaced a small amount. The reaction force in line with the displacement is then compared to the actuator force for this displacement, calculated using the Peano-HASEL analytical model.

The forces are compared to assess whether or not the actuator is blocked. If the actuator is not blocked, the displacement is incremented once more, else the actuator is considered blocked and the simulation terminates. The energy stored in the SEE is then calculated by taking the integral over the displacement of the reaction force. This method however neglects the energy stored by deformation of SEE elements out of line with the actuation force, which may be considerable. However, more involved methods of calculating SEE potential energy using volumetric strain equations currently produce unrealistic results.

Each step of the simulation is converged by reducing the mesh element size by 5% and assessing the discrepancy in the maximum Von Mises stress in the SEE and checking this against a predefined error cutoff. This is likely inefficient as specific regions cannot be targeted by the meshing algorithm and as such all regions are meshed with the same size. The presence of geometric features that require detailed meshing increases the overall complexity of the mesh considerably, even in regions where a simple mesh would suffice. This is a trade-off of using MATLAB's PDE solver.

Silicone is a non-linear elastic and as such there is no constant elastic modulus. To navigate this, a sample of different silicones with varying shore hardness were mechanically tested, the stress-strain results averaged and the stress-strain curve differentiated to provide a function representing the elastic modulus as a function of displacement:

$$E(x) = \frac{d}{dx} \left( \frac{1}{n} \sum_{j=1}^n \sigma_j(\epsilon) \right) \quad (5.4)$$

This can then be used for each deformation step of simulation, assigning material properties each time the simulation is run because the simulation is displacement based. This is valid as silicone is highly elastic with minimal hysteresis, but it must still be seen as an approximation.

## 5.4 Optimisation

Once each seed has been tested in simulation, the objective function is computed for each seed and this informs the seeds involved in the next generation's population. The fitness of each seed provides a probabilistic representation in a selection pool used for the genetic optimisations: the fitter the more represented. Firstly, the fittest of the population is transferred to the next generation automatically in an *Elitism* operation. The percentage of solutions subject to elitism is tuneable. Elitism is designed to allow optimal solutions the chance to stabilise and not be relocated by other optimisation operations away from their potentially optimal solution. *Crossover* selects two seeds from the pool and, using a defined index as a crossing point, swapping sections of the seeds, creating two new seeds. This is done with the intention of capturing favourable properties of both seeds, potentially seeing a drop in fitness of one offspring in favour of a fitness gain in the other. In the case of this representation, crossover translates to breaking each SEE along a certain plane perpendicular to its length and swapping the two upper sections. The crossover point is selected from a discretised truncated normal distribution, centred around  $\frac{m}{2}$  with a standard deviation of  $\frac{m}{4}$  in both 2D and 3D cases. The normal distribution is intended to provide significant variance in SEEs. The material properties are considered attached to the geometry and are crossed over

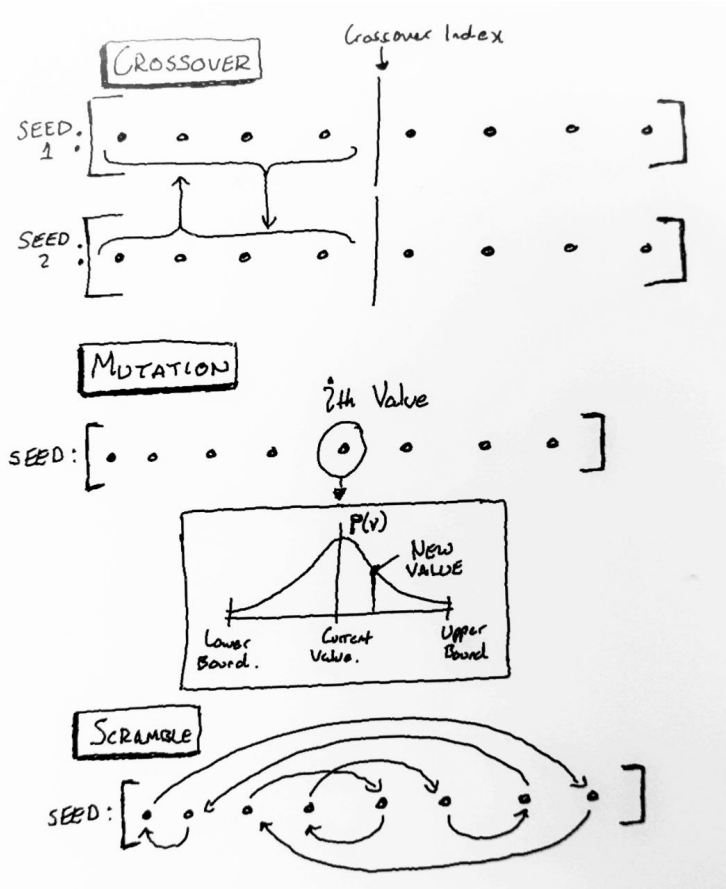


Figure 5.5: Characteristic cartoon demonstrating genetic operations Crossover, Mutation and Scramble.

equivalently. In the two dimensional scheme this includes the  $L$  and  $t$  terms. *Mutation* involves the increment of a particular seed parameter by a certain value. This can be carried out on any seed value within its respective bounds. Again, the mutation is performed with a truncated normal distribution with a mean as the current value and the standard deviation as one quarter the length of the bounds. Mutation is designed to allow solutions outside the current population to be found and break out of local minima. With similar intention, *Scramble* shuffles the indexes of seed without changing values. This allows for new material assignments and the movement of sections throughout the series elastic element.

The optimisation loop is carried out until a convergence is observed in fitness or a set number of generations is reached.

## 5.5 Results

To check that the scheme is effective, silicone elements were constructed that could easily replicated in the genetic algorithm by hard coding a representative seed. Using physical tensile mechanical testing, elements of 20A silicone were tested and the results compared to those generated by the simulation (Figure 5.6). The use of the function describing the infinitesimal elastic modulus pro-

duces results that do not replicate the real response of the silicone. It is possible this is because the current simulation methodology deforms the SEE from initial conditions each loop, rather than using the previous state. Using linear regression, a linear approximation was used in the genetic algorithm, following the same trend as the real sample however the silicone's response is quadratic.

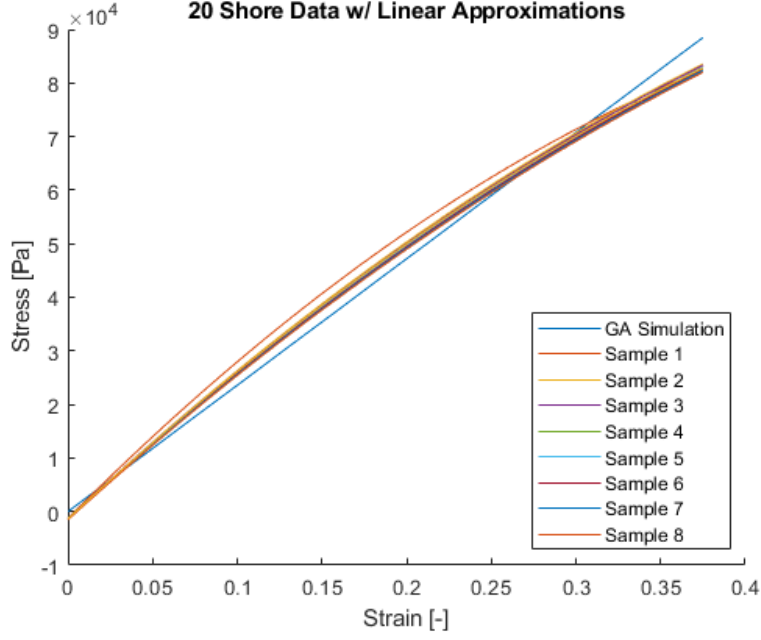


Figure 5.6: Comparison of experimental data, linear regression model and results of the genetic algorithms modelling and simulation. The difference between the linear fit and the genetic algorithm is imperceptible at this scale.

A more open optimisation was carried out using the genetic methods in order to understand how they behave. This test used 20 individuals for 10 generations (a total of 200 simulations).

In all tests, the Peano-HASEL actuation unit remains fixed with a signature:

$$[5 \mid 7 \mid 80 \mid 20 \mid 0.6]$$

Reflecting the scale of literature actuators and mimicking manufactured actuators for this work.

This test used the 3D scheme and the initialisation is presented in the table below:

The shore hardness was fixed in this test as currently the algorithm for generating geometry has no consistent and, crucially, automatic method for applying different materials. This is possible, but requires work in allocating names to geometric sections beyond standard methods. For now the shore hardness remains fixed throughout the SEE length. Moreover the seed currently only represents  $w$  or  $v$  values, so actuator length and in the 2d case, thickness, remain fixed currently. Allowing access to length and thickness is a desired piece of immediate future work that can be done quickly.

This test produced no observable change in fitness but did evolve the geometry of the SEE (Figure 5.7). This indicates that the scheme functions as intended but it does not produce fitness changes at this time.

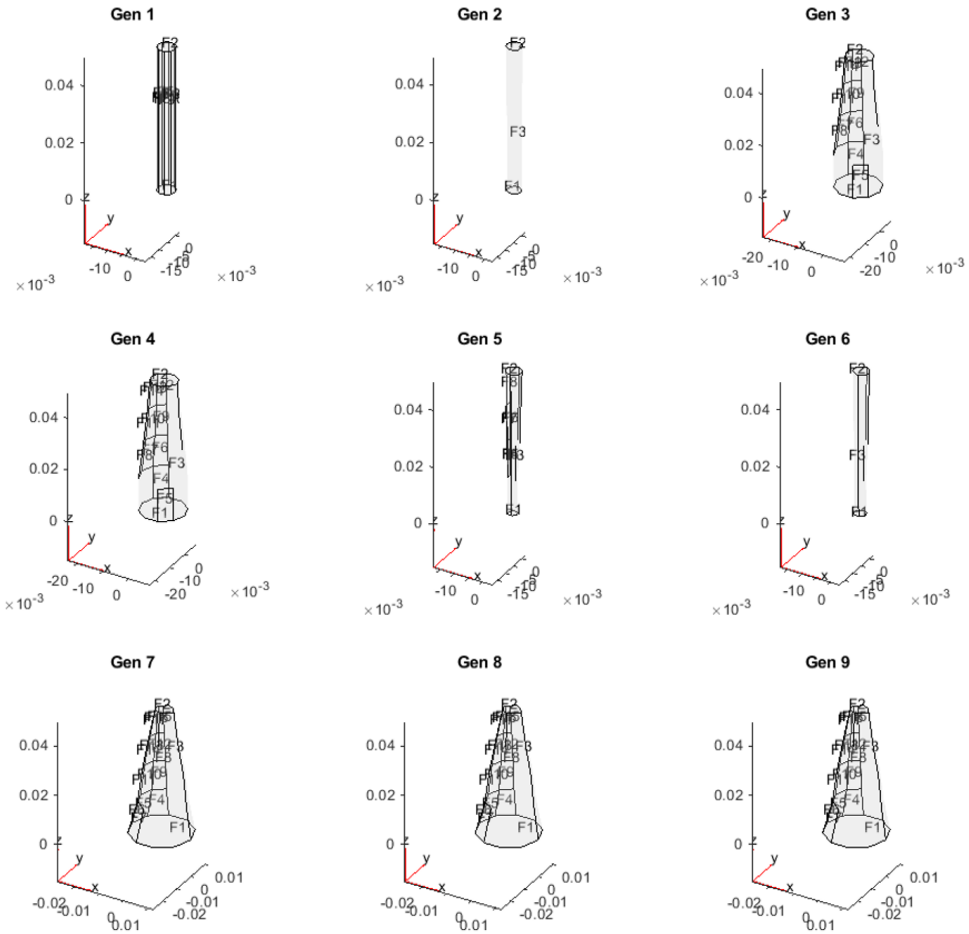


Figure 5.7: Evolution of a single SEE throughout generation

## 5.6 Discussion

Using a linear approximation is a current problem. Obviously this has not allowed for an optimised SEE beyond the numerical simulations using Hook's law. Methods of deriving Neo-Hookean models have shown good agreement with experiments for silicone rubber<sup>[77]</sup>, and this methodology can be employed in the modelling and simulation.

In future the multi-material expansion will be used as another major way to target non-linear responses, but more accurate response modelling may also be needed in tandem.

Results with the reduced optimisation demonstrate a minimal and functionally negligible improvement in fitness. This may be due one or a combination of a few factors:

Firstly, the reduced optimisation does not adapt length or thickness. It is highly likely that these will be critical to producing effective solutions. However, in most applications it is likely that length may be a fixed constraint, as mounting a PH-SEA on a platform will likely be bounded by such a problem. Therefore while length adaption will be incorporated in future work, the value of effectiveness of the optimisation may suffer loses in general applicability allowing this variability.

Parameter	Value
$L$	0.08m
Shore Hardness	20A
$E$	270456 Pa
$n$	10
$m$	5
Percentage <sub>Elite</sub>	10%
$k_1$	1
$k_2$	1
Bound <sub>up</sub>	0.025m
Bound <sub>low</sub>	0.005m

Table 5.1: Parameters for initial GA test

The inclusion of material adaption for each element is hypothesised to have a large impact on the fitness improvements of each generation. This is a major focus of future work in the next 3 months. Manufacturing of these SEEs with multiple silicons has been shown possible with prototyping and other experiments (Figure.4.19a, for example. However as mentioned in section 4.4.1, the strength of these interfaces and the variables that contribute to this strength must be investigated.

Another large factor of consideration is the nature of the optimisation operations. Both crossover and mutate rely on Gaussian distributions with bounds set based on mathematical intuition. Further work will look to optimise these operations, which may have a large impact on the magnitude of fitness gradients and the speed of convergence to optimal solutions.

## 5.7 Conclusions

So far the genetic algorithm's effectiveness at creating optimal SEEs for the PH-SEA remains ambiguous. While all the components are now operational, it is key to expand and investigate it's functionality to improve the fitness gradients. The FEA simulations can reproduce the non-linear response of silicone by assuming the elastic modulus is a function of displacement. Investigating parameters and genetic operations to improve fitness is a needed part of future work. Furthermore, the silicone interfaces will elucidate the potential to create multi-material SEEs consistently. This expansion is hypothesised to have a large effect on fitness gradients.

# Chapter 6

## Discussions, Conclusions and Future Work

### 6.1 Discussion

With the completion of the high voltage testing rig and successful manufacturing of Peano-HASEL samples completed and achievable, the project is in a favourable position for future work detailed below. The main modifications to testing now mainly focus on circuits and software (The changing of actuation signals, implementation of pennate actuator control, self-sensing capability).

Preliminary results of couplings can be validated and continued when materials are acquired. Initial results suggest that both solutions (Roots and direct silicone molding) have potential to be solutions, it is now a case of understanding what combination of variables produce effective couplings and validating this. The manufacturing of SEEs as detailed previously allows for a highly tuneable design space. It is critical to investigate silicone interfaces in the next month to understand how applicable this is so that the GA optimisation work can continue.

Investigations of SEEs in tandem with the genetic algorithmic optimisation will see the most attention in the coming months.

The high voltage rig is completed bar a few connections. These will be finished in the coming days after this report. All the necessary components are collated and the DAQ code written (Appendix A). Furthermore, similar research by other projects has lead to the creation of a 8-Channel high voltage controller SHVRIMPS which has been generously offered for use in this project. This increases the feasibility of the VSA and Machine Learning work as the construction of necessary circuits is no longer needed.

While inconclusive, the results of the initial variable stiffness tests suggest that the mechanism of lateral deformation does indeed produce a controllable change in stiffness responses that is non-negligible. Future work will seek to confirm this and investigate the impact of the variables state in section 4.6.

### 6.2 Conclusions

A main focus of this year has been the culmination of setting up consistent manufacturing and experimental capability. This is now established and puts the project in a favourable position

for rapid data collection that will likely see an increase in applicable results. Many delays were incurred in the ordering of critical materials and with the moving of support facilities to MECD there were many times that work could not progress as intended. Now that while much of the results presented here are preliminary, they are mainly hindered by a lack of material and failure of samples, which will be rectified next month (Oct2022). They also inform the process of carrying out future work as well as indicating failure points (Such as silicone tab pull-off in the variable stiffness experiments) that can be addressed in the immediate months.

The genetic algorithm is not up to full capability but initial tests suggest it is functional and the next steps are matters of improvement and tuning.

The support of the SHVRIMPS project decreases the time investment of all work involving multiple actuators and this potentiates progress.

Overall, while sporting sporadic results currently, the project is in a good position to continue and meet the project aim in the 15months time frame available and use the remaining 6 months as writing up period for the thesis. There is a clear line of research now focused on the silicone SEEs and their integration into the Peano-HASEL platform that provides a coherent body of work. Parallel research investigating Peano-HASELs and creating experimental rigs such as SHVRIMPS also support this work by reducing the scope considerably. The stretch goals can be reduced or removed as a buffer for the work directly related to the aim, but addressing them is desirable, while not necessary.

### 6.3 Overview of Future Work

Future work aims to realise the PH-VSA prototype and characterise its operation. This includes the evaluation of performance in 1DOF positioning tasks of a lone Peano-HASEL and a fixed stiffness PH-SEA, that involve moving between set points while under load, specifically looking at settle times and overall positional accuracy. Power modulation performance will be evaluated by testing high impulse movements of the Peano-HASEL under different static loads, first without series elastic elements and then featuring this extension, comparing the two in power.

The variable stiffness extension using the aponeurosis inspired approach will be continued. Testing here looks to understand the magnitude of variability in the stiffness from the pennate actuators and understand the factors that contribute to this. Moreover, can variable stiffness allow the mitigation of hypothesised trade offs seen in static stiffness systems between power modulation and positional accuracy tasks? This method of variable stiffness is also hypothesised to introduce capability for active vibration damping through direct counter forcing using pennate actuators. Methodology to test this hypothesis is still under consideration. This work will hopefully culminate in a publishable journal paper.

The extension to variable stiffness will require additional circuitry to regulate actuation voltages as well as consideration on the positioning of pennate actuators; work that will likely be carried out in collaboration with other parallel research projects for simulation and actuation rigs.

The genetic algorithm is a novel way to approach series elastic element optimisation facilitated by the characteristics of silicone and therefore results can likely be published independently of the above work once discussed improvements are made in the immediate months after this report. Undertaking this work in parallel with the SEA/VSA experiments is achievable and the genetic algorithm paper will support that work.

Completion of this work will realise the aim of the PhD.

Once the above is completed, a stretch goal is desirable to use the established PH-VSA platform as a basis to carry out investigations on machine learning based control, which is a prospering and

active research field. This work will look to understand the benefits and drawbacks of machine learning control with the Peano-HASEL VSA and seek to improve on the performance seen in the previous work. To realise this work, proprioceptive sensing capability needs to be introduced to the PH-VSA; the algorithm written and then trained; before evaluating its performance compared to a more traditional control methodology, likely a PID controller seen in literature.

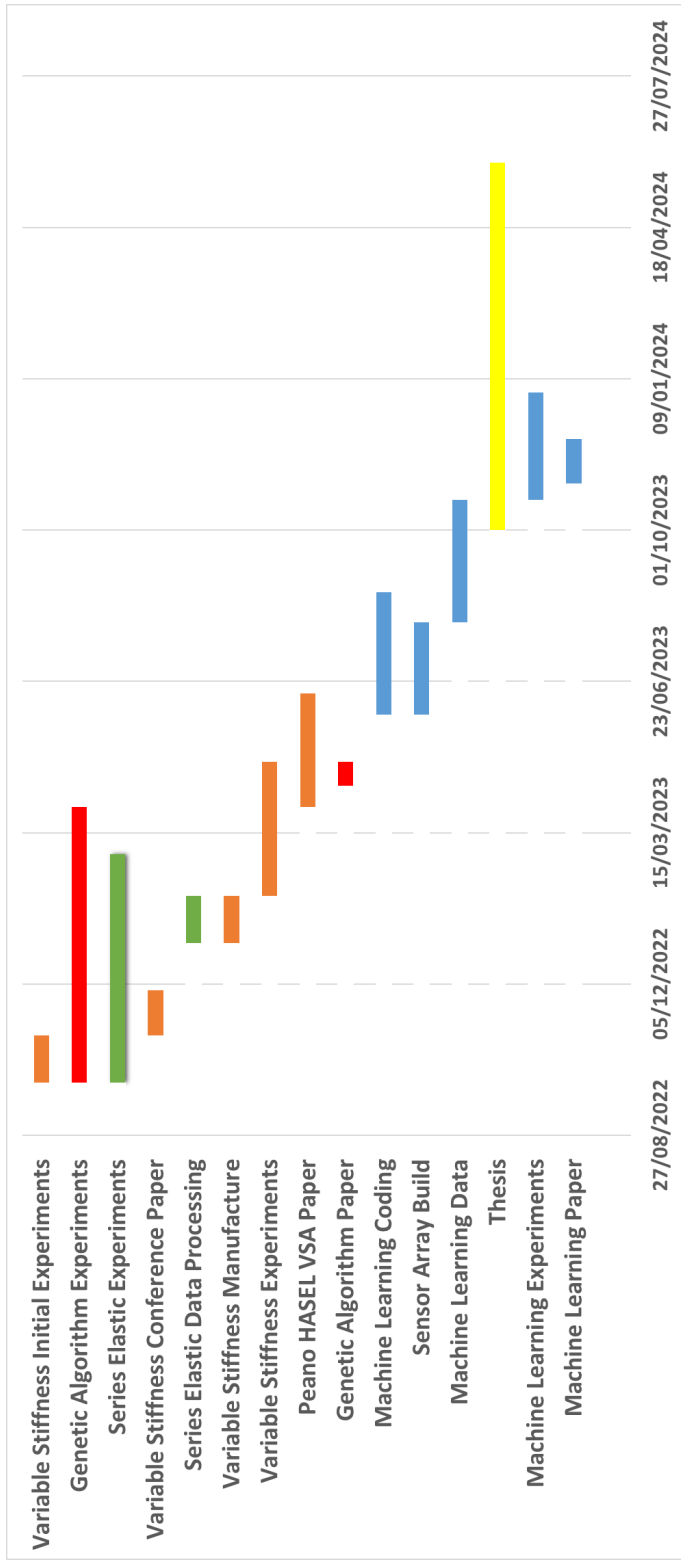


Figure 6.1: Gantt chart demonstrating future project workflow.

## 6.4 PH-VSA Work Packages

There are 15months available for research remaining, leaving 6 months afterwards as a writing up period. In order to realise the project aim, the following work packages need to be undertaken. Please note that the stretch goal exists on the condition that the PH-VSA is complete, otherwise that time will function as a buffer.

### 1: Silicone Couplings

#### **Timeframe: Oct 2022 - Dec 2022**

An immediate investigation to carry out is a study of the impact of curing time on silicone interfaces. This study will make small samples of two silicones with variable cure times between pours then mechanically test them to understand the impact on interface strength. This will be carried out in the coming weeks.

The study of roots will continue with an investigation into a clamping methodology aswell. The strength of these interfaces with the SEE under tension need to be explored, as well as the variables which alter this interaction.

### 2: Variable Siffness Principle Investigations

#### **Timeframe: Oct 2022 - Dec 2022**

Continuations of work carried out on investigating the impact of the pennate variable stiffness will be carried out as soon as material is available. The test will however be modified to use the PLA root methodology until curing is investigated, rather than the silicone binding, as the silicone tear off failure mode is an inconsistent detriment to acquiring useful results. The principle is the same in both cases so the investigation still appears potentially fruitful regardless of coupling method.

### 3.1: Peano-HASEL Force-Velocity Benchmarking

#### **Timeframe: Oct 2022 - Dec 2022**

Experiments using Peano-HASELs actuating loads without SEEs to provide Force-Velocity benchmarks to understand the magnitude of power modulation achieved through the introduction of an SEE. These experiments can be carried out in the next months with the production of samples and experimental rig completed.

### 3.2: Peano-HASEL Position-Time Benchmarking

#### **Timeframe: Oct 2022 - Dec 2022**

Similar to above but involving analysis of settle times to positional setpoints. This benchmark will allow for comparisons when introducing a SEE.

### 4.1: PH-SEA Force-Velocity Tests

#### **Timeframe: Dec 2022 - March 2023**

These tests will look to load the SEE while locked in place by a magnet to allow potential energy development in the SEE under loading from Peano-HASELs before release. This will characterise the power modulation capabilities of the PH-SEA and compare outputs to the benchmark.

## **4.2:PH-SEA Position-Time Tests**

### **Timeframe: Dec 2022 - March 2023**

Characterising the ability of the PH-SEA to achieve accurate positioning, including the dynamic response and settle times. Multiple set points in a single actuation cycle can be investigated to understand system hysteresis and response times. Varying the load on the actuator and tracking the motion of the load using a laser displacement sensor will provide displacement-time data that can be used to assess these metrics.

## **4.3:PH-SEA Power Modulation Tests**

### **Timeframe: Dec 2022 - March 2023**

Investigations of the power modulation capability of the PH-SEA will be conducted using a magnetic coupling and release mechanism to build SEE energy and then release this transiently. Changes in actuator loading will be used to characterise the force output of the PH-SEA and a laser displacement sensor will track the position of the load in time. Temporal force outputs and power data can then be used to investigate the power modulation. Again this forms part of the larger PH-SEA work.

## **5:Control Signals**

### **Timeframe: Oct 2022 - Jan 2022**

A simple investigation is the effect of different actuation signals on Peano-HASEL dynamics. This study will look at the mathematical nature of the actuation voltage function and look to understand the impact of this on the dynamic response in positioning tasks, observing changes in rise time, settle time, dynamic magnification. When the Peano-HASEL is expanded into a SEA,

## **6:Genetic Algorithm Investigations**

### **Timeframe: Oct 2022 - March 2023**

This work can run parallel to all of the above as it is computationally based. A optimised SEE can be produced in a number of days and installed onto the PH-SEA easily once couplings are finalised. Future work will look at understanding the impact on fitness gradients throughout generations of optimisation parameters and cost function metric weightings. Expanding the genetic algorithm to include the ability to attribute sections of an SEE different materials will be a line of immediate future work. Having access to both geometry and material properties would allow the optimisation scheme more degrees of freedom within which to search for optimal solutions. This will require coding an automated method to assign, mesh and accurately simulate multi material SEEs. However, this is dependant now on the results of the silicone interface study as it is critical to understand the nature of the interface if a multi-material SEE is to be physically realised. Validations will be carried out on results using mechanical testing. Optimised SEEs will be manufactured through 3D printer modular molds. The final tendon will be implemented on the PH-SEA and compared to original benchmark tests. This would be the first genetic optimisation of silicone springs to the authors knowledge and the first use of this approach to make a soft SEE for an SEA.

## **7.1:Pennate Peano-HASEL Actuators**

**Timeframe: Oct 2022 - March 2023**

The introduction of pennate PH actuators for the variable stiffness expansion of the PH-SEA will require production of HV power supplies or some method of regulating a large amplifier with electrical control, likely via optocouplers. Mounting of the pennate actuators will also require attention as it will be challenging to allow required movement while maintaining the pennate angle. This will be the first attempt at this methodology of achieving variable stiffness in a soft actuator.

## **7.2:Controllable Stiffness Variability Characterisation**

**Timeframe: Dec 2022 - June 2023**

Investigating the magnitude and controllability of the variable stiffness modifications will characterise the PH-VSA and repeats of the PH-SEA tests above will be undertaken with variable stiffness introduced. A particular line of inquiry is the ability of the PH-VSA to actively reduce vibrations of the SEE through pulsing of pennate actuators. This will hopefully be published as a conference paper.

## **8: Thesis**

**Timeframe: Oct 2023 - June 2024**

## **6.5 Stretch: Long-Short Term Memory Control and Sensing**

### **6.5.1 Proposed Approach**

It is possible that machine learning control schemes can compensate for the lack of sensory information and complexity of dynamics by using existing information to statistically infer required control inputs. Taking inspiration from the biomimetic principles, a Long-Short Term Memory (LSTM) approach has been conceptualised to achieve the open-loop control of the PH-VSA in a 1DOF system. The goal of the controller will be to achieve accurate positioning of the SEE's free end using proprioceptive sensory inputs from the Peano-HASEL's capacitive kinaesthesia and those inputs associated with SEE state. The LSTM architecture allows for interpretation of time series data in context. It is hypothesised this will mitigate and compensate for the non-linearity and potential hysteresis present in the PH-VSA system.

The VSA architecture proposed in this work in tandem with the LSTM controller could potentially solve the predicted problem of transient SEE vibrations by actively pulsing the actuators in order to cancel out these vibrations by active counter-forcing. This problem may be especially prevalent in force modulation modes where SEE recoil is predicted to be substantial.

The LSTM based control architecture requires a large data set in order to learn to control the PH-VSA system. This data needs to adequately cover the operating space with enough variability to allow for the network to accurately extrapolate to novel actuation scenarios. To gather this data, a "Babbling" approach will be employed in which a PH-VSA is actuated using near random signals. These signals will be generated by selecting a voltage stimulus paths and tracking the path taken by the SEE tip as well as sensory data. Hold times and approach gradients will be varied within bounds and also randomly scaled. This approach will need consideration in order to populate the data set with useful actuation cycles. An accurate dynamic analytical or multi-physics model of the

PH-VSA could also facilitate a digital twin approach that could contribute to this data collection with a fair weighting attributed to corresponding training trials to reflect the data's non-physicality.

The training regime also warrants considerable attention. Training will see the machine learning operate within a bounded environment in an attempt to match positions on a real world PH-VSA using only sensory inputs and the SEE tip path, producing voltage stimulus signals to meet this path. The cost function will include metrics such as energy expenditure and positional error. Novel tip paths will be generated to avoid data over fitting and demonstrate the ability of the controller to meet novel control demands.

The machine learning approach is designed to investigate the effectiveness of the methodology, not to provide a generalised control network that can be applied to any subsequent 1-DOF task without further training. Machine learning approaches are limited by their dataset and what the data capture. Any application would need to retrain networks to that specific application. A machine learning approach also sacrifices human interoperability, which may be detrimental to implementation when safety of the robot or interacting systems/humans is considered. However, if considerable accuracy on tasks can be demonstrated and the network bounded, a reasonable confidence can be established in a control scheme.

## Workpackages

**Stretch.1: Coding — Timeframe: June 2023 - August 2023** The LSTM will likely be written in Matlab with a Simulink interface to the physical apparatus. The cost function will need considerable attention to capture positional accuracy and power expenditure. This step also includes the design of the actuation cycles. These will likely be made in discrete chunks that can be chained together into different combinations. This will allow for hysteresis impacts and variability to be captured in the training data set while encoding desired or useful actuation patterns.

**Stretch.2: Magnetic SEE Sensing — Timeframe: June 2023 - August 2023** Integration of hall sensors into the sensing apparatus for an SEE could detect the change in magnetic field strength given by a magnet(s) embedded into the SEE. This would allow for data that can be related to actuation outputs by the LSTM.

**Stretch.3: Data Collection — Timeframe: August 2023 - Oct 2023** As discussed, data collection will take place with a babbling approach with multiple actuation cycles. Consideration to the nature of actuation cycles is important to allow the LSTM to generalise. Data will then be collected over the course of all actuation cycles. Likely each actuation cycle will be run multiple times in different sequences.

**Stretch.4: Experiments — Timeframe: Oct 2023 - December 2023** Physical Experiments will look to see if there is a non-negligible improvement in positional accuracy and energy expenditure when operating the PH-VSA. It is hypothesised that if these attributes are well captured in the cost function and the training data set has sufficient generalisability, then an improvement over conventional actuation would be observed. Experiments can also be carried out on the impact of LSTM variables such as network depth and width, attempting to determine optimum values for minimisation of computation cost while maintaining performance, important factors for onboard, *in situ* control.

## **Appendix A**

# **Experimental Setup**

## **Experimental Setup**

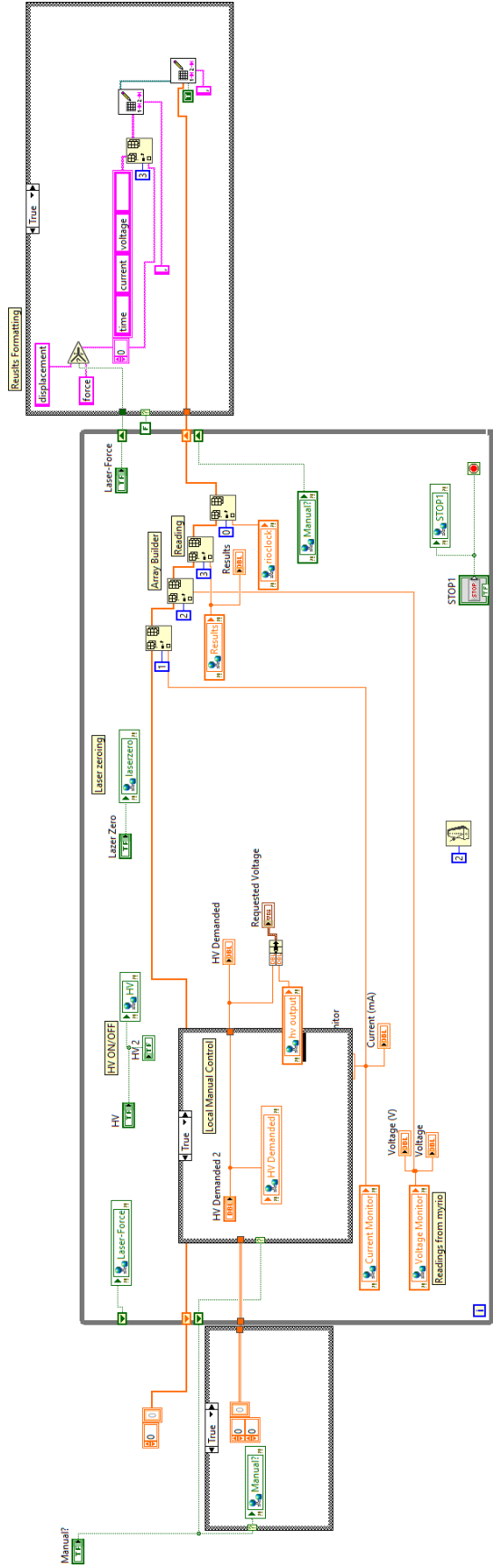


Figure A.1: Control Code on PC

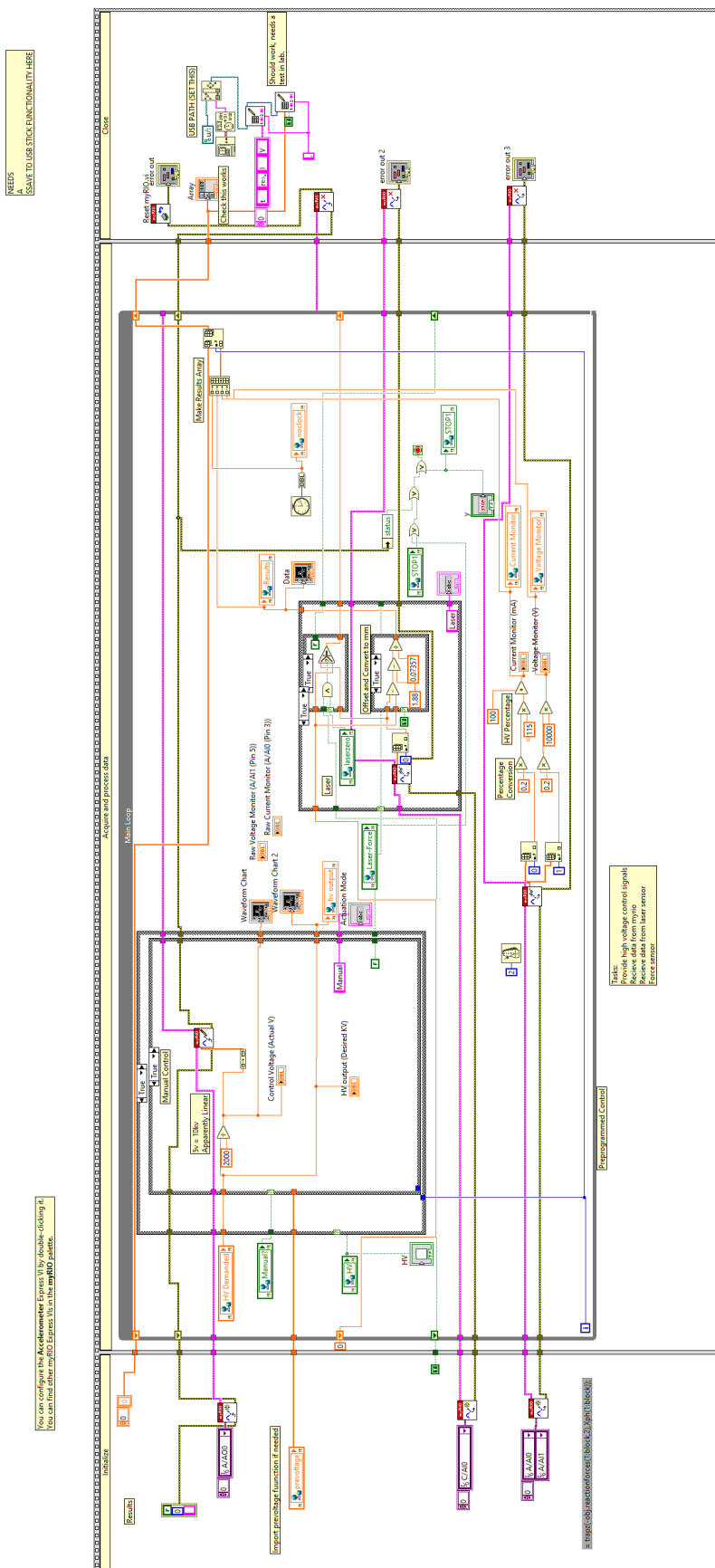


Figure A.2: MyRio Labview Code

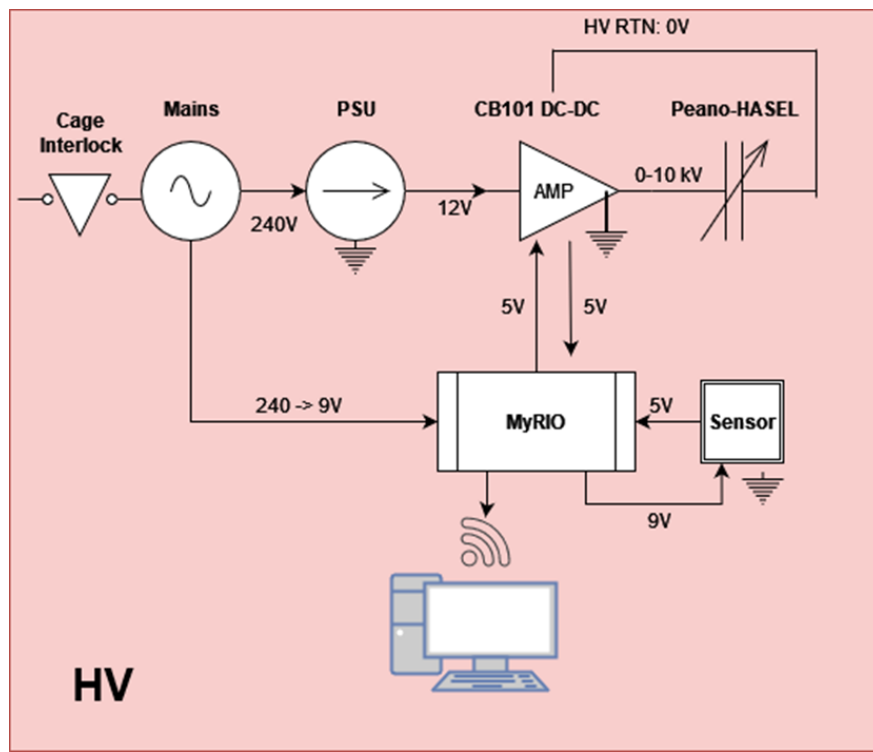


Figure A.3: Diagram of High voltage setup.

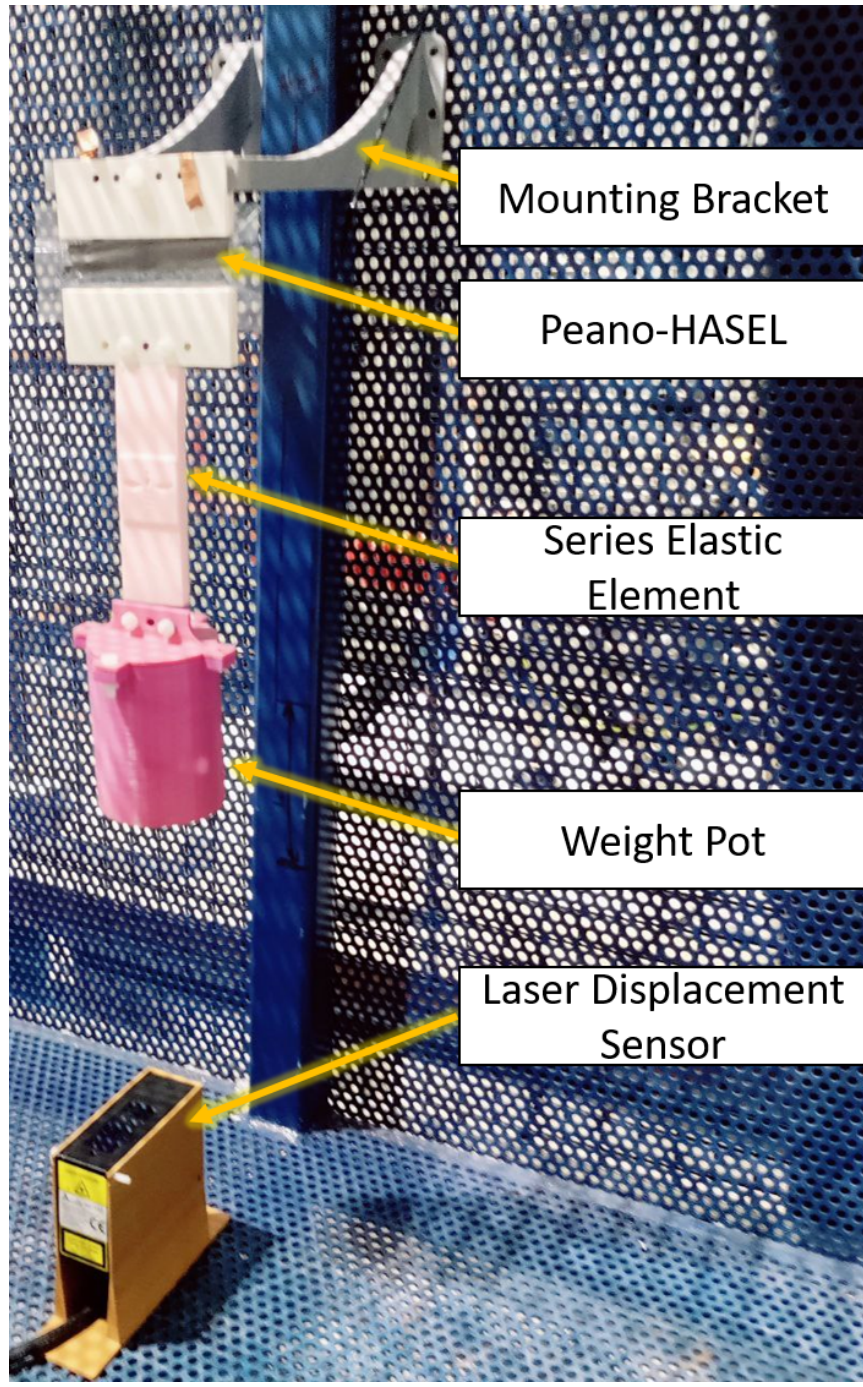


Figure A.4: Experimental setup for displacement readings in high voltage cage. The brakcet can be mouted at vvarying height using the holes in cage, allowing for any PH-SEA design.

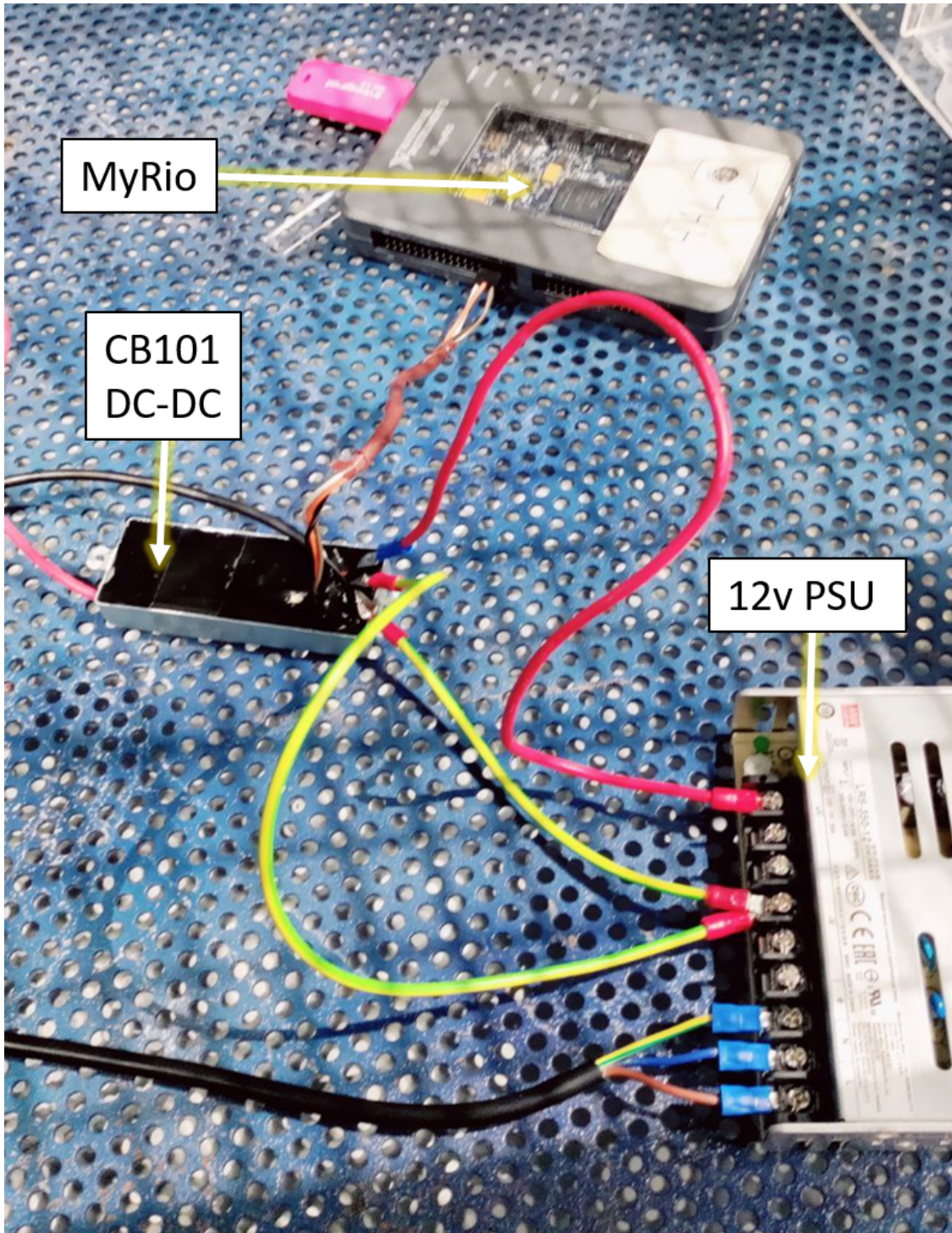


Figure A.5: Experimental circuit. The circuit can be left loose as the cage is interlocked and fully grounded, making exposed components safe. Data Acquisition is carried out by a MyRio controller and the PSU converts mains to 12v. The cb-101 is a DC-DC transformer that bumps a 12v signal into a 10kv. The CB101 is controllable with a 5v signal from the myrio and provides feedback through current and voltage monitors.

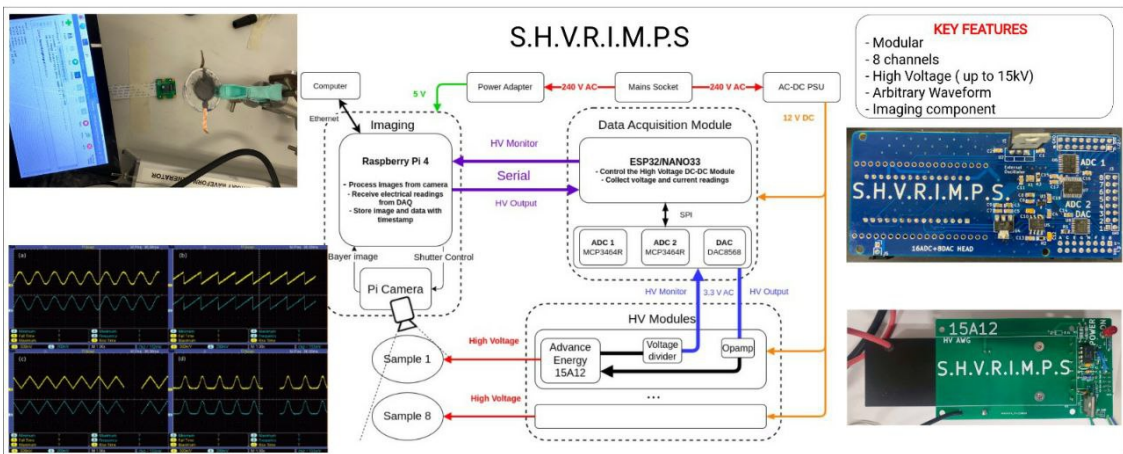


Figure A.6: Graphical abstract of SHVRIMPS system that will be loaned to this project to help complete multi-channel actuation in the PH-VSA

## Appendix B

### Matlab code

#### G-Code Generator

```
1      % PEANO HASEL GCDOE GEN
2 % Enter signature and other variables
3 % get actuator gcode
4
5 %% Signature
6
7 lp = 20; %mm pouch length
8 w = 80; % mm width
9 f = 0.6; % electrodle percentage coverage
10 g = 4; % mm gap width at +-0.5w
11 s = 40; % mm injection port lenght , g is width
12 taper = 0;
13 n = 6; % number of series acutators +1 for some reason
14 NN = 0; % number of single actuators in batch
15
16 filename = append(num2str(w), '_', num2str(lp), '_', num2str(n), '.gcode');
17 % — —
18 % | | bottom
19 %
20
21 % +(1-f)*lp needed for bucklers
22
23
24 %% NEED A HOME COORDINATE SO I CAN CHANGE THIS EASY
25 %% Initial file creation and header
26 % take from working files
27 gcode = fopen(filename, 'w');
28 fprintf(gcode, datestr(datetime('now')));
29 fprintf(gcode, '\n');
```

```

30 fprintf(gcode, ';Generated by yah boy, big up standardisation of file
31   formats\n');
32 fprintf(gcode, 'G21; mm\n');
33 fprintf(gcode, 'G0 Z8; z to safe\n');
34 fprintf(gcode, 'G0 X40 Y40\n'); % slap that boy to the origin
35 %% Main loop
36 % c = [w 0; %bottom
37 %     w+2 0.25*(lp-f*lp); w 0.5*(lp-f*lp); w+2 0.75*(lp-f*lp); w lp-f*
38 %         lp; %right triangle thing
39 %     w lp-g; w+s lp-g; w+s lp;% Fill port
40 %     0 lp; % top
41 %     0 lp-f*lp; -2 0.75*(lp-f*lp); 0 0.5*(lp-f*lp); -2 0.25*(lp-f*lp)
42 % ];
43 % c = flip(c);
44 c = [-2 0.25*(lp-f*lp); 0 0.5*(lp-f*lp); -2 0.75*(lp-f*lp); 0 lp-f*lp;
45     0 lp; w+s lp;%+w/3+s/2 lp; % top
46     w+s lp-g;%+w/3+s/2 lp-g; w+s+w/3 lp-g; w+s+w/3 0; w+s 0;
47     %w+s lp-g;
48     w lp-g;
49     w lp-f*lp; w+2 0.75*(lp-f*lp); w 0.5*(lp-f*lp); w+2 0.25*(lp-f*lp)
50     ; w 0; 0 0];
51 % All but bottom are missing c1
52 xbump = zeros(size(c), 'like', c);
53 c = c + (xbump(:, 1) + 40);
54 offset = zeros(size(c), 'like', c);
55 offset(:, 2) = offset(:, 2) + lp; % bump all y values
56 bigoffset = zeros(size(c), 'like', c);
57 bigoffset(:, 2) = bigoffset(:, 2) + lp * 2.5;
58 i = 0;
59 while i <= n
60     i = i + 1;
61     if i == n && i == 1 % case for single actuator
62
63         % draw points for closed bottom and injection port
64         fprintf(gcode, 'single\n\n');
65         %fprintf(gcode, 'G0 Z-0.2 X0 Y0\n');
66         fprintf(gcode, 'G1 Z-0.2 X40 Y40');
67         for NN = drange(0, NN)
68             %fprintf(gcode, 'G1 F50 X%.7g Y%.7g\n', c(1,:)); % draw
69             % bottom line
70             gcode = buckler(gcode, f, lp, c(1, :), 1); % make a right
71             buckler
72             fprintf(gcode, 'G0 X%.7g Y%.7g\n', [40 40+lp*2.5*NN]);
73             fprintf(gcode, 'G1 Z-0.2');
74             fprintf(gcode, 'G0 X%.7g Y%.7g\n', [40 40+lp*2.5*NN]);
75             for j = drange(1, 6)
76                 fprintf(gcode, 'G1 F50 X%.7g Y%.7g\n', c(j, :));

```

```

72      end
73      fprintf(gcode , 'G0 Z8\n') ; % up
74      fprintf(gcode , 'G0 X%.7g Y%.7g\n' , c(7,:)) ; %over gap
75      fprintf(gcode , 'G0 Z-0.2\n') ; %back down
76      for j = drange(8,14)%18)
77          fprintf(gcode , 'G1 F50 X%.7g Y%.7g\n' ,c(j,:));
78      end
79      c = c+bigoffset;
80      fprintf(gcode , 'G0 Z8\n') ; % up
81      fprintf(gcode , 'G0 F50 X%.7g Y%.7g\n' ,[0 0+lp *2.5*NN]) ;
82  end

83
84      fprintf(gcode , 'G0 Z8\n') ; % up
85      break
86      % Finished
87 elseif i ~= n && i==1% case for bottom
88     % draw close bottom box with gap
89     % draw points for closed bottom and injection port
90     % draw points for closed bottom and injection port
91     fprintf(gcode , ';'bottom\n\n');
92     fprintf(gcode , 'G0 Z-0.2 X40 Y40\n');
93     fprintf(gcode , 'G1 Z-0.2 X40 Y40\n');
94     fprintf(gcode , 'G1 F50 X%.7g Y%.7g\n' ,c(1,:)); % draw bottom
95     line
96     % gcode = buckler(gcode,f,lp,c(1,:),1); % make a right buckler
97     for j = drange(1,6)
98         fprintf(gcode , 'G1 F50 X%.7g Y%.7g\n' ,c(j,:));
99     end
100    fprintf(gcode , 'G0 Z8\n') ; % up
101    fprintf(gcode , 'G0 X%.7g Y%.7g\n' , c(7,:)); %over gap
102    fprintf(gcode , 'G0 Z-0.2\n') ; %back down
103    for j = drange(8,14)%18)
104        fprintf(gcode , 'G1 F50 X%.7g Y%.7g\n' ,c(j,:));
105    end
106    fprintf(gcode , 'G0 Z8\n') ; % up
107    fprintf(gcode , 'G0 F50 X%.7g Y%.7g\n' ,c(5,:)); %new origin

108 else % mids
109     % draw top "L's" w/ gap
110     % currently at [w,(i-1)*lp] from last run
111     % draw close bottom box with gap
112     % draw points for closed bottom and injection port
113     % draw points for closed bottom and injection port

114     fprintf(gcode , 'mid\n\n');
115     c = c + offset;
116     fprintf(gcode , 'G0 Z-0.2\n') ; %back down

```

```

118      %fprintf(gcode , 'G1 F50 X%.7g Y%.7g\n' ,c(1,:)); % draw bottom
119      % line
120      gcode = buckler(gcode ,f ,lp ,c(1,:),1); % make a right buckler
121      for j = drange(1,6)
122          fprintf(gcode , 'G1 F50 X%.7g Y%.7g\n' ,c(j,:));
123          fprintf(gcode , 'G0 Z8\n'); % up
124          fprintf(gcode , 'G0 X%.7g Y%.7g\n' , c(7,:)); %over gap
125          fprintf(gcode , 'G0 Z-0.2\n'); %back down
126          for j = drange(8,13)%18)
127              fprintf(gcode , 'G1 F50 X%.7g Y%.7g\n' ,c(j,:));
128          end
129          fprintf(gcode , 'G0 Z8\n'); % up
130          fprintf(gcode , 'G0 F50 X%.7g Y%.7g\n' ,c(5,:)); %new origin
131      end
132  end
133  %gcode = circles(gcode ,true ,w,lp ,n);
134  %gcode = circles(gcode ,false ,w,lp ,n);
135
136 %% End
137  fprintf(gcode , 'G0 Z20; z to safe\n');
138  fprintf(gcode , 'G0 X100 Y100\n'); % slap that boy to the origin
139  fclose(gcode);
140
141
142 %% Circle function
143  function gcode = circles(gcode ,bottom ,w,lp ,n)
144      seperation = 10; % seperation between holes mm
145      co_circle_number = 4; %number of co-centric circles
146      line_circle_number = 5;
147      distance = 10;
148      reso = 20; % circle divisions
149      inc = 0.5; % Incremenet of circle radius
150
151      fprintf(gcode , 'G0 Z8\n'); % up
152      x = 0.5*w - floor(line_circle_number)*seperation + 40; % start on
153          % furthest left
154      if bottom == true
155          yy = -distance +40; % Start at centre of inner most circle
156      else
157          yy = lp*(n) + distance +40; % Start at centre of inner most
158          % circle
159      end
160      fprintf(gcode , 'G0 X%.7g Y%.7g\n' , [x,yy]); % go there
161      for k = 1:line_circle_number
162          % Start left , add seperation each time
163          %fprintf(gcode , 'G91'); % switch to relative

```

```

163     centre = [40+ 0.5*(w)-floor(line_circle_number/2)*seperation+(k
164         -1)*seperation , yy];
165     fprintf(gcode , 'G0 X%.7g Y%.7g\n' , centre); % hover over centre
166     for j = 1:co_circle_number
167         % start in middle , go outwards
168         radius = 6/2 + inc*(j-1); % M4 clearance
169         angle = 0.0;
170         step = (2*pi)/reso;
171         fprintf(gcode , 'G0 X%.7g Y%.7g\n' , (centre + [radius ,0])); %
172             first point is on right of centre
173         fprintf(gcode , 'G0 Z-0.2\n'); %back down
174         for i = 1:reso
175             % increment around circle
176             angle = angle + step;
177             x = radius* cos(angle);
178             y = radius* sin(angle);
179             fprintf(gcode , 'G0 X%.7g Y%.7g\n' , (centre + [x,y]));
180             %angle = angle + step;
181
182         end
183     end
184 end

```

## Numerical Code for PH Analytical Model

```

1      %% 2022 Series and Parallel PH Model
2  % Derived from Kellaris et al (2019)
3  %% Model Constants
4  Lp = 0.02; % [m] Initial Pouch Length – From original kellaris paper
        (2018)
5  perm0 = 8.85418782e-12; %[m-3kg-1s4A2]
6  permr = 2.2; % for BOPP
7  Eb = 700e6;%#[V/m] the breakdown strength of BOPP
8  w = 0.08; %[m] from original kellaris paper
9  t = 30e-6; %[m] Bopp thickness used in initial designs
10 %k = 1000000; %[Nm-1] Achilles tendon average sourced from Litchwark
        2005
11 rho_f = 903; %[kgm-3] Bopp Density TEKRA (2020)
12 rho_o = 920; %[kgm-3] FR3 Dielectric oil Density Cargill (2018)
13 alpf = pi/2; % #[rad] Assume circular cross section on stroke
        completion
14 Eper = 0.6; % Percentage of electrode coverage
15 Va = 7500; % Actuation voltage
16 N = 5; % parallel actuators

```

```

17 nn = 7; % series actuators
18 res = 1000;
19
20 %% Swept constants
21 %Va = linspace(0,10000,1000) % 0 -> 10kV res: 10V
22 E = Va/(2*t);
23 %Eper = np.linspace(0,1,0.01)
24
25 %# model start
26 %Lambda for force
27 lamb = N*Va^2*perm0*permr*w/(4*t);
28
29 % Electrode length
30 Le = Lp*Eper;
31
32 % optimal fill eqn based on electrode coverage ratio
33 % !!! MIGHT NOT WORK WITH ARRAY !!!
34 alpeqn = ((1-Eper)^2)*(2/pi); % Easy to calc constant
35 y = 0.01; % intial guess of angle
36 it = 0.0001; % iteration
37 scale = 1.6/it; % how many possible
38 eend = scale; % int for loop
39 i = 0;
40 while i < eend % over scale
41
42     func = (y-sin(y)*cos(y))/(y^2) - alpeqn; % Find value of remaining
        equation with embedded alpha0
43
44     if func >= 0 % root is transition from negative to positive in this
        case
        alp0 = y - it; % previous value before sign flip returned
        break %root found, stop
45     else
46         y = y + it; %move to next guess
47         i = i + 1;
48         continue
49     end
50 end
51
52 %Height
53 h = Lp*(sin(alp0)/alp0); % Height [m]
54
55 %Area w/ restraints
56 % !!! MIGHT NOT WORK WITH ARRAY !!!
57 A = (Lp - Le)^2 / pi; % Area [m2]
58
59 %Fill Volume
60 Vol = A*w;

```

```

63
64 Fb = lamb*(cos(alp0)/(1-cos(alp0))); % Blockign Force
65
66 Lpf = Lp - Le; % Fully deformed pouh length
67
68 xmax = h - (Lpf*sin(alpf)/alpf) - Le; % Max possible displacement
       assssuming circular profile
69
70 alp = linspace(alp0,alpf,res);
71
72 % Dumb workaround incoming...
73 lpnum = 2.*A.*alp.^2;
74 lpd़om = (alp - sin(alp).*cos(alp));
75 lp2 = lpnum./lpdom;
76 lp = lp2.^0.5;
77 lp(1) = Lp;
78
79 le = Lp - lp;
80
81 lpmp = sin(alp)./alp;
82 lplpmp = lp.*lpmp;
83 X = h - lplpmp - le;
84
85 % Single actuator force response
86 F = lamb.* (cos(alp)./(1-cos(alp)));
87
88 % Series response calc (assumes all series actuators are equivalent)
89 globalx = X;
90 xseries = zeros(nn,res); % Storage for extra series displacements
91 mass = zeros(nn,res); % Effective mass
92
93 plot(X*1000,F)
94 xlabel('Displacement [mm]')
95 ylabel('Force [N]')
96 title('Increasing Number of PH-sarcs, n, in Fibre')
97
98 hold on
99 for n = drange(1,nn) % Sum contributions of series actuators
100    addload = (n-1)*9.81*(Vol*rho_o+Lp*w*t*2*rho_f);
101    for i = drange(1,length(F))
102        mass(n,i) = F(i) + addload;
103
104        if mass(n,i) >= Fb
105            continue
106        else
107            j = 1;
108            while j < length(F)
109                if F(j) <= mass(n,i)

```

```

110         xseries(n,i) = X(j);
111         break
112     else
113         j = j+1;
114     end
115     continue
116 end
117 end
118 end
119 X = sum(xseries,1);
120 X(X==0) = NaN;
121 F(F == 0) = NaN;
122 plot(X(1,1:end-1)*1000,F(1,1:end-1))
123 end
124 %legend('n=1','n=2','n=3','n=4','n=5','n=6','n=7','location','best')
125 hold off
126 % FOR GA SIMS
127 fph = F;
128 Xph = X;

```

## Genetic Algorithm

### High Level Operation

```

1 %% Genetic Algorithm
2 % TO DO
3 % [-] Cost Function
4 % [x] Initial Pop
5 % [x] stochastic selection
6 % [x] Genetic Algo events
7 % [x] Mutation
8 % [x] Crossover
9 % [x] Elitism
10 % [x] Link to geogen
11 % [x] Peano-HASEL model
12 % [x] IS BUSTED - fix
13 % [x] Write major loop
14 % [x] Test - did ---- all
15 % [x] Check that the see sim starts from previous displacement each
     time, I
16 % dont think it does!!!! (it does)
17 % [] E equation surface
18 % [x] big sweep
19 % [] multimaterial mod
20 % [] test
21 %% Setup

```

```

22 clear
23 clc
24 close
25
26 %% Global problem definitions [EVERYTHING IN M]
27
28 res = 1000;
29
30 % These will be defined here and PASSED to geo gen.
31 L = 0.08; % Length Tendon [m]
32 thickness = 0.01; % thickness of "2d" [m]
33 n = 20; % No. vectors per fan
34 m = 30; % No. Fans
35 r = 0; % No. Interstitial Vectors
36
37 E = 20; % 20shore.
38 nu = 0.45; % Poisson - dimless -> 0.33 incase
39 rho = 1080; % Density - kg/m3
40
41 pop_size = 20; % Number of individuals
42 pooln = 100; %Number of elements in mating pool. Divided up
    probabilistically (actual will have ± 1% or 2% from rounding)
43 elite_per = 0.1; % Percentage of seeds for elitism
44
45 a1 = 1; % Efficiency Cost Coefficient
46 a2 = 1; % Volume Cost Coefficient
47 gens = 10;
48 twoD = true; % T -> 2D POP | F -> 3D POP
49 %% Constraints
50 %% Bounding Cylinder
51 boundup = 0.025; % radius of bounding outer [m]
52 boundlw = 0.005; % radius of bounding inner dimension
53 % Every element of w must be less than or equal to this!
54
55 %% Generate Initial Population
56
57 Pops = cell(gens,1);
58 Pops{1} = Population(L,n,m,r,boundup,boundlw,E,nu,rho,pop_size,pooln,
    elite_per,a1,a2,thickness,twoD,res);
59 %Pop = Population(L,n,m,r,bound,E,nu,rho,pop_size,pooln,elite_per,a1,a2
    ,thickness,twoD);
60
61 %% %% Varying radii cylinder initial pop
62 % radi_step = (boundup - boundlw)/pop_size;
63 % for i = 1:length(Pops{1}.seeds)
64 %     Pops{1}.seeds(i).chromosome(:,1) = radi_step*i;
65 %     disp(Pops{1}.seeds(i).chromosome(:,1))
66 % end

```

```

67
68 %% Loop until fitness convergence or max generations reached
69
70 % Pops{1}.get_fit() % Pulls all zero fitness but necessary for loop
    start condition
71 fit_change_min = 0.1; %Big number to start loop
72 fit_change = 0;
73
74 j = 1; % COUNTER for POPS cell
75 while fit_change < fit_change_min && Pops{j}.gen < gens % While |
    fitness max _ i - fitness max _ i+1|/fitness max _i+1 < 0.01 (1%) or
    gen < gens
76
77 for i = (1:length(Pops{1}.seeds))
    i=i
    if twoD == true
        Pops{j}.seeds(i).Generate_Geometry_2d();
    else
        Pops{j}.seeds(i).Generate_Geometry_3d();
    end
    Pops{j}.seeds(i).Sim();
end
78
79 Pops{j}.get_vols();
80
81 Pops{j}.get_fit();
82 if j ~= 1
    fit_change = abs((max(Pops{j}.fits)-max(Pops{j-1}.fits))/max(
        Pops{j}.fits));
else
    fit_change = 0;
end
83
84 Pops{j+1} = Pops{j};
85 Pops{j+1}.Sort();
86 Pops{j+1}.make_crosspool();
87 Pops{j+1}.make_mutpool(); ;
88
89 % clone Pops(j) before doing operations to create next generation
90
91 Pops{j+1}.gen = j; % label pop with generation number
92 Pops{j+1}.id_update(); % update seed ids
93 % How many times?
94 for i = floor(pop_size/4)
    Pops{j+1}.crossover(); % perform crossover a few times
95
96 end
97 for i = floor(3*pop_size/4)
    Pops{j+1}.mutate(); % perform mutation a few times
98
99
100
101
102
103
104
105
106
107
108
109
110

```

```

111
112 end
113
114 j = j+1 % Move on
115 disp(fit_change < fit_change_min)
116 disp(Pops{j}.gen < gens)
117 disp(fit_change < fit_change_min || Pops{j}.gen < gens)
118
119 end

```

## Population Object

```

1 classdef Population < handle
2
3 properties
4     L % Every Tendon has same length
5     n % no vectors per fan
6     m % How many fans
7     r % intstitial vectors
8     boundup % Boundary radius size
9     boundlw
10    pop_size % size of population
11    seeds = Seed.empty; % list of individuals in population
12    seeds_sorted;
13    elite_per;
14    pooln % size of mating pool
15    poolcross % cross mating pool
16    poolmut % mutation pool
17    gen % generation
18    vols % list of all individual volumes
19    volmean % current generation mean volume
20    effs % list of efficiencies
21    fits % list of costs
22    a1 % Fitness energy scaling param
23    a2 % Fitness mass scaling param
24    fitnorm % list of fitnorms
25    thickness
26    E % Youngs
27    nu % Poissons
28    rho % Mat Density
29    twoD % T -> 2D POP | F -> 3D POP
30
31 methods
32     function obj = Population(L,n,m,r,boundup,boundlw,E,nu,rho,
33                                pop_size, pooln, elite_per, a1, a2, thickness, twoD, res) %
34         % [Constructor] LET THERE BE LIFE
35         obj.a1 = a1;

```

```

34     obj.a2 = a2;
35     obj.gen = 0;
36     obj.fits = zeros(obj.pop_size,1);
37     obj.L = L;
38     obj.n = n;
39     obj.m = m;
40     obj.r = r;
41     obj.E = E;
42     obj.rho = rho;
43     obj.nu = nu;
44     obj.boundup = boundup;
45     obj.boundlw = boundlw;
46     obj.pooln = pooln;
47     obj.pop_size = pop_size;
48     obj.elite_per = elite_per;
49     obj.thickness = thickness;
50     obj.twoD = twoD;
51     for k = 1:obj.pop_size
52         obj.seeds(k) = Seed(obj.L,obj.r,obj.n,obj.m,obj.boundup
53                               ,obj.boundlw,obj.a1,obj.a2,obj.thickness,obj.E,obj.
54                               nu,obj.rho,twoD,res); % Inits all seeds
55         obj.seeds(k).id = [k, obj.gen]; % id
56         obj.seeds(k).gen = obj.gen;
57         obj.seeds(k).fit = 0;
58         Pop.seeds(k).Generate_Geometry()
59     end
60     for i = 1:obj.pop_size
61         obj.fits(i) = obj.seeds(i).fit;
62     end
63
64     function obj = id_update(obj)
65         for k = 1:obj.pop_size
66             obj.seeds(k).id = [k, obj.gen];
67         end
68     end
69
70     function obj = get_fit(obj) % creates array of all costs
71         for i = 1:obj.pop_size
72             obj.seeds(i).Fit();
73             obj.fits(i) = obj.seeds(i).fit;
74         end
75         obj.fitnorm = obj.fits/sum(obj.fits);
76     end
77
78     function obj = Sort(obj) % Orders seeds by cost so that mating
79     pools can be built
80     [~, ind] = sort([obj.seeds.fit]);

```

```

79         obj.seeds_sorted = obj.seeds(ind);
80     end
81
82     function Generate_Geometry_2D(obj) % Generates 2d geometry for
83         all seeds
84         for i = 1:obj.pop_size
85             obj.seeds(i).Generate_Geometry_2d();
86         end
87     end
88
89     function Generate_Geometry_3D(obj) % Generates 3d geometry for
90         all seeds
91
92         for i = 1:obj.pop_size
93             obj.seeds(i).Generate_Geometry_3d();
94         end
95
96     function Sim(obj)
97         for i = 1:obj.pop_size
98             obj.seeds(i).Sim()
99         end
100    end
101
102    function obj = make_crosspool(obj) % Crosspool – Better fitness
103        has more chance.
104        obj.poolcross = int16.empty;
105        start = ceil(length(obj.seeds)*obj.elite_per);
106        for k = start:obj.pop_size %for each individual w/o elites
107            for j = drange(1,round(obj.fitnorm(k)*obj.pooln)) %
108                place a probabilistically weighted amount into the
109                mating pool
110                obj.poolcross(end+1,1) = k; % adds the index to the
111                pool
112            end
113        end
114    end
115
116    function obj = make_mutpool(obj) % Mutation Pool – Worse has
117        more chance
118        obj.poolmut = int16.empty;
119
120        inversecost = (ones(length(obj.fitnorm),1) – obj.fitnorm)/(
121            obj.pop_size – 1);
122        start = ceil(length(obj.seeds)*obj.elite_per);
123        %% This loop is now more likely to select low fitness
124        %% individuals

```

```

119    for k = drange(start,obj.pop_size) %for each individual
120        for j = drange(1,round(inversecost*obj.pooln)) % place
121            an inverse probabilistically weighted amount into
122            the mating pool
123            obj.poolmut(end+1,1) = k; % adds the index to the
124            pool
125        end
126    end
127
128    function obj = get_vols(obj)
129        for i = 1:obj.pop_size
130            obj.vols(i) = obj.seeds(i).V;
131        end
132        obj.volmean = sum(obj.vols)/obj.pop_size;
133        for i = 1:obj.pop_size
134            obj.seeds(i).Vm = obj.volmean;
135        end
136    end
137
138    function obj = crossover(obj)
139        mates = zeros(2);
140        while mates(1) == mates(2)
141            mates = obj.poolcross(randi([1,length(obj.poolcross)
142                ],1,2));
143        end
144        mate1 = obj.seeds(mates(1)).chromosome;
145        mate2 = obj.seeds(mates(2)).chromosome;
146        i = 0;
147        cross = 0;
148        while i == 0
149            if obj.twoD == false % Changes crossover if twoD mode
150                is in/activated
151                if cross < 1 % Negative check
152                    cross = round(normrnd((length(obj.seeds(1)).
153                        chromosome)/2),(length(obj.seeds(1).
154                        chromosome)/6));
155                elseif cross > obj.n*obj.m % Chromosome bound check
156                    cross = round(normrnd((length(obj.seeds(1)).
157                        chromosome)/2),(length(obj.seeds(1).
158                        chromosome)/6)));
159                else
160                    i = 1;
161                end
162            else
163                if cross < 1 % Negative check
164                    cross = round(normrnd((obj.m/2),(obj.m/4)));
165                elseif cross > obj.n*obj.m % Chromosome bound check
166
```

```

158         cross = round(normrnd((obj.m/2),(obj.m/4)));
159     else
160         i = 1;
161     end
162 end
163 %% Make sub arrays and substitute into mates
164 %% Sub arrays
165 ovum1 = mate1(1:cross); % make sub upto cross
166 ovum2 = mate2(1:cross); % make sub from cross
167 mate2(1:cross) = ovum1; % sub into mate2
168 mate1(1:cross) = ovum2; % sub into mate1
169 obj.seeds(mates(1)).chromosome = mate1; % Introduce the
170     baby to the population , awww
171 obj.seeds(mates(2)).chromosome = mate2;%
172
173 end % Crossover with normal dist cross points
174
175 function obj = mutate(obj)
176     muti = obj.poolmut(randi([1,length(obj.poolmut)])); % index
177         for mutation is randomly selected from the pool
178     mut = obj.seeds(muti).chromosome; %
179     for i = 1:length(mut)
180         sigma = abs(obj.boundup-mut(i))/6; % Stanard deviation
181             is 0.25 distance to bound. Norm dist drops off about
182             4sig from mean
183         mut(i) = abs(normrnd(mut(i),sigma)); %
184         check = 0;
185         while check == 0
186             if mut(i) <= obj.boundlw
187                 mut(i) = abs(normrnd((obj.boundup - obj.boundlw)/2,(obj.boundup - obj.boundlw)/6)); %
188             elseif mut(i) >= obj.boundup
189                 mut(i) = abs(normrnd((obj.boundup - obj.boundlw)/2,(obj.boundup - obj.boundlw)/6));
190             else
191                 check = 1;
192             end
193         end
194         % scramble - two seperate operations?
195         %muti = obj.poolmut(randi(length(obj.poolmut)));
196         mut(randperm(length(mut)));
197         obj.seeds(muti).chromosome = mut;
198     end % Mutation operations bump and scramble | Currently
          combines

```

```

199
200     end
201
202 end

```

## Seed Object

```

1
2     classdef Seed < handle
3     % Tendon seed is part of population
4     % They are used to grow tendons from a chromosome
5     properties
6         % Properties
7         r
8         L
9         n
10        m
11        boundup
12        boundlw
13        chromosome % array or weights for scaling
14        E % Youngs
15        nu % Poissons
16        rho % Mat Density
17        thickness
18
19     % obj. identification
20     id
21     fname % name of stl
22
23     % Attributes
24     fit % fitness of seed
25     V % volume
26     Vm % mean volume of current gen
27     Usee % Energy stored in tendon
28     Uact % Energy created till block by Ph
29     eff % efficiency
30     Rs
31     % Other
32     a1
33     a2
34     geometry % STL?
35     rf % sim reaction strcture
36     reactionforces % simreaction forces
37
38     res
39     xx
40 end

```

```

41 methods
42     function obj = Seed(L,r,n,m,boundup,boundlw,a1,a2,thickness,E,
43         nu,rho,twoD,res)
44         obj.res = res;
45         obj.a1 = a1;
46         obj.a2 = a2;
47         obj.n = n;
48         obj.m = m;
49         obj.L = L;
50         obj.r = r;
51         obj.E = E;
52         obj.nu = nu;
53         obj.rho = rho;
54         obj.boundup = boundup;
55         obj.boundlw = boundlw;
56         obj.thickness = thickness;
57         if twoD == true
58             obj.chromosome = (obj.boundlw + (obj.boundup - obj.
59                 boundlw).*rand(1,m))./1; %000;
60         else
61             obj.chromosome = (obj.boundlw + (obj.boundup - obj.
62                 boundlw).*rand(n*m,1))./1; %000;
63         end
64     end
65
66     function obj = Generate_Geometry_3d(obj) % [] Finished?
67         obj.fname = append(num2str(obj.id(2)), '_', num2str(obj.id(1)
68             ), '.stl');
69         W = reshape(obj.chromosome,[obj.n,obj.m]);
70         z = linspace(0,obj.L,obj.m); % Propogate unit vectors along
71         length
72         U = zeros(3,obj.m); % unit vectors at each z
73         W = movmean(movmean(W,4,1),4,2);
74         big = {};
75         for i = drange(1:obj.m)
76             U(1,i) = 1;
77             U(3,i) = z(i);
78         end
79
80         theta = 2*pi/obj.n;
81         P = zeros(3,obj.m,obj.n); % Point Cloud pre-interpolation
82         [dim x fans x vectors in fans]
83         M = obj.m+((obj.m-1)*obj.r); % Number of fans w/
84         interpolated
85         Q = zeros(3,(M*obj.n)); % Point Cloud post-interpolation
86         [dim x fans x vectors in fans]
87         P = zeros(3*obj.m,obj.n);
88         %% Vector scaling

```

```

81
82     for i = drange(1:obj.m) % fan
83         for j = drange(1:obj.n) % Vector in fan
84             w = [W(j,i) 0 0; 0 W(j,i) 0; 0 0 1];% diagonal
85                 weight matrix to scale unit vector
86             rot = [cos((j-1)*theta) sin((j-1)*theta) 0; -sin((j-1)*theta) cos((j-1)*theta) 0; 0 0 1]; % rotation matrix
87             u = w*U(:,i); % scaled u into jth vector
88             p = rot*u; % rotated jth vector into position
89             for k = drange(1:3)
90                 P(k+((i-1)*3),j) = p(k); %insert into P
91             end
92         end
93
94     %% Reshape p for graph
95
96     %pp = reshape(P,[3 ,m*n]);
97
98     %% Interpolation
99     %
100    % k = 1; % set 0 so first q input is a
101    % %Every vector fan in P, -1 is for not going past last
102    % fan as this will be the "cap" of the tendon (-)-()-
103    % for j = drange(1,obj.n) %Every vector in a fan
104    %     for i = drange(1,obj.m-1) %Every vector fan in P, -1
105    %         is for not going past last fan as this will be the "cap" of the
106    % tendon (-)-()-
107    %         a = P(:,i,j); %Set start vector as fan1
108    %         b = P(:,i+1,j); %set end vector as fan 2
109    %         equivalent
110    %         d = b-a;
111    %         %s = (1/(obj.r+1))*(P(3,i+1,j) - P(3,i,j)); %step
112    %         size
113    %
114    %         for ii = drange(0,obj.r+1) % sweep the line
115    %             between until hits next fan, placing vectors at regular intervals
116    %             along line
117    %             Q(:,k) = a + (ii/(obj.r+1))*d; %Place vector
118    %             at set intervals between a and b
119    %             %
120    %             k = k+1;
121    %             if ii == obj.r+1 && Q(3,k) ~= 100
122    %                 continue
123    %             else
124    %                 k = k+1;
125    %             end
126    %         end
127    %     end

```

```

118 % end
119 % Q(Q>-0.00005 & Q < 0.00005) = 0; % Smooth out numerical
120 error
121
122 P(P >-0.00005 & P < 0.00005) = 0;
123 PP = cell(obj.m,obj.n);
124 for i = drange(1:obj.m)
125     for j = drange(1:obj.n)
126         PP(i,j) = {P(1+((i-1)*3):3+((i-1)*3),j)};
127     end
128 end
129 %% Smoothing []
130 %% Need to go down tendon threads and smooth. Needs P rearranged
131 %% to do this.
132 %% P() = movmean(P,meanwind);
133
134 %% STL gen
135 %% Meshing
136 %% Meshing algorithm should draw regular triangles across the
137 %% tendon. Likely
138 %% sampling points to construct geometry completely
139 %% List in CCW direction so normal is out of geometry
140 %% STL = fopen(obj.fname,'w');
141 %% fprintf(STL, [ 'solobj.id ' obj.fname '\n' ]);
142
143
144
145 %% facet normal ni nj nk
146 %% outer loop
147 %%     vertex v1x v1y v1z
148 %%     vertex v2x v2y v2z
149 %%     vertex v3x v3y v3z
150 %% endloop
151 %% endfacet
152
153 %% 3D VERSION
154
155 %% TENDON IS IN BLOCKS
156 %% Z = 1 -> 2 []
157 %% []
158 %% []
159 %% Z = i-1 -> i []
160 %% Tendon blocks are built of many cyclic ordered points and are
161 %% referenced from the top
162

```

```

163 % STLalgo draws a block as so:
164 % n1 -> n2 -> n3
165 % NORMAL is defined by acw direction
166 % These rotate around a block
167 % o(TL) ——11———— o(TR)
168 % | | |
169 % 12 /13 /21 23
170 % | | |
171 % O(BL) ——22———— o(BR)

172
173 % Caps are defined differently
174 % no need to invert normals on 3d version
175
176 inv = 0;
177 STL = fopen(obj.fname, 'w');
178 fprintf(STL, [ 'solid ' obj.fname '\n']);
```

179

```

180 % Caps
181 % Bottom – Should be labelled face 1 and is fixed
182 for i = drange(1:obj.n)
183 idd = [num2str(1), 'cap', 'point', num2str(i)];
184 if i ~= obj.n
185     v1 = PP{1,i}';
186     v2 = [0,0,0];
187     v3 = PP{1,1+i}';%PP{1,i+2}'; %
188     big = stlwriter(STL,v1,v2,v3,inv,idd,big);
189 else
190     v1 = PP{1,i}';
191     v2 = [0,0,0];
192     v3 = PP{1,1}';%PP{1,i+2}'; %
193     big = stlwriter(STL,v1,v2,v3,inv,idd,big);
194 end
195 end
196 % Top – SHould be labelled face 2 and is loaded
197 for i = drange(1:obj.n)
198 idd = [num2str(2), 'cap', 'point', num2str(i)];
199 if i ~= obj.n
200     v1 = PP{end,i}';
201     v2 = [0,0,obj.L];
202     v3 = PP{end,i+1}';
203     big = stlwriter(STL,v1,v2,v3,inv,idd,big);
204 else
205     v1 = PP{end,i}';
206     v2 = [0,0,obj.L];
207     v3 = PP{end,1}';
208     big = stlwriter(STL,v1,v2,v3,inv,idd,big);
209 end
210 end
```

```

211
212 % Sobj .ides
213 for B = drange(1:obj.m-1) % For every block ie P(1:6,:)
214 for i = drange(1:obj.n) % For every point i+1 until returning
215 to 1
216 if i ~= obj.n
217     idd = [ num2str(1) , 'block' , num2str(B) , 'point' ,
218             num2str(i) ];
219     v1 = PP{B,i+1}';
220     v2 = PP{B,i}';
221     v3 = PP{B+1,i}';
222     big = stlwriter(STL,v1,v2,v3,inv,idd,big);
223
224     idd = [ num2str(2) , 'block' , num2str(B) , 'point' ,
225             num2str(i) ];
226     v1 = PP{B,i+1}';
227     v2 = PP{B+1,i}';
228     v3 = PP{B+1,i+1}';
229     big = stlwriter(STL,v1,v2,v3,inv,idd,big);
230
231 else
232     idd = [ num2str(1) , 'block' , num2str(B) , 'point' ,
233             num2str(i) ];
234     v1 = PP{B,1}';
235     v2 = PP{B,i}';
236     v3 = PP{B+1,i}';
237     big = stlwriter(STL,v1,v2,v3,inv,idd,big);
238
239 end
240 end
241 end
242
243 fprintf(STL,[ 'endsolid ' , obj.fname '\n']);
244 fclose(STL);
245 end
246
247 function obj = Generate_Geometry_2d(obj)
248
249     obj.fname = append(num2str(obj.id(2)) , '_' , num2str(obj.id(1)) , '_'
250                         , 'stl');
251 %r = 0; % No. Interstitial Vectors (GA)
252 z = linspace(0,obj.L,obj.m); % Propogate unit vectors along
length

```

```

252 zero = zeros(1,obj.m); % Bottom, tendon is made of two layers
253     sandwiched
254 meanwind = 3;
255 big = {};
256
257 smoothW = movmean(obj.chromosome,meanwind);
258 coordsssharp = cat(1,obj.chromosome,zero,z);
259 coordsssmoothR = cat(1,smoothW,zero,z);
260     % coordsssmoothL = cat(1,-smoothW,zero,z);
261 y = z;
262
263 plot3(coordsssharp(1,:),coordsssharp(2,:),coordsssharp(3,:));
264 hold on
265 plot3(coordsssmoothR(1,:),coordsssmoothR(2,:),coordsssmoothR(3,:))
266 ;
267 hold off
268
269 %% Stl Meshing
270 % Meshing algorithm should draw regular triangles across the
271 % tendon. Likely
272 % sampling points to construct geometry completely
273 % List in CCW direction so normal is out of geometry
274
275
276
277
278
279 % facet normal ni nj nk
280 %     outer loop
281 %         vertex v1x v1y v1z
282 %         vertex v2x v2y v2z
283 %         vertex v3x v3y v3z
284 %     endloop
285 % endfacet
286
287
288
289 % Loop 1 - Front x AND back x(thickness translation of
290 % coordiantes.)
291 % two in line vertices, one below or above.
292 % every value m will produce 4 triangles all from one point (
293 % left)
294
295 % create flat LR matrix [R (1,:) | L(2,:)]
296 x = cat(1,smoothW,-smoothW);

```

```

295
296
297
298 % 2DEEE VERSION
299
300 % TENDON IS IN BLOCKS
301 % y = 1 -> 2 []
302 % []
303 % []
304 %y = i-1 -> i []
305 % Tendon blocks are built of two lines and are
306 % referenced from the top
307
308 % STLalgo draws a block as so:
309 % n1 -> n2 -> n3
310 % NORMAL is defined by acw direction
311 % o(TL) ——11——— o(TR)
312 % | | |
313 % 12 /13 /21 23
314 % | | |
315 % O(BL) ——22—— o(BR)
316 %% Cap (Top) — ALWAYS F1
317
318 % !!! FACE LABELS ARE ASSIGNED IN GENERATION ORDER !!!
319
320 inv = 0; % Invert unit normal y/n?
321 % TR TL BL
322 idd = [ 'ct1' , 0];
323 v1 = [x(2,1) y(1,1) obj.thickness]; % from the TR point on
324 % block
325 v2 = [x(1,1) y(1,1) obj.thickness];
326 v3 = [x(1,1) y(1,1) 0];
327 big = stlwriter(STL,v1,v2,v3,inv,idd,big);
328 % TR BL BR
329 idd = [ 'ct2' , 0];
330 v1 = [x(2,1) y(1,1) obj.thickness]; % from the left point on
331 % the line
332 v2 = [x(1,1) y(1,1) 0];
333 v3 = [x(2,1) y(1,1) 0];
334 big = stlwriter(STL,v1,v2,v3,inv,idd,big);
335 %% Cap (Bottom) — ALWAYS F2
336 inv = 1;
337 % TR TL BL
338 idd = [ 'cb1' , 0];
339 v1 = [x(2,end) y(1,end) obj.thickness]; % from the TR point on
340 % block
341 v2 = [x(1,end) y(1,end) obj.thickness];
342 v3 = [x(1,end) y(1,end) 0];

```

```

340 big = stlwriter(STL,v1,v2,v3,inv,idd,big);
341 % TR BL BR
342 idd = [ 'cb2' , 0];
343 v1 = [x(2,end) y(1,end) obj.thickness]; % from the left point
344 % on the line
345 v2 = [x(1,end) y(1,end) 0];
346 v3 = [x(2,end) y(1,end) 0];
347 big = stlwriter(STL,v1,v2,v3,inv,idd,big);
348 %% Back
349 for i = drange(1,length(obj.chromosome)-1) % For each block
350 along length
351 inv = 1;
352 idd = [ 'B1' , num2str(i)];
353 % TR TL BL
354 v1 = [x(1,i) y(1,i) 0]; % from the TR point on block
355 v2 = [x(2,i) y(1,i) 0];
356 v3 = [x(2,i+1) y(1,i+1) 0];
357 big = stlwriter(STL,v1,v2,v3,inv,idd,big);
358 %% TR BL BR
359 idd = [ 'B2' , num2str(i)];
360 v1 = [x(1,i) y(1,i) 0]; % from the left point on the line
361 v2 = [x(2,i+1) y(1,i+1) 0];
362 v3 = [x(1,i+1) y(1,i+1) 0];
363 big = stlwriter(STL,v1,v2,v3,inv,idd,big);
364 end
365 %% Front
366 for i = drange(1,length(obj.chromosome)-1) % For each block
367 along length
368 inv = 0;
369 % TR TL BL
370 idd = [ 'F1' , num2str(i)];
371 v1 = [x(1,i) y(1,i) obj.thickness]; % from the TR point on
372 % block
373 v2 = [x(2,i) y(1,i) obj.thickness];
374 v3 = [x(2,i+1) y(1,i+1) obj.thickness];
375 big = stlwriter(STL,v1,v2,v3,inv,idd,big);
376 %% TR BL BR
377 idd = [ 'F2' , num2str(i)];
378 v1 = [x(1,i) y(1,i) obj.thickness]; % from the left point
379 % on the line
380 v2 = [x(2,i+1) y(1,i+1) obj.thickness];
381 v3 = [x(1,i+1) y(1,i+1) obj.thickness];
382 big = stlwriter(STL,v1,v2,v3,inv,idd,big);
383 end
384 %% SiddES
385 %% LEFT

```

```

383 for i = drange(1,length(obj.chromosome)-1) % For each block
384     along length
385     inv = 0;
386     % TR TL BL
387     idd = [ 'SL1' , num2str(i)];
388     v1 = [x(2,i+1) y(1,i+1) obj.thickness]; % from the TR point
389     on block
390     v2 = [x(2,i) y(1,i) obj.thickness];
391     v3 = [x(2,i) y(1,i) 0];
392     big = stlwriter(STL,v1,v2,v3,inv,idd,big);
393     % TR BL BR
394     idd = [ 'SL2' , num2str(i)];
395     v1 = [x(2,i+1) y(1,i+1) obj.thickness]; % from the left
396     point on the line
397     v2 = [x(2,i) y(1,i) 0];
398     v3 = [x(2,i+1) y(1,i+1) 0];
399     big = stlwriter(STL,v1,v2,v3,inv,idd,big);
400 end
401 %% Right
402 for i = drange(1,length(obj.chromosome)-1) % For each block
403     along length
404     inv = 1;
405     % TR TL BL
406     idd = [ 'SR1' , num2str(i)];
407     v1 = [x(1,i+1) y(1,i+1) obj.thickness]; % from the TR point
408     on block
409     v2 = [x(1,i) y(1,i) obj.thickness];
410     v3 = [x(1,i) y(1,i) 0];
411     big = stlwriter(STL,v1,v2,v3,inv,idd,big);
412     % TR BL BR
413     idd = [ 'SR2' , num2str(i)];
414     v1 = [x(1,i+1) y(1,i+1) obj.thickness]; % from the left
415     point on the line
416     v2 = [x(1,i) y(1,i) 0];
417     v3 = [x(1,i+1) y(1,i+1) 0];
418     big = stlwriter(STL,v1,v2,v3,inv,idd,big);
419 end
420
421 fprintf(STL,[ 'endsolid ' obj.fname '\n']);
422 fclose(STL);
423 % smodel = createpde('structural','static-solobj.id');
424 %
425 % importGeometry(smodel,'teest.stl');

```

```

425    % -OR-
426    %
427    % geomblock = multicubobj.id(1,1,3);
428    %
429    % smodel.Geometry = geomblock;
430
431
432
433
434
435    % Show model
436
437    % pdegplot(smodel,'FaceLabels','on','VertexLabels','on',...
438    % FaceAlpha',0.25);
439    end
440
441    function obj = Sim(obj)
442        %% Sim! [x] Fix infirun?
443
444        %% Peano Hasel define
445        Lp = 0.02; % [m] Initial Pouch Length – From original
446        % kellaris paper (2018)
447        perm0 = 8.85418782e-12; %[m–3kg–1s4A2]
448        permr = 2.2; % for BOPP
449        Eb = 700e6;%#[V/m] the breakdown strength of BOPP
450        w = 0.08; %[m] from original kellaris paper
451        t = 30e-6; %[m] Bopp thickness used in initial designs
452        %k = 1000000; %[Nm–1] Achilles tendon average sourced from
453        % Litchward 2005
454        rho_f = 903; %#[kgm–3] Bopp Density TEKRA (2020)
455        rho_o = 920; %#[kgm–3] FR3 Dielectric oil Density Cargill
456        % (2018)
457
458
459
460        [fph, Xph] = ph(Lp,w,Eper,perm0,permr,t,rho_f,rho_o,Va,N,nn
461        ,obj.res); % Pull Force/Disp of actuator
462
463        smodel = createpde('structural','static-solid');
464        importGeometry(smodel,obj.fname);
465
466        pdegplot(smodel,'FaceLabels','on','VertexLabels','off',...
467        'FaceAlpha',0.25);

```

```

467
468 % Pre-define rf
469 obj.rf = struct( 'Fx' ,0 , 'Fy' ,0 , 'Fz' ,0 );
470 obj.reactionforces = zeros( length(fph) ,3 );
471 for i = drange(1,length(fph)) % for all forces in fph
472 %disp(i)
473 err = 0.1; % 10%
474 meshsize = 0.1;
475 maxVM = 0; % initialise loop
476 conv = 1;
477 % Loop looks at max stress and waits till error
478 % converges
479 while conv > err
480 % MESHIN
481
482 msh = generateMesh(smodel , 'Hmax' ,meshsize , 'Hmin' ,
483 meshsize*0.01);
484
485 % Show model mesh
486
487
488 pdeplot3D(smodel)
489
490
491 % MATERIAL PROPERTIES
492
493 % Polyethylene Material – Big assumption silicone is
494 % linelastic
495 % obj.E = -1.995e5 * Xph(i) + 1.416e5; % Elastic Mod –
496 % Pa shore 20
497 % nu = obj.nu; % Poisson – dimless
498 % rho = obj.rho; % Density – kg/m3
499 structuralProperties(smodel , 'YoungsModulus' ,obj.E ,
500 'PoissonsRatio' ,obj.nu , 'MassDensity' ,obj.rho);
501
502 % BOUNDARY CONDITIONS
503
504 structuralBC(smodel , 'Face' ,2 , 'Constraint' , 'fixed' );
505
506 % PERTURBATIONS – [x] needs PH loading
507 % [x] Pull out face displacement
508 % [x] what is force ouput of PH here?
509 % [x] can the element deform further?
510 % [x] Is this auto captured in sim?
511
512 % Assign deformation conditions
513 % p1 = fph/(obj.thickness*x(1,1)^2);

```

```

510
511      % structuralBoundaryLoad(smodel,'Face',1,'pressure',p1)
512      ;
513
514      % Forces peano hasel tip displacement on the loaded
515      % face
516      structuralBC(smodel,'Face',1,'ZDisplacement',-Xph(i));
517
518      % SOLVE FEA
519
520      obj.Rs = solve(smodel);
521
522      % Mesh Convergence check
523      maxVMnew = max(obj.Rs.VonMisesStress);
524      conv = abs((maxVMnew-maxVM)/maxVM);
525      maxVM = maxVMnew;
526      meshsize = meshsize - 0.05*meshsize;
527
528      end
529
530      % Get reaction force to test block
531      obj.rf = evaluateReaction(obj.Rs,'Face',2);
532      obj.reactionforces(:, :) = [obj.rf.Fx, obj.rf.Fy, obj.rf
533      .Fz];
534
535      % Has block been found?
536      disp(obj.rf.Fz)
537      disp(fph(i))
538      if obj.rf.Fz > fph(i)
539          block = i;
540          break
541      else
542          continue
543      end
544
545      end
546      obj.V = msh.volume();
547      pdeplot3D(smodel,'ColorMapData',obj.Rs.VonMisesStress,
548      'Deformation',obj.Rs.Displacement,'DeformationScaleFactor
549      ',100);
550      obj.reactionforces(obj.reactionforces==0) = NaN;
551      obj.reactionforces(1,:) = 0;
552      plot(Xph,fph,Xph,obj.reactionforces(:,3))
553      obj.xx = Xph;
554
555      %% Strain energy - BROKEN??? VERY SMALL
556
557      % Volumetric strain energy [] BROKEN MAYBE???? Very small.

```

```

553 %  $Uv = E ./ (2 \cdot (1 + nu) \cdot (1 - 2 \cdot nu)) \cdot ((1 - nu) \cdot (exx.^2 + eyy.^2 + ezz.^2) + 2 \cdot nu \cdot (exx \cdot eyy + eyy \cdot ezz + ezz \cdot exx))$ 
554
555 % $Uv = obj.E ./ (2 \cdot (1 + obj.nu) \cdot (1 - 2 \cdot obj.nu)) \cdot ((1 - obj.nu) \cdot ((Rs.Strain.xx).^2 + (Rs.Strain.yy).^2 + (Rs.Strain.zz).^2) + 2 \cdot obj.nu \cdot (Rs.Strain.xx \cdot Rs.Strain.yy + Rs.Strain.yy \cdot Rs.Strain.zz + Rs.Strain.zz \cdot Rs.Strain.xx));$ 
556 %
557 %
558  $Uv = (1/2) \cdot (obj.Rs.Strain.xx \cdot obj.Rs.Stress.xx + obj.Rs.Strain.yy \cdot obj.Rs.Stress.yy + obj.Rs.Strain.zz \cdot obj.Rs.Stress.zz) + (obj.Rs.Stress.xy \cdot obj.Rs.Strain.xy + obj.Rs.Stress.yz \cdot obj.Rs.Strain.yz + obj.Rs.Stress.xz \cdot obj.Rs.Strain.xz);$ 
559
560 % $Ut = (1/(2 * obj.E)) \cdot (obj.Rs.Stress.xx.^2 + obj.Rs.Stress.yy.^2 + obj.Rs.Stress.zz.^2) - 2 \cdot obj.nu \cdot (obj.Rs.Stress.xx \cdot obj.Rs.Stress.yy + obj.Rs.Stress.xx \cdot obj.Rs.Stress.zz + obj.Rs.Stress.yy \cdot obj.Rs.Stress.zz);$ 
561 % Shear Strain energy (not sure if values I am using are correct)
562 % $Us = (obj.E / (4 \cdot (1 + obj.nu))) \cdot ((Rs.Strain.xy).^2 + (Rs.Strain.xz).^2 + (Rs.Strain.yz).^2);$ 
563
564 testuv = sum(Uv); % + sum(Us);
565
566 % ALT using reaction force (more accurate atm, possibly not
567 % getting everything)
568 obj.Usee = trapz(-obj.reactionforces(1:block,2),Xph(1:block));
569
570 %% Efficiency
571
572 % Peano_HASEL energy estimate up to block
573 obj.Uact = -trapz(fph(1:block),Xph(1:block));
574
575 obj.eff = abs(obj.Usee/obj.Uact);
576
577 end
578
579 function obj = Vol(obj)
580     obj.geometry = stlread(append(num2str(obj.id(2)), '_',
581                             num2str(obj.id(1)), '.stl'));
582     %[obj.V,Area] = stlVolume(obj.geometry.Points,obj.geometry.
583     %ConnectivityList); %broken
584     % !!! REMEMBER TO CITE THIS FUNCTION !!!
585 end

```

```

584
585     function obj = Fit(obj)
586         obj.fit = obj.a1.* (obj.Usee*obj.eff) + obj.a2.* (obj.Vm./obj
587             .V); % Big -> Better
588     end
589 end

```

## Peano-HASEL Function

```

1      function [fph , Xph] = ph(Lp,w,Eper,perm0,permr,t,rho_f,rho_o,Va,N,
2          nn,res)
3      %% 2022 Series and Parallel PH Model – Derived from Kellaris et al
4          (2019)
5
6      %% Model Constants –
7      % Lp = 0.02; % [m] Initial Pouch Length – From original kellaris
8      % paper (2018)
9      % perm0 = 8.85418782e-12; %[m-3kg-1s4A2]
10     % permr = 2.2; % for BOPP
11     % Eb = 700e6;%#[V/m] the breakdown strength of BOPP
12     % w = 0.12; %[m] from original kellaris paper
13     % t = 21e-6; %[m] Bopp thickness used in initial designs
14     % %k = 1000000; %[Nm-1] Achilles tendon average sourced from
15     % Litchmark 2005
16     % rho_f = 903; %[kgm-3] Bopp Density TEKRA (2020)
17     % rho_o = 920; %[kgm-3] FR3 Dielectric oil Density Cargill (2018)
18
19
20     alpf = pi/2; % #[rad] Assume circular cross section on stroke
21     completion
22
23     %% Swept constants
24     %Va = linspace(0,10000,1000) % 0 -> 10kV res: 10V
25     % E = Va/(2*t);
26     %Eper = np.linspace(0,1,0.01)
27
28     %% model start
29     %Lambda for force
30     lamb = Va^2*perm0*permr*w/(4*t);
31
32     % Electrode length

```

```

33 Le = Lp*Eper;
34
35 % optimal fill eqn based on electrode coverage ratio
36 % !!! MIGHT NOT WORK WITH ARRAY !!!
37 alpeqn = ((1-Eper)^2)*(2/pi); % Easy to calc constant
38 y = 0.01; % intial guess of angle
39 it = 0.0001; % iteration
40 scale = 1.6/it; % how many possible
41 eend = scale; % int for loop
42 i = 0;
43 while i < eend % over scale
44
45     func = (y-sin(y)*cos(y))/(y^2) - alpeqn; % Find value of
        remaining equation with embedded alpha0
46
47     if func >= 0 % root is transition from negative to positive in
        this case
        alp0 = y - it; % previous value before sign flip returned
        break %root found, stop
    else
        y = y + it; %move to next guess
        i = i + 1;
        continue
    end
end

56
57 %Height
58 h = Lp*(sin(alp0)/alp0); % Height [m]
59
60 %Area w/ restraints
61 % !!! MIGHT NOT WORK WITH ARRAY !!!
62 A = (Lp - Le)^2 / pi; % Area [m2] [] EDIT TO ALP0 EQN
63
64 %Fill Volume
65 Vol = A*w;
66
67 Fb = lamb*(cos(alp0)/(1-cos(alp0))); % Blockign Force
68
69 Lpf = Lp - Le; % Fully deformed pouh length
70
71 xmax = h - (Lpf*sin(alpf)/alpf) - Le; % Max possible displacement
        asssuming circular profile
72
73 alp = linspace(alp0,alpf,res);
74
75 % Dumb workaround incoming...
76 lpnum = 2.*A.*alp.^2;
77 lpdom = (alp - sin(alp).*cos(alp));

```

```

78 lp2 = lpnum./lpdom;
79 lp = lp2.^0.5;
80 lp(1) = Lp;
81
82 le = Lp - lp;
83
84 lpmp = sin(alp)./alp;
85 lplpmp = lp.*lpmp;
86 X = h - lplpmp - le;
87
88 % Single actuator force response
89 F = lamb.*cos(alp)./(1-cos(alp)));
90
91 % Series response calc (assumes all series actuators are equivalent
92 )
93 globalx = X;
94 xseries = zeros(nn,res); % Storage for extra series displacements
95 mass = zeros(nn,res); % Effective mass
96
97 for n = drange(1,nn) % Sum contributions of series actuators
98     addload = (n-1)*9.81*(Vol*rho_o+Lp*w*t*2*rho_f);
99     for i = drange(1,length(F))
100         mass(n,i) = F(i) + addload;
101
102         if mass(n,i) >= Fb
103             continue
104         else
105             j = 1;
106             while j < length(F)
107                 if F(j) <= mass(n,i)
108                     xseries(n,i) = X(j);
109                     break
110                 else
111                     j = j+1;
112                     end
113                     continue
114                 end
115             end
116         end
117 X = sum(xseries,1);
118
119 % FOR GA SIMS
120 fph = N*F;
121 Xph = X; % convert to mm

```

# Bibliography

- [1] E Acome, S K Mitchell, T G Morrissey, M B Emmett, C Benjamin, M King, M Radakovitz, and C Keplinger. Hydraulically amplified self-healing electrostatic actuators with muscle-like performance. *65*(January):61–65, 2018.
- [2] Peter Aerts. Vertical jumping in Galago senegalensis: The quest for an obligate mechanical power amplifier. *Philosophical Transactions of the Royal Society B: Biological Sciences*, 353(1375):1607–1620, 1998.
- [3] Haider A.F. Almurib, Haidar Fadhil Al-Qrimli, and Nandha Kumar. A review of application industrial robotic design. *International Conference on ICT and Knowledge Engineering*, pages 105–112, 2011.
- [4] Yiannis Ampatzidis, Luigi De Bellis, and Andrea Luvisi. iPathology: Robotic applications and management of plants and plant diseases. *Sustainability (Switzerland)*, 9(6):1–14, 2017.
- [5] Christopher J. Arellano, Nicolai Konow, Nicholas J. Gidmark, and Thomas J. Roberts. Evidence of a tunable biological spring: Elastic energy storage in aponeuroses varies with transverse strain in vivo. *Proceedings of the Royal Society B: Biological Sciences*, 286(1900):3–8, 2019.
- [6] Henry C. Astley and Thomas J. Roberts. The mechanics of elastic loading and recoil in anuran jumping. *Journal of Experimental Biology*, 217(24):4372–4378, 2014.
- [7] Jessica Austin, Alexander Schepelmann, and Hartmut Geyer. Control and evaluation of series elastic actuators with nonlinear rubber springs. *IEEE International Conference on Intelligent Robots and Systems*, 2015-Decem:6563–6568, 2015.
- [8] Emanuel Azizi and Thomas J. Roberts. Bi-axial strain and variable stiffness in aponeuroses. *Journal of Physiology*, 587(17):4309–4318, 2009.
- [9] Mordechai Ben-Ari and Francesco Mondada. *Elements of Robotics (Robots and Their Applications)*. 2017.
- [10] H. C. Bennet Clark. The energetics of the jump of the locust *Schistocerca gregaria*. *Journal of Experimental Biology*, 63(1):53–83, 1975.
- [11] H. C. Bennet-Clark and E. C. Lucey. The jump of the flea: a study of the energetics and a model of the mechanism. *Journal of Experimental Biology*, 47(1):59–67, 1967.
- [12] H.C. BENNETCLARK. *Energy Storage in Jumping Animals*, volume 1. Pergamon Press, 1976.
- [13] Sara Bernardini, Ferdinand Jovan, Zhengyi Jiang, Simon Watson, Peiman Moradi, Tom Richardson, Rasoul Sadeghian, and Sina Sareh. A Multi-Robot Platform for the Autonomous Operation and Maintenance of Offshore Wind Farms. *Aamas*, pages 1696–1700, 2020.
- [14] A. A. Biewener. Allometry of quadrupedal locomotion: the scaling of duty factor, bone curvature and limb orientation to body size. *Journal of Experimental Biology*, 105:147–171, 1983.
- [15] Robert Bogue. Robots poised to revolutionise agriculture. *Industrial Robot*, 43(5):450–456, 2016.

- [16] Anna L Brill, Avik De, Aaron M Johnson, and Daniel E Koditschek. Tail-assisted rigid and compliant legged leaping. In *Intelligent Robots and Systems (IROS), 2015 IEEE/RSJ International Conference on*, pages 6304–6311. IEEE, 2015.
- [17] Paul Brochu and Qibing Pei. Advances in dielectric elastomers for actuators and artificial muscles. *Macromolecular Rapid Communications*, 31(1):10–36, 2010.
- [18] Steven L. Brunton and Bernd R. Noack. Closed-loop turbulence control: Progress and challenges. *Applied Mechanics Reviews*, 67(5), 2015.
- [19] Jiawei Cao, Wenyu Liang, Jian Zhu, and Qinyuan Ren. Control of a muscle-like soft actuator via a bioinspired approach. 2018.
- [20] Keene Chin, Tess Hellebrekers, and Carmel Majidi. Machine Learning for Soft Robotic Sensing and Control. *Advanced Intelligent Systems*, 2(6):1900171, 2020.
- [21] E. Coevoet, T. Morales-Bieze, F. Largilliere, Z. Zhang, M. Thieffry, M. Sanz-Lopez, B. Carrez, D. Marchal, O. Goury, J. Dequidt, and C. Duriez. Software toolkit for modeling, simulation, and control of soft robots. *Advanced Robotics*, 31(22):1208–1224, 2017.
- [22] Nikolaus Correll, Nikos Arechiga, Adrienne Bolger, Mario Bollini, Ben Charrow, Adam Clayton, Felipe Dominguez, Kenneth Donahue, Samuel Dyar, Luke Johnson, Huan Liu, Alexander Patrikalakis, Timothy Robertson, Jeremy Smith, Daniel Soltero, Melissa Tanner, Lauren White, and Daniela Rus. Indoor robot gardening: Design and implementation. *Intelligent Service Robotics*, 3(4):219–232, 2010.
- [23] J. M. Duperret, G. D. Kenneally, J. L. Pusey, and D. E. Koditschek. Towards a comparative measure of legged agility. *Springer Tracts in Advanced Robotics*, 109(June):3–16, 2016.
- [24] Nazek El-Atab, Rishabh B Mishra, Fhad Al-Modaf, Lana Joharji, Aljohara A Alsharif, Haneen Alamoudi, Marlon Diaz, Nadeem Qaiser, and Muhammad Mustafa Hussain. Soft Actuators for Soft Robotic Applications: A Review. *Advanced Intelligent Systems*, 2000128:2000128, 2020.
- [25] M. E.G. Evans. The jump of the click beetle (Coleoptera, Elateridae)—a preliminary study. *Journal of Zoology*, 167(3):319–336, 1972.
- [26] M. E.G. Evans. The jump of the click beetle (Coleoptera: Elateridae)—energetics and mechanics. *Journal of Zoology*, 169(2):181–194, 1973.
- [27] Julie M Gabriel. The development of the locust jumping mechanism. *Journal of Experimental Biology*, 118:327–340, 1985.
- [28] Todd A. Gisby, Benjamin M. Obrien, and Iain A. Anderson. Self sensing feedback for dielectric elastomer actuators. *Applied Physics Letters*, 102(19), 2013.
- [29] Todd A. Gisby, Benjamin M. O'Brien, Sheng Q. Xie, Emilio P. Calius, and Iain A. Anderson. Closed loop control of dielectric elastomer actuators. *Electroactive Polymer Actuators and Devices (EAPAD) 2011*, 7976(March 2011):797620, 2011.
- [30] Stephan-Daniel Gravert, Mike Y Michelis, Simon Rogler, Dario Tscholl, Thomas Buchner, and Robert K Katzschmann. Planar modeling and sim-to-real of a tethered multimaterial soft swimmer driven by peano-hasels. *arXiv preprint arXiv:2208.00731*, 2022.
- [31] R. I. Griffiths. Shortening of muscle fibres during stretch of the active cat medial gas-

- trocnemius muscle: the role of tendon compliance. *The Journal of Physiology*, 436(1):219–236, 1991.
- [32] Keir Groves, Andrew West, Konrad Gornicki, Simon Watson, Joaquin Carrasco, and Barry Lennox. MallARD: An autonomous aquatic surface vehicle for inspection and monitoring of wet nuclear storage facilities. *Robotics*, 8(2), 2019.
- [33] Duncan W. Haldane, M. M. Plecnik, J. K. Yim, and R. S. Fearing. Robotic vertical jumping agility via Series-Elastic power modulation. *Science Robotics*, 1(1), 2016.
- [34] W. J. Heitler. The locust jump. *Journal of Comparative Physiology*, 89(1):93–104, 1974.
- [35] Havalee T. Henry, David J. Ellerby, and Richard L. Marsh. Performance of guinea fowl Numida meleagris during jumping requires storage and release of elastic energy. *Journal of Experimental Biology*, 208(17):3293–3302, 2005.
- [36] Chong Hong, Dewei Tang, Qiquan Quan, Zhuoqun Cao, and Zongquan Deng. A combined series-elastic actuator parallel-elastic leg no-latch bio-inspired jumping robot. *Mechanism and Machine Theory*, 149:103814, 2020.
- [37] Stacy Hunt, Thomas G. McKay, and Iain A. Anderson. A self-healing dielectric elastomer actuator. *Applied Physics Letters*, 104(11):2012–2015, 2014.
- [38] Paul G. Huray. *Maxwell's Equations*. Number 915. John Wiley & Sons, Inc, 2015.
- [39] Filip Ilievski, Aaron D. Mazzeo, Robert F. Shepherd, Xin Chen, and George M. Whitesides. Soft robotics for chemists. *Angewandte Chemie International Edition*, 50(8):1890–1895, 2011.
- [40] IFR International Federation of Robotics. Executive Summary World Robotics 2020 Industrial Robots. *World Robotic Report*, pages 15–24, 2020.
- [41] Rob S. James, Carlos A. Navas, and Anthony Herrel. How important are skeletal muscle mechanics in setting limits on jumping performance? *Journal of Experimental Biology*, 210(6):923–933, 2007.
- [42] Maxwell James Clerk. A treatise on electricity and magnetism. *A Treatise on Electricity and Magnetism*, 9781108014038:1–442, 1873.
- [43] Tyler Jenkins and Matthew Bryant. Variable stiffness soft robotics using pennate muscle architecture. In *Bioinspiration, Biomimetics, and Bioreplication IX*, volume 10965, pages 18–27. SPIE, 2019.
- [44] Xiaobin Ji, Xinchang Liu, Vito Cacucciolo, Matthias Imboden, Yoan Civet, Alae El Haitami, Sophie Cantin, Yves Perriard, and Herbert Shea. An autonomous untethered fast soft robotic insect driven by low-voltage dielectric elastomer actuators. *Science Robotics*, 4(37), 2019.
- [45] Gwang Pil Jung, Carlos S. Casarez, Sun Pill Jung, Ronald S. Fearing, and Kyu Jin Cho. An integrated jumping-crawling robot using height-adjustable jumping module. *Proceedings - IEEE International Conference on Robotics and Automation*, 2016-June:4680–4685, 2016.
- [46] Kwangmok Jung, Kwang J. Kim, and Hyouk Ryeol Choi. A self-sensing dielectric elastomer actuator. *Sensors and Actuators, A: Physical*, 143(2):343–351, 2008.
- [47] Navvab Kashiri, Andy Abate, Sabrina J Abram, Alin Albu-Schaffer, Patrick J Clary, Monica Daley, Salman Faraji, Raphael Furnemont, Manolo Garabini, Hartmut Geyer,

- et al. An overview on principles for energy efficient robot locomotion. *Frontiers in Robotics and AI*, 5:129, 2018.
- [48] Nicholas Kellaris, Philipp Rothemund, Yi Zeng, Shane K. Mitchell, Garrett M. Smith, Kaushik Jayaram, and Christoph Keplinger. Spider-Inspired Electrohydraulic Actuators for Fast, Soft-Actuated Joints. *Advanced Science*, 2100916:1–16, 2021.
- [49] Nicholas Kellaris, Vidyacharan Gopaluni Venkata, Philipp Rothemund, and Christoph Keplinger. An analytical model for the design of Peano-HASEL actuators with drastically improved performance. *Extreme Mechanics Letters*, 29:100449, 2019.
- [50] Nicholas Kellaris, Vidyacharan Gopaluni Venkata, Garrett M. Smith, Shane K. Mitchell, and Christoph Keplinger. Peano-HASEL actuators: Muscle-mimetic, electrohydraulic transducers that linearly contract on activation. *Science Robotics*, 3(14):1–11, 2018.
- [51] John Thomas Kendrick. Design of High-Performance, Dual-Motor Liquid-Cooled, Linear Series Elastic Actuators for a Self-Balancing Exoskeleton. (February), 2018.
- [52] Daekyun Kim, Sang-hun Kim Id, Taekyoungh Kim Id, Brian Byunghyun Kang, Minhyuk Lee, Wookeun Park Id, Subyeong Ku, Dongwook Kim Id, Junghan Kwon, Hochang Lee, Joonbum Bae, Yong-lae Park, and Kyujin Cho. Review of machine learning methods in soft robotics. pages 1–24, 2021.
- [53] Coleman Knabe, Bryce Lee, Viktor Orehov, and Dennis Hong. Design of a compact, lightweight, electromechanical linear series elastic actuator. *Proceedings of the ASME Design Engineering Technical Conference*, 5B:1–8, 2014.
- [54] Kyoungchul Kong, Joonbum Bae, and Masayoshi Tomizuka. A compact rotary series elastic actuator for human assistive systems. *IEEE/ASME Transactions on Mechatronics*, 17(2):288–297, 2012.
- [55] Mirko Kovač, Manuel Schlegel, Jean Christophe Zufferey, and Dario Floreano. Steerable miniature jumping robot. *Autonomous Robots*, 28(3):295–306, 2010.
- [56] G. Kovacs, L. Düring, S. Michel, and G. Terrasi. Stacked dielectric elastomer actuator for tensile force transmission. *Sensors and Actuators, A: Physical*, 155(2):299–307, 2009.
- [57] Anand Kumar, Nirma Yadav, Shipra Singh, and Neha Chauhan. Minimally invasive (endoscopic-computer assisted) surgery: Technique and review. *Annals of Maxillofacial Surgery*, 6(2):159, 2016.
- [58] Cecilia Laschi, Barbara Mazzolai, and Matteo Cianchetti. Soft robotics: Technologies and systems pushing the boundaries of robot abilities. *Science Robotics*, 1(1):eaah3690, 2016.
- [59] Chan Lee, Suhui Kwak, Jihoo Kwak, and Sehoon Oh. Generalization of series elastic actuator configurations and dynamic behavior comparison. *Actuators*, 6(3), 2017.
- [60] Thomas Lens and Oskar von Stryk. Design and dynamics model of a lightweight series elastic tendon-driven robot arm. In *2013 IEEE International Conference on Robotics and Automation*, pages 4512–4518. IEEE, 2013.
- [61] R. L. Lieber, M. E. Leonard, C. G. Brown, and C. L. Trestik. Frog semitendinosus tendon load-strain and stress-strain properties during passive loading. *American Journal of Physiology - Cell Physiology*, 261(1 30-1), 1991.
- [62] Richard L. Lieber, Margot E. Leonard, and Cynthia G. Brown-Maupin. Effects of muscle

- contraction on the load-strain properties of frog aponeurosis and tendon. *Cells Tissues Organs*, 166(1):48–54, 2000.
- [63] Gordon J Lutz and Lawrence C Rome. Built for Jumping : The Design of the Frog Muscular System. *Science*, 263(5145):370–372, 1994.
- [64] Khoi Ly, Nicholas Kellaris, Dade McMorris, Brian K. Johnson, Eric Acome, Vani Sundaram, Mantas Naris, J. Sean Humbert, Mark E. Rentschler, Christoph Keplinger, and Nikolaus Correll. Miniaturized Circuitry for Capacitive Self-Sensing and Closed-Loop Control of Soft Electrostatic Transducers. *Soft Robotics*, 00(00):1–14, 2020.
- [65] RL MARSH. Jumping ability of anuran amphibians. *Advances in veterinary science and comparative medicine*, 38:51–111, 1994.
- [66] Craig P. McGowan and Clint E. Collins. Why do mammals hop? Understanding the ecology, biomechanics and evolution of bipedal hopping. *Journal of Experimental Biology*, 221(12), 2018.
- [67] Davis J. McGregor, Sameh Tawfick, and William P. King. Mechanical properties of hexagonal lattice structures fabricated using continuous liquid interface production additive manufacturing. *Additive Manufacturing*, 25:10–18, 2019.
- [68] Thomas A. McHanion. Effects of Scale. In *Muscles, Reflexes, and Locomotion*, chapter Chapter 9., pages 234–296. Princeton University Press., 1984.
- [69] MiMRee. Multi-Platform Inspection, Maintenance and Repair in Extreme Environments (MiMRee) — Project — ORE Catapult, 2019.
- [70] Shane K. Mitchell, Xingrui Wang, Eric Acome, Trent Martin, Khoi Ly, Nicholas Kellaris, Vidyacharan Gopaluni Venkata, and Christoph Keplinger. An Easy-to-Implement Toolkit to Create Versatile and High-Performance HASEL Actuators for Untethered Soft Robots. *Advanced Science*, 6(14), 2019.
- [71] Pauli Mustalahti and Jouni Mattila. Position-based impedance control design for a hydraulically actuated series elastic actuator. *Energies*, 15(7), 2022.
- [72] Keiji Nagatani, Seiga Kiribayashi, Yoshito Okada, Kazuki Otake, Kazuya Yoshida, Satoshi Tadokoro, Takeshi Nishimura, Tomoaki Yoshida, Eiji Koyanagi, Mineo Fukushima, and Shinji Kawatsuma. Emergency response to the nuclear accident at the Fukushima Daiichi Nuclear Power Plants using mobile rescue robots. *Journal of Field Robotics*, 30(1):44–63, 2013.
- [73] M. Nancekievill, A. R. Jones, M. J. Joyce, B. Lennox, S. Watson, J. Katakura, K. Okumura, S. Kamada, M. Katoh, and K. Nishimura. Development of a Radiological Characterization Submersible ROV for Use at Fukushima Daiichi. *IEEE Transactions on Nuclear Science*, 65(9):2565–2572, 2018.
- [74] Matthew Nancekievill, Jose Espinosa, Simon Watson, Barry Lennox, Ashley Jones, Malcolm J. Joyce, Jun Ichi Katakura, Keisuke Okumura, So Kamada, Michio Katoh, and Kazuya Nishimura. Detection of simulated fukushima daichii fuel debris using a remotely operated vehicle at the naraha test facility. *Sensors (Switzerland)*, 19(20), 2019.
- [75] Eduardo Navas, Roemi Fernández, Delia Sepúlveda, Manuel Armada, and Pablo Gonzalez-de santos. Soft Grippers for Automatic Crop Harvesting : A Review. 2021.
- [76] Ryuma Niiyama, Daniela Rus, and Sangbae Kim. Pouch Motors: Printable/inflatable soft

- actuators for robotics. *Proceedings - IEEE International Conference on Robotics and Automation*, pages 6332–6337, 2014.
- [77] Siti Noor Azizzati Mohd Noor and Jamaluddin Mahmud. Modelling and computation of silicone rubber deformation adapting neo-hookean constitutive equation. In *2015 Fifth International Conference on Communication Systems and Network Technologies*, pages 1323–1326. IEEE, 2015.
- [78] Luiz F.P. Oliveira, António P. Moreira, and Manuel F. Silva. Advances in agriculture robotics: A state-of-the-art review and challenges ahead. *Robotics*, 10(2):1–31, 2021.
- [79] Daniel Joseph Paluska, Gill A Pratt, and Daniel Joseph Paluska. Design of a Humanoid Biped for Walking Research by Master of Science at the Signature of Author Design of a Humanoid Biped for Walking Research by. 2003.
- [80] Brian S. Peters, Priscila R. Armijo, Crystal Krause, Songita A. Choudhury, and Dmitry Oleynikov. Review of emerging surgical robotic technology. *Surgical Endoscopy*, 32(4):1636–1655, 2018.
- [81] Panagiotis Polygerinos, Nikolaus Correll, Stephen A. Morin, Bobak Mosadegh, Cagdas D. Onal, Kirstin Petersen, Matteo Cianchetti, Michael T. Tolley, and Robert F. Shepherd. Soft Robotics: Review of Fluid-Driven Intrinsically Soft Devices; Manufacturing, Sensing, Control, and Applications in Human-Robot Interaction. *Advanced Engineering Materials*, 19(12), 2017.
- [82] Gill A. Pratt and Matthew M. Williamson. Series elastic actuators. *IEEE International Conference on Intelligent Robots and Systems*, 1:399–406, 1995.
- [83] Jerry Pratt and Gill Pratt. Intuitive control of a planar bipedal walking robot. *Proceedings - IEEE International Conference on Robotics and Automation*, 3(May 1998):2014–2021, 1998.
- [84] Uwe Prosko. Energy conservation by elastic storage in kangaroos. *Endeavour*, 4(4):148–153, 1980.
- [85] S. M.Mizanoor Rahman. A novel variable impedance compact compliant series elastic actuator for human-friendly soft robotics applications. *Proceedings - IEEE International Workshop on Robot and Human Interactive Communication*, pages 19–24, 2012.
- [86] Neil D. Reeves and Glen Cooper. Is human Achilles tendon deformation greater in regions where cross-sectional area is smaller? *Journal of Experimental Biology*, 220(9):1634–1642, 2017.
- [87] Michele Righi, Marco Fontana, Rocco Vertechy, Mattia Duranti, and Giacomo Moretti. Analysis of dielectric fluid transducers. (March):29, 2018.
- [88] Thomas J. Roberts. The integrated function of muscles and tendons during locomotion. *Comparative Biochemistry and Physiology - A Molecular and Integrative Physiology*, 133(4):1087–1099, 2002.
- [89] Thomas J. Roberts and Emanuel Azizi. Flexible mechanisms: The diverse roles of biological springs in vertebrate movement. *Journal of Experimental Biology*, 214(3):353–361, 2011.
- [90] Thomas J. Roberts and Richard L. Marsh. Probing the limits to muscle-powered accelerations: Lessons from jumping bullfrogs. *Journal of Experimental Biology*, 206(15):2567–2580, 2003.

- [91] David W. Robinson, Jerry E. Pratt, Daniel J. Paluska, and Gill A. Pratt. Series elastic actuator development for a biomimetic walking robot. *IEEE/ASME International Conference on Advanced Intelligent Mechatronics, AIM*, pages 561–568, 1999.
- [92] Dylan Ross, Markus P. Nemitz, and Adam A. Stokes. Controlling and Simulating Soft Robotic Systems: Insights from a Thermodynamic Perspective. *Soft Robotics*, 3(4):170–176, 2016.
- [93] Samuel Rosset and Herbert R. Shea. Small, fast, and tough: Shrinking down integrated elastomer transducers. *Applied Physics Reviews*, 3(3), 2016.
- [94] Philipp Rothemund, Nicholas Kellaris, and Christoph Keplinger. How inhomogeneous zipping increases the force output of Peano-HASEL actuators. *Extreme Mechanics Letters*, 31:100542, 2019.
- [95] Philipp Rothemund, Nicholas Kellaris, Shane K Mitchell, Eric Acome, and Christoph Keplinger. HASEL Artificial Muscles for a New Generation of Lifelike Robots — Recent Progress and Future Opportunities. 2003375:1–28, 2020.
- [96] Philipp Rothemund, Sophie Kirkman, and Christoph Keplinger. Dynamics of electrohydraulic soft actuators. *Proceedings of the National Academy of Sciences of the United States of America*, 117(28):16207–16213, 2020.
- [97] Philipp Rothemund, Sophie Kirkman, and Christoph Keplinger. Dynamics of electrohydraulic soft actuators. *Proceedings of the National Academy of Sciences of the United States of America*, 117(28):16207–16213, 2020.
- [98] Ellen Rumley, Philipp Rothemund, Steven Zhang, Nicholas Kellaris, and Christoph Keplinger. Characterization of charge retention effects in HASEL actuators. In Iain A. Anderson, John D. W. Madden, and Herbert R. Shea, editors, *Electroactive Polymer Actuators and Devices (EAPAD) XXIV*, volume PC12042, page PC120420B. International Society for Optics and Photonics, SPIE, 2022.
- [99] Umberto Scarfogliero, Cesare Stefanini, and Paolo Dario. Design and development of the long-jumping "grillo" mini robot. *Proceedings - IEEE International Conference on Robotics and Automation*, (April):467–472, 2007.
- [100] Cosima Schunk, Levi Pearson, Eric Acome, Timothy G. Morrissey, Nikolaus Correll, Christoph Keplinger, Mark E. Rentschler, and J. Sean Humbert. System Identification and Closed-Loop Control of a Hydraulically Amplified Self-Healing Electrostatic (HASEL) Actuator. *IEEE International Conference on Intelligent Robots and Systems*, pages 6417–6423, 2018.
- [101] Jonathon W Sensinger and Richard F Ff Weir. Improvements to series elastic actuators. In *2006 2nd IEEE/ASME International Conference on Mechatronics and Embedded Systems and Applications*, pages 1–7. IEEE, 2006.
- [102] Fabrizio Sergi, Dino Accoto, Giorgio Carpino, Nevio Luigi Tagliamonte, and Eugenio Guglielmelli. Design and characterization of a compact rotary Series Elastic Actuator for knee assistance during overground walking. *Proceedings of the IEEE RAS and EMBS International Conference on Biomedical Robotics and Biomechatronics*, pages 1931–1936, 2012.
- [103] Azad Shademan, Ryan S Decker, Justin D Opfermann, Simon Leonard, Axel Krieger, and Peter C W Kim. Supervised autonomous robotic soft tissue surgery. Technical report.

- [104] Hamed Toubar, Mohammad I Awad, Mohamed N Boushaki, Zhenwei Niu, Kinda Khalaf, and Irfan Hussain. Design, modeling, and control of a series elastic actuator with discretely adjustable stiffness (seadas). *Mechatronics*, 86:102863, 2022.
- [105] Hanh Tran. Robotic Single-Port Hernia Surgery. 2011.
- [106] C. L. Trestik and R. L. Lieber. Relationship between achilles tendon mechanical properties and gastrocnemius muscle function. *Journal of Biomechanical Engineering*, 115(3):225–230, 1993.
- [107] B. Vanderborght, A. Albu-Schaeffer, A. Bicchi, E. Burdet, D. G. Caldwell, R. Carloni, M. Catalano, O. Eiberger, W. Friedl, G. Ganesh, M. Garabini, M. Grebenstein, G. Grioli, S. Haddadin, H. Hoppner, A. Jafari, M. Laffranchi, D. Lefeber, F. Petit, S. Stramigioli, N. Tsagarakis, M. Van Damme, R. Van Ham, L. C. Visser, and S. Wolf. Variable impedance actuators: A review. *Robotics and Autonomous Systems*, 61(12):1601–1614, 2013.
- [108] Chao Wan, Zhixiu Hao, and Xiqiao Feng. Structures, properties, and energy-storage mechanisms of the semi-lunar process cuticles in locusts. *Scientific Reports*, 6(June):1–13, 2016.
- [109] Xingrui Wang, Shane K. Mitchell, Ellen H. Rumley, Philipp Rothmund, and Christoph Keplinger. High-Strain Peano-HASEL Actuators. *Advanced Functional Materials*, 30(7):1–9, 2020.
- [110] Patrick M. Wensing, Albert Wang, Sangok Seok, David Otten, Jeffrey Lang, and Sangbae Kim. Proprioceptive actuator design in the MIT cheetah: Impact mitigation and high-bandwidth physical interaction for dynamic legged robots. *IEEE Transactions on Robotics*, 33(3):509–522, 2017.
- [111] George M Whitesides. Soft robotics. *Angewandte Chemie International Edition*, 57(16):4258–4273, 2018.
- [112] James P Wissman, Alec K Ikeno, and Charles A Rohde. Hydraulically Amplified Self-Healing Electrostatic ( HASEL ) Inspired Actuators. 2020.
- [113] Sebastian Wolf, Giorgio Grioli, Oliver Eiberger, Werner Friedl, Markus Grebenstein, Hannes Hoppner, Etienne Burdet, Darwin G. Caldwell, Raffaella Carloni, Manuel G. Catalano, Dirk Lefeber, Stefano Stramigioli, Nikos Tsagarakis, Michael Van Damme, Ronald Van Ham, Bram Vanderborght, Ludo C. Visser, Antonio Bicchi, and Alin Albu-Schaffer. Variable Stiffness Actuators: Review on Design and Components. *IEEE/ASME Transactions on Mechatronics*, 21(5):2418–2430, 2016.
- [114] Matthew A. Woodward and Metin Sitti. MultiMo-Bat: A biologically inspired integrated jumping-gliding robot. *International Journal of Robotics Research*, 33(12):1511–1529, 2014.
- [115] Ernest Y. Wu, J. Suñé, and W. Lai. On the weibull shape factor of intrinsic breakdown of dielectric films and its accurate experimental determination-Part II: Experimental results and the effects of stress conditions. *IEEE Transactions on Electron Devices*, 49(12):2141–2150, 2002.
- [116] Chi Zhang, Wei Zou, Liping Ma, and Zhiqing Wang. Biologically inspired jumping robots: A comprehensive review. *Robotics and Mechatronics*, C., Zou, W., Ma, L., and Wang, Z. (2020). *Biologically inspired jumping robots: A comprehensive review*. *Robotics and Mechatronics*, 2020:1–20, 2020.

- and Autonomous Systems, 124, 103362. ELASTOMERS Zhigang Suo \* School of Engineering and Applied Sciences, Kavli Institute for Nanobio Science and Technology, Harvard University, Cambridge, MA 02138. October, 2019. <https://doi.org/10.1101/103362>Autonomougineering and Applied Sciences, Kavli Institute for Nanobio Science and Technology, Harvard University, Cambridge, MA 02138. October, 2019. <https://doi.org/10.1101/103362>
- [117] Zhigang Suo. THEORY OF DIELECTRIC